ANALYSIS OF NEARSHORE CURRENT PATTERNS USING AERIAL DRONE MEASUREMENTS AT MONWABISI

by

Ryan Phillip Shaw Abrey

Thesis presented in fulfilment of the requirements for the degree of Master of Engineering in Civil Engineering in the Faculty of Engineering at Stellenbosch University

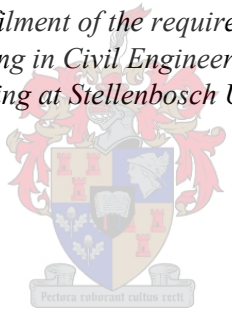

Supervisor: Prof K Schoonees

Co-supervisor: Mr L Croukamp

December 2019

PLAGIAATVERKLARING / PLAGIARISM DECLARATION

1. Plagiaat is die oorneem en gebruik van die idees, materiaal en ander intellektuele eiendom van ander persone asof dit jou eie werk is.

   Plagiarism is the use of ideas, material and other intellectual property of another's work and to present is as my own.

2. Ek erken dat die pleeg van plagiaat 'n strafbare oortreding is aangesien dit 'n vorm van diefstal is.

   I agree that plagiarism is a punishable offence because it constitutes theft.

3. Ek verstaan ook dat direkte vertalings plagiaat is.

   I also understand that direct translations are plagiarism.

4. Dienooreenkomstig is alle aanhalings en bydraes vanuit enige bron (ingesluit die internet) volledig verwys (erken). Ek erken dat die woordelikse aanhaal van teks sonder aanhalingstekens (selfs al word die bron volledig erken) plagiaat is.

   Accordingly, all quotations and contributions from any source whatsoever (including the internet) have been cited fully. I understand that the reproduction of text without quotation marks (even when the source is cited) is plagiarism.

5. Ek verklaar dat die werk in hierdie skryfstuk vervat, behalwe waar anders aangedui, my eie oorspronklike werk is en dat ek dit nie vantevore in die geheel of gedeeltelik ingehandig het vir bepunting in hierdie module/werkstuk of 'n ander module/werkstuk nie.

   I declare that the work contained in this assignment, except where otherwise stated, is my original work and that I have not previously (in its entirety or in part) submitted it for grading in this module/assignment or another module/assignment.

_____
Ryan Phillip Shaw Abrey

_____
Student number

_____
Date

Abstract

This thesis explores the development of a methodology for using quadcopter aerial drones to measure currents in the nearshore zone, along with assessing other possible applications within the marine environment.

Current velocities were measured at Monwabisi beach in False Bay, Cape Town to enable the results to be compared with similar studies already conducted in the area. This provided a means of result validation, as the scope of the study did not include budget for measurement of sea currents with electronic instruments during the testing for comparison. The primary drone used during testing was a DJI Mavic Air due to its affordable price and ease of use, making it more accessible to most users.

Calibration tests were conducted on land to measure a fixed known length in order to adequately scale the photos taken by the drone to the altitude recorded by the on-board altimeter. During calibration the drone was flown at different heights with the camera facing directly down and a set of photos were taken of a tape measure which could then be scaled in AutoCAD. This was crucial as the typical land-based method of photogrammetry, to determine height and distance from the drone, would not be reliable over water as its surface is constantly shifting.

A set of coordinates of a static point was also measured in order to determine the horizontal accuracy of the reported coordinates which rely on the on-board GPS measurements. It was found that the measured coordinates required smoothing to compensate for GPS errors encountered by the drone. The drone used has a reported horizontal hovering accuracy of ±1.5 m but was found to produce a measured mean current precision below 2 $cm.s^{-1}$ once averaged over 10 seconds. This information filtered into a method for tracking drifters as they floated on the sea surface behind the surf zone. This is similar to the existing method of GPS current drifters; however, biodegradable oranges could now be used in their place with the drone above measuring their coordinates as they drifted on the currents.

Several tests were then carried out during different environmental conditions at Monwabisi and a range of currents were measured for comparison with the previous studies. Measurements taken by the drone resulted in similar current patterns to those seen in the previous studies model results. Furthermore, the current velocities were of the same order of magnitude.

It was also found that the drone could observe other aspects from above such as: effluent plumes at diffusers, marine life and even sediment movements. Each of these aspects could prove valuable for coastal studies in providing data at a reasonable cost. Overall, the findings proved that a quadcopter aerial drone is a versatile engineering tool which was able to measure currents in the nearshore zone while finding similar flow patterns to previous model results.

Opsomming

Hierdie tesis ondersoek die ontwikkeling van 'n metodologie vir die gebruik van hommeltuie om strome in die nabystrandse sone te meet, asook die evaluering van ander moontlike toepassings in die mariene omgewing.

Stroomsnelhede is by die Monwabisi-strand in Valsbaai, Kaapstad gemeet sodat die resultate vergelyk kon word met dié van soortgelyke toetse wat reeds in die gebied uitgevoer is. Hierdie toetse het 'n geleentheid geskep vir die bevestiging van resultate aangesien die meting en vergelyking van seestrome met elektroniese instrumente nie deel van die projekbegroting was nie. Die primêre hommeltuig wat tydens die toetse gebruik is, was 'n DJI Mavic Air as gevolg van die bekostigbare prys en gemak van gebruik wat dit toeganklik vir die meeste gebruikers maak.

Ykingstoetse is op land uitgevoer om 'n vasgestelde voorafbepaalde lengte te meet sodat die foto's wat deur die hommeltuig geneem word, se skaal bepaal kon word met betrekking tot die hoogte wat deur die aanboordse hoogtemeter aangeteken word. Tydens yking is die hommeltuig teen verskillende hoogtes gevlieg met die kamera direk na onder gemik om 'n stel foto's te neem wat dan in Autocad geskaal kon word. Die metode is noodsaaklik aangesien die tipiese landgebaseerde metode van fotogrammetrie om die hoogte en afstand van die hommeltuie te bepaal, nie betroubaar oor water is nie aangesien daar konstante beweging is.

'n Stel koördinate van 'n statiese punt is ook gemeet om die horisontale akkuraatheid van die aangemelde koördinate wat van die aanboordse GPS-metings afhang, te bepaal. Dit is gevind dat die gemete koördinate gladstryking nodig het om vir foute wat deur die hommeltuig gemaak word, te kompenseer. Die hommeltuig het 'n gerapporteerde stilsweef-akkuraatheid van ±1.5 m, maar daar is gevind dat die gemete gemiddelde akkuraatheid onder 2 $cm.s^{-1}$ was nadat 'n gemiddelde oor 'n 10-sekonde-interval bepaal is. Hierdie inligting is gefilter deur 'n metode om boeie te volg terwyl hulle op die see- oppervlakte agter die nabystrandse sone dryf. Hierdie metode is soortgelyk aan die metode wat deur huidige GPS-stroomboeie gebruik word. Bioafbreekbare lemoene kan nou in hulle plek gebruik word met die hommeltuig wat van bo hulle koördinate meet terwyl hulle in seestrome dryf.

Verskeie toetse is daarna uitgevoer tydens verskillende omgewingstoestande by Monwabisi en 'n verskeidenheid strome is gemeet vir vergelyking met vorige studies. Metings deur die hommeltuig het soortgelyke stroompatrone as vorige studiemodelle getoon. Verder, was die stroomsnelhede van dieselfde grootte-orde.

Daar is ook gevind dat die hommeltuig ander aspekte van bo kon meet, soos uitvloeiselwolke by verspreiders, mariene lewe en sedimentbewegings. Elkeen van hierdie aspekte kan waardevol in kusstudies wees om data teen redelike koste te verkry. In die algemeen is daar gevind dat hommeltuie veelsydige ingenieursinstrumente is wat strome in die nabystrandse sone kan meet, terwyl die resultate soortgelyk aan vorige modelresultate is.

Acknowledgements

I would first like to thank my thesis advisor Prof Koos Schoonees and co-supervisor Mr Leon Croukamp of the Department of Civil Engineering at University of Stellenbosch for their guidance in developing this thesis.

I would also like to thank S. Kistner from PRDW for providing me with insight into his previous work as well as wave data for Monwabisi. I appreciate the efforts by Yaseen Gamiet from NSRI in compiling any information available to be used in this thesis. I cannot forget Christo Rautenbach who was always available to give advice and help where needed.

To my brother Mark, your expertise in academia has shone through and I really appreciate all of your comments polishing up this thesis. To my parents Donna-Jean and Russell, your continued support is always treasured.

I must express my very profound gratitude to my wife Genevieve for her boundless support and patience throughout my years of study and through this thesis process. This accomplishment would not have been possible without her. I thank her sincerely.

Lastly, I must thank God, the source of it all.

Contents

List of Figures

List of Tables

Nomenclature

LIST OF ABBREVIATIONS

Symbol	Term
α_b	Angle between the incoming wave crests and the shoreline
f	Focal Length
h	Altitude/Distance to subject
S_w	Sensor Width
U	Current Velocity
u_w	Steady current driven by breaking waves
u_t	Tidal current
u_a	Wind-driven current
u_o	Oscillatory flows due to wind waves
u_I	Oscillatory flows due to infragravity waves
U_{PA30}	30 m peak average current velocity
U	Cross shore currents
V	Longshore currents

Acronym	Term
ADV	Acoustic Doppler Velocimeter
ADCP	Acoustic Doppler Current Profiler
AWAC	Acoustic Wave Current Profiler
AOV	Angle of View
CAA	Civil Aviation Authority
CoastalCOMS	Coastal Conditions Monitoring System
EXIF	Exchange image file format
FOV	Field of view
GCP	Ground Control Point
GNSS	Global Navigation Satellite System
GPS	Global Positioning System
GSD	Ground Sample Distance
RPA	Remotely Piloted Aircraft
SAWS	South African Weather Service
UTM	Universal Transverse Mercator
VBA	Visual Basic for Applications
WGS	World Geodetic System

Chapter 1: Introduction

Scientists and engineers are constantly searching for new and innovative ways to collect information about their surroundings in a simpler manner, while maintaining the accuracy of existing methods. Advances in other fields may often lead to a novel methodology that has been done a certain way in another field up until that point. This thesis aims to explore the use of the newly accessible technology of aerial quadcopter drones to measure currents in the nearshore zone which would typically have been carried out with expensive helicopters or submerged instruments. Using drones would allow for site data to be collected quickly and easily, early on in the project life reducing the number of assumptions made. Most notably when sea current modelling is required, using drones to provide onsite current measurements could provide calibration data, especially when little to no data would be available as budgets do not allow for expensive current measurements during project initiation, or during tender designs.

1.1 Background

This study was based on Monwabisi Beach off False Bay, on the South African Cape Peninsula. Two previous studies have already investigated the currents at Monwabisi to assess its safety for swimming, first by the CSIR in 1997 and then by Kistner in 2016 to fulfil his master's degree requirements at the University of Stellenbosch. Neither of these studies were able to source adequate site measurements for calibration of the physical/numerical models. This was due to the high costs associated with traditional techniques for environmental measurement in the coastal zone. This study proposes a simpler and cheaper method for measuring currents, using widely accessible drones, to provide a solution to data collection in cases such as these two previous studies.

1.2 Limitations of This Study

This study included no scope for calibrating the results of the drone collection method using other more traditional measurement techniques, due to limited funding. The current magnitudes were compared to those modelled by Kistner.

The environmental conditions tested were subject to the day on which the data was collected and hence the exact conditions tested in the previous studies were not sampled. The on-site environmental conditions were not measured and hence wind and wave data has been sourced from nearby weather stations or through numerical models for False Bay.

1.3 Chapter Layout

This study is arranged such that after this introduction, Chapter 2 commences with a review of literature currently available. Chapter 3 then provides the methodology proposed followed by Chapter 4 with results. Chapters 5 and 6 contain conclusions and recommendations respectively.

1.4 Objectives

The main objectives of this study were as follows:

1.4.1 Develop a method for utilising Drones for Current Data Collection

The main objective of this study was to develop a methodology for the use of drones in the measurement of current velocity in the nearshore zone by tracking drifters through sequential aerial photographs. The developed method needed to orientate the acquired images geographically and then assign coordinates to the drifters such that the velocities could be calculated for each time-step. This then allowed for a set of velocities to be statistically processed to provide a characteristic flow pattern. The intention was to provide a simple and cost-effective method for quick nearshore current results without the need for existing expensive and difficult to implement current measurement methods.

1.4.2 Compare Results with Previous Studies

Two previous studies have been carried out on the currents within Monwabisi Bay and this study aimed to compare the results acquired using the drone method with the results from these studies as neither study was able to calibrate their models with actual measurements on site.

1.4.3 Evaluate the use of Drones for Marine Data Collection

During the collection of current data at Monwabisi Bay, any additional interesting aspects were highlighted to suggest possible applications for drones in further marine engineering studies while promoting drone use in the field.

Chapter 2: Literature Study

2.1 Aerial Photography

2.1.1 Brief History

The first successful aerial photograph was taken as far back as 1858 by French inventor Gaspard-Félix Tournachon who went up in a balloon and photographed Paris (Editorial Board, 2019). Even back then advances strove for a smaller platform such as the kite used by M. Arthur Batut in the late 1880's to photograph Labruguiere, France and the pigeon mounted camera, designed by Julius Neubranner in 1903, which went on to be used in military surveillance. Rockets became the next innovation for launching aerial cameras, with even Alfred Nobel, after whom the Nobel prize was named, developing the first rocket camera (Baumann, 2014).

All of this was soon replaced by aeroplanes after L.P. Bonvillain took the first aerial photograph over Italy by an aircraft piloted by Wilbur Wright in 1908 (Madeira & Green, 2016). World War 1 drove advances in plane mounted photography to provide up to date maps such as the camera developed by Sherman M. Fairchild which reduced distortion and motion blur from the speed of the plane as well as including an intervalometer which allowed for photos to be taken at any set interval (Baumann, 2014).

Fairchild took his camera developed for the military and applied it commercially to map Manhattan Island which proved its usefulness for both local government and business in New York. He quickly built a successful aerial photography company working on projects such as mapping over 510 square miles of the Canadian wilderness, which further engrained the usefulness of aerial photography (Baumann, 2014).

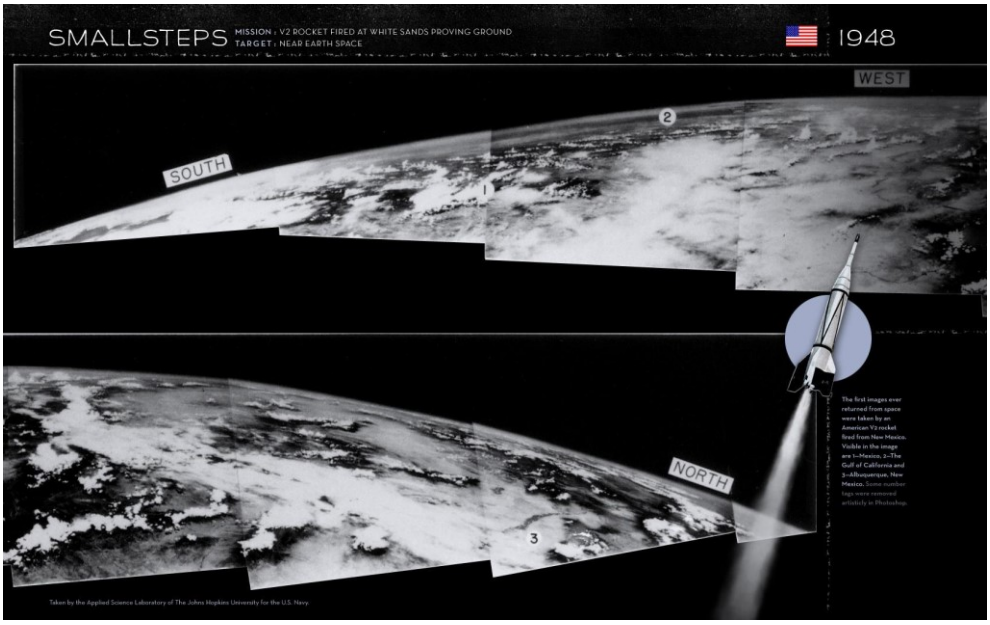

Figure 2-1: First Pictures of Earth From 161 km in Space (NASA, 2015)

Our view of the Earth was taken to new heights in 1935 when Captain Albert Stevens took a balloon named “The Explorer II” up to an altitude of 72 395 feet (22 066 m) which gave us the first view of the curvature of the Earth (Madeira & Green, 2016). The first image from space was then taken in 1946 by a V-2 rocket launched from the White Sands Missile Range (Reichhardt, 2006) shown in Figure 2-1 above.

According to the National Geo-spatial Information (NGI) website (NGI, 2013a), the first aerial photographs of South Africa in their archives go back to the 1930’s and by the 1950’s the whole country had been mapped using aerial photography from aeroplanes flying approximately 4570 m above ground. The entire country is remapped every 5-7 years using film cameras up until 2008 at which point NGI switched over to digital cameras (NGI, 2013a). Between 2008 and 2017 NGI had used an Intergraph DMC digital camera which has an image resolution with a pixel corresponding to a distance of 0.5 m on the ground, or commonly referred to as Ground Sample Distance (GSD), and then increasing the resolution to a GSD of 0.25 m since 2017 with the intention of covering the entire country every 5 years (NGI, 2013b).

Drone technology has its roots back in World War I where, in 1916, the British Royal Air Force attempted to develop a rudimentary remote-controlled unmanned aircraft. Named the Ruston Proctor Aerial Target, they hoped it would counter the German Zeppelins. The project was abandoned after a number of failed launches leaving the Americans to develop a functioning aircraft a year later called the Hewitt-Sperry Automatic Airplane (Ford, 2018).

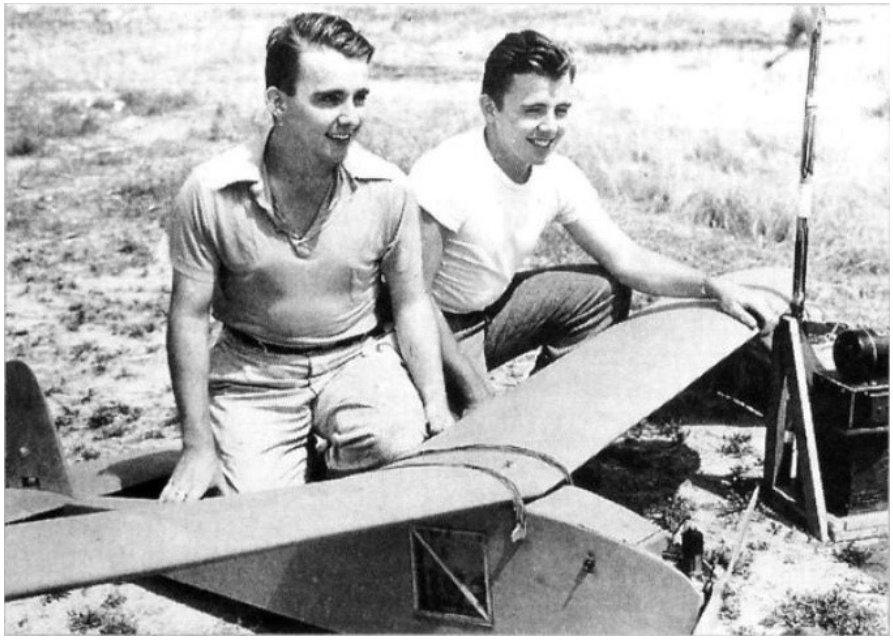

Figure 2-2: Walt and Bill Good Holding their Model Aircraft "the Guff" (Gudaitis, 1994)

Hobbyists had access to remote control model aircraft since the development of “the Guff” in 1939 (Gudaitis, 1994) which, by the 1960’s, became a popular hobby all over the world thanks to advancements in transistor technology and the models being sold in easy to build kits (Dormehl, 2018). A picture of Walt and Bill Good with "the Guff" can be seen in Figure 2-2 above.

Predominately fixed wing drones continued to be developed for military use until 2006 where the government sector found applications such as disaster relief and the commercial sector realised its use in surveying as well as applications such as spraying pesticide (Ford, 2018).

The quadcopter layout of the remote controlled aircraft used in this thesis was first released as a toy in 1991 called the Keyence Gyrosaucer II E-570 (Turi, 2014). However, it did not take off until the Dragonflyer quad helicopter gained some fame in the 1999 “Inspector Gadget” movie (Darack, 2017). The Chinese based company, DJI, which as of 2018 had approximately 74% of the market share (French, 2018), released their first quadcopter named the Phantom in 2013 and the name DJI quickly became synonymous with drones. They have become the market leader targeting expensive commercial drones for industry, such as the Inspire 2, and the Mavic Air, which is more accessible to the public; both of which have been tested as part of this thesis.

2.1.2 Drone Positioning

Drones rely on the GPS positioning network to navigate themselves especially in recent years where they can follow a predefined set of coordinates which are loaded onto the drone prior to launch. In the case of the Mavic Air and the Inspire 2, DJI has fitted a duel GPS receiver which is able to use the US Army GPS satellite network as well as the Russian GLONASS satellite network, hoping that it will be able to achieve a high positioning accuracy wherever in the world the user wishes to fly (DJI, 2018a).

In addition to GPS both drones are fitted with downward facing cameras which can detect horizontal movement by comparing the patterns from one frame to the next and hence prevent drift of the aircraft. These cameras are in a stereoscopic arrangement which also provides altitude measurements over and above the inbuilt altimeter which is based on a barometer sensor. The Inspire 2 also has a downward facing ultrasonic sensor which provides even more accurate altitude measurements even in low light situations. A summary of the positioning systems and performance of each drone can be found in Table 2-1 below:

Table 2-1: DJI Positioning Systems (DJI, 2019a).

Drone	**Mavic Air**	**Inspire 2**
Global Navigation Satellite System (GNSS)		
Provider	GPS + GLONASS	GPS + GLONASS
Downward Vision Sensing System		
Altitude Range:	0.1 - 8 m	0.1 - 5 m
Operating Range:	0.5 - 30 m	<10 m
Hovering Accuracy Range		
	Vertical:	
GPS Alone	±0.5 m	±0.5 m
GPS & Vision System	±0.1 m	±0.1 m
	Horizontal:	
GPS Alone	±1.5 m	±1.5 m
GPS & Vision System	±0.1 m	±0.3 m

The GPS reading will then be recorded in the metadata of each image taken by the drone. This can then be used to position each image from a sequence of images to get a time-series. The altitude data can also be used to scale the image. The GPS accuracy range, ±1.5 m, reported by DJI may not be enough for measuring currents as the vision system will not function over water (DJI, 2018a). This GPS error is due to several factors such as atmospheric conditions, signal interference or an unavailability of satellites at the time (U.S. Air Force, 2017).

DJI released the Phantom 4 RTK early in 2019 which aims to address this problem and is aimed at more accurate surveying applications. The drone is equipped with a real-time kinematic (RTK) positioning unit which, similar to a GPS survey staff, connects to either a local network or a base station which provides real time error data. This then reduces the hovering accuracy range to a mere 0.01m horizontally and 0.015m vertically (Mulakala, 2019) although this comes with an expected retail price of approximately €5,700 (DJI, 2018b).

2.1.3 Orthorectifying and Orienting Aerial Images

For an image taken from above to accurately represent the land below orthorectification needs to take place, then the image needs to be oriented using its GPS coordinates and finally rotated as per the compass reading. Orthorectification is the process of removing any distortion generated by the cameras lenses as well as any tilt of the camera. This distortion along with any topographical changes will cause details at the edges of the image to be more distorted than directly below the aircraft (Satellite Imaging Corp, 2017). This effect can be seen in Figure 2-3 which is a test shot carried out for the DJI Mavic Air. Note how the gridline appears to bend away at the edges but the onboard software corrects for the distortion in the centre of the image where the grid is seen as parallel.

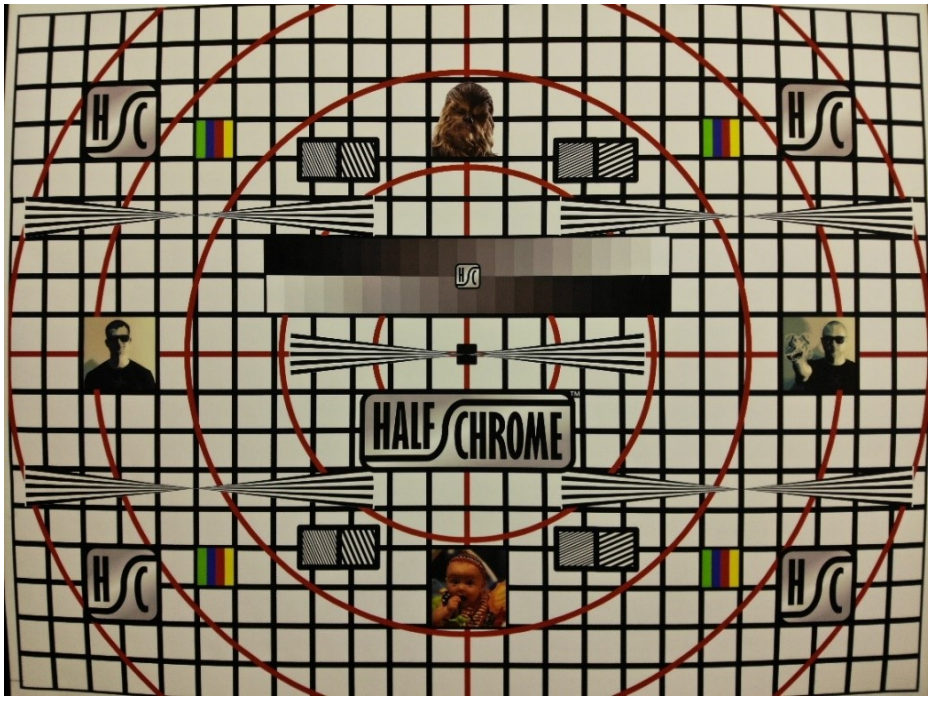

Figure 2-3: DJI Mavic Air Camera Test Shot (Half Chrome, 2018)

The distortion effect can be seen in the corners of the image above where the edges seem to curl away from the camera. However, the on-board image processing does correct some distortion in the centre of the image based on its lens profile. For aerial mapping this distortion is further exacerbated by drastic changes in topography as seen in Figure 2-4 below where two equal horizontal distances on the ground will appear different in the image, or the side of a tall building will be shown.

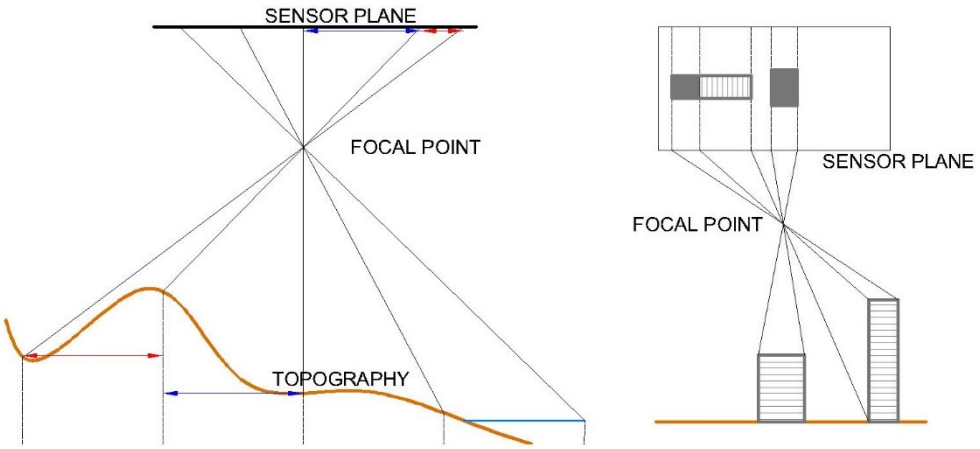

Figure 2-4: Examples of Distortion in Aerial Photographs Adapted from (Devi & Veena, 2014)

In order to correct for these errors software packages such as Pix4D, Agisoft Metashape, DroneDeploy and ESRI Drone2Map use photogrammetry to generate a digital elevation model (DEM) which can then be used to overlay the images and provide an accurate ortho-mosaic map (Hughes, Teuten, Starnes, Cowie, Swinfield, Humpidge, Williams, Bridge, Casey, Asque & Morris, 2018). Photogrammetry is the process by which a complex computation is carried out to pick up overlapping ground points between at least two different camera positions. The software will determine the relative coordinates of the camera and ground points to then triangulate between the two images. If enough overlapping points are available in each image, a 3 dimensional model can be built (Upadhyay, 2014). For photogrammetry where this relative position is measured between three or more images it is best if the adjacent photos overlap by at least 60 %, as seen in Figure 2-5, in order to get sufficient coverage (Kaamin, Daud, Sanik, Farah, Ahmad, Mokhtar, Ngadiman & Yahya, 2016)

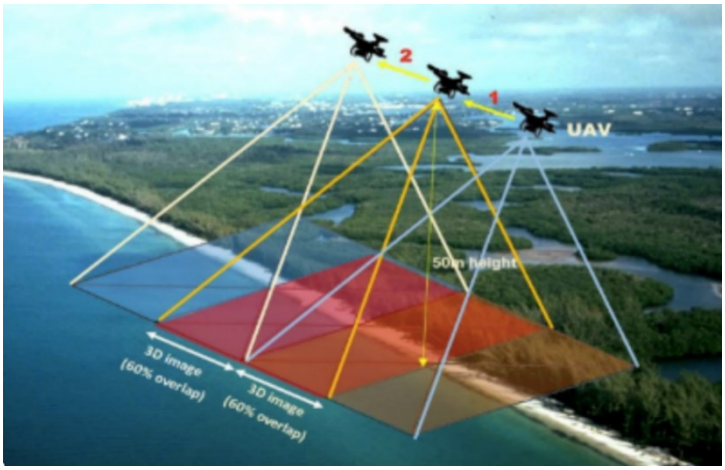

Figure 2-5: Overlapping Photographs for Aerial Photogrammetry (Kaamin *et al.*, 2016)

This is similar to the process by which our brains determine depth using our stereoscopic vision by intuitively measuring the change in position of the image seen by our left eye compared to our right eye. The distance to the object (D) can be calculated using the known field of view (φ_0 or FOV) and the distance (B) between the two cameras (S_L & S_R) as well as the observed object angles (φ_1 & φ_2) as shown in Figure 2-6 below. In the case of drone aerial photography, the two camera positions would be the same camera at two different times.

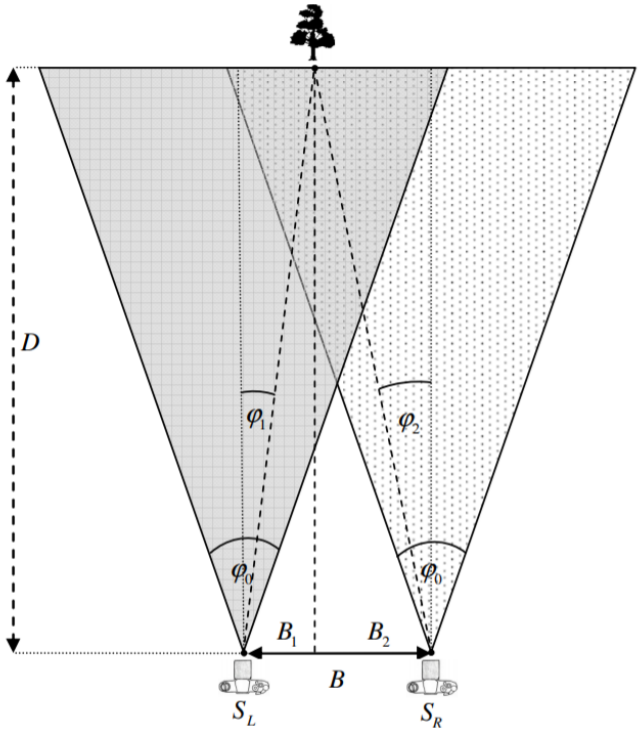

Figure 2-6: Stereoscopic Vision (Mrovlje1 & Vrančić, 2008)

The software will then use the on-board GPS to scale and locate the map. The inherent errors in GPS, discussed in section 2.1.2 above, only allow for this method to provide a rough location. Tests of length measurements carried out by one of the software developers mentioned above achieved an average 1.1% error (Putch, 2017). This can be improved further by making use of at least 5 ground control points (GCP's) which are static points placed around the study area, visible from above (see Figure 2-7) and have known coordinates. These points are then included in the photogrammetry calculations such that the DTM fits these points providing correct geographic location and scaling (Hughes *et al.*, 2018) with a tenfold improvement on accuracy (Putch, 2017).

Figure 2-7: Examples of GCP's (Baker, 2016)

The issue with this method is that if there is movement in the subject being mapped, i.e. water, then the algorithms cannot find matching points between images and the 3D model can become distorted or if no consistent points are available, photogrammetry will not be possible (Hughes *et al.*, 2018). An example of this can be seen in Figure 2-8 below processed with the free to use software Maps Made Easy which highlights the elevation errors where water is present.

Figure 2-8: Example DEM of the Monwabisi Spur.

2.1.4 Conventional Drone Applications

Drones have become widely used in the commercial field, most notably aerial videography where filmmakers are now able to get incredible footage from a vantage point previously only attainable using an expensive to run helicopter. In the agriculture sector drones are used to count plants and even estimate the plants health (Drone Deploy, 2018a) with thermal imaging cameras available for the DJI inspire (DJI, 2019b). Similar thermal imaging cameras on drones have been used to detect water leaks in underground pipelines (Australian Water Association, 2015). Amazon has stated that they are working on using drones to deliver packages (BBC News, 2016) and in South African game parks, drones have been used to prevent poaching (Air Shepherd, 2019).

In surveying, drones have become an integral tool with photogrammetric surveys being a standard quick method for providing a detailed map and 3D model of an area with reported accuracies of 4cm horizontal and 7cm vertically (Buczkowski, 2017).

The construction and engineering industries have taken to drone use the most in recent times with a year on year growth of 239% by May 2018, according to the mapping software company Drone Deploy. From site safety, to progress tracking and quality assurance, drones have become commonplace on site (Drone Deploy, 2018b).

2.1.5 Existing Drone Coastal Applications

Existing applications have focussed on longer term monitoring such as the Volta Delta, Ghana where drones have been used to monitor flooding and coastal erosion (Appeaning Addo, Jayson-Quashigah,

Codjoe & Martey, 2018) and in Truc Vert, SW France, low-cost drones have been used to monitor coastal dunes and assist with dune management (Laporte-Fauret, Marieu, Castelle, Michalet, Bujan & Rosebery, 2019). These monitoring studies rely on the mapping functionality of aerial photography to create a snapshot in time in the form of a DTM and orthomosaic photograph which can then be compared in software such as ArcGIS®(Long, Millescamps, Guillot, Pouget & Bertin, 2016).

A more dynamic application more in line with measuring currents has been successfully tested by Le Roux (2018) who used drones to measure effluent dispersion plumes of marine outfalls through the surf zone.

At the time of this thesis no similar use of drones measuring real-time coastal processes in motion has been found.

2.1.6 Image Recognition

Image recognition has been widely used as an effective method for tracking moving objects by comparing similarities and differences between two consecutive frames (Kalantar, Mansor, Abdul Halin, Shafri & Zand, 2017). One such common application is for pedestrian and vehicular tracking, where an algorithm detects, categorises and tracks objects from a network of citywide street mounted surveillance cameras (Keaikitse, 2014). Piepmeier *et al.* (2006) were able to track the surface elevation of water using stereoscopic cameras which allowed them to determine wave characteristics. The algorithms that process the images are vulnerable to noise which can be created by insufficient light, shadows and reflections (Viriyakijja & Chinnarasri, 2015) which are especially characteristic of water with its smooth reflective surface (Piepmeier *et al.*, 2006). Aerial images have been used by Benbow *et al.* (2017) to study breaking waves by observing texture patterns on the surface due to air entrained by wave action creating foam on the water surface.

With the advent of machine learning, systems can be taught to provide information from an image without the need for complex transformations used previously. It is possible to take video surveillance of the beach and train an algorithm to track individual waves to provide wave data such as wave period, wave velocity and the length of breakers (Stringari, Harris & Power, 2019). An example output is provided in Figure 2-9 below.

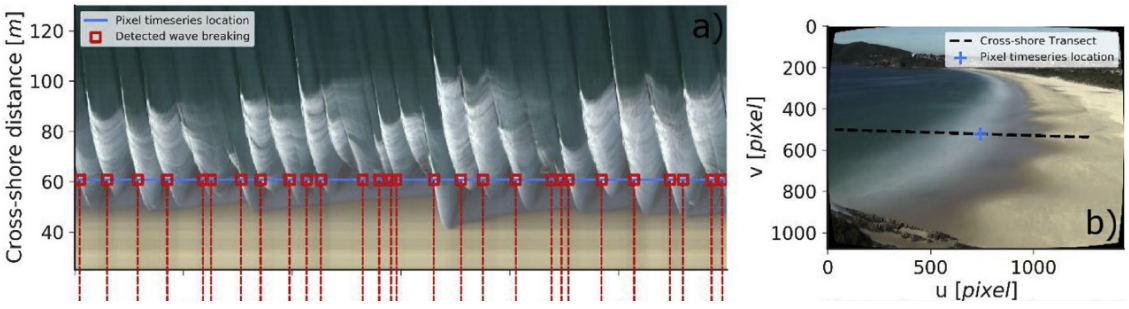

Figure 2-9: Machine Learning Input (left) from Beach Surveillance (right) to Determine Wave Peaks Over Time (Stringari et al., 2019).

2.1.7 Legal Requirements

While the use of drones is relatively new, the growth has drastically increased in recent years, such that Regulatory bodies, i.e. the Civil Aviation Authority (CAA) of South Africa, have not had an opportunity to adequately assess the risks involved and hence stringent restrictions have been placed on drone use. The CAA has defined a remotely piloted aircraft (RPA) in legislation as an "unmanned aircraft which is piloted from a remote pilot station…" which may be used for private use where there is no commercial outcome, interest or gain, while for all other uses RPA's must be operated in terms of Part 101 of the South African Civil Aviation Requirements (SACAA, 2017a).

All drone (RPA) operations are restricted to flying out of controlled, restricted or prohibited airspace and 10km away from an aerodrome (including helipad). The operator must leave a 50m buffer between the aircraft and any person or public road and needs to gain permission from the property owner before the operator wishes to fly over. Flights are also restricted to daylight and clear weather conditions. For private operations the drone weight is restricted to a maximum of 7kg, has to remain within line of sight at all times and may not fly over 150 feet above the ground (SACAA, 2017b). Should an operator wish to charge remuneration or deviate from the above restrictions, he/she is required to acquire the following certifications (SACAA, 2015):

- Air Service Licence
- RPAS Operators Certificate
- RPAS Letter of Approval
- Remote Pilot Licence
- Certificate of Registration

Based on conversations with operators in the industry, this has proven to be a costly procedure with the whole process costing in excess of R100 000 and taking months to get final approvals. Therefore, the number of South African companies with a RPAS Operators Certificate is currently limited to 38 (SACAA, 2019). Other countries such as New Zealand, do not distinguish between private and commercial operations and do not require certification, providing the drone is below 25kg and is flown within the set guidelines (Airshare, 2019).

Regulations will also need to be updated as drones become safer with advancements such as the AirSense technology released by DJI which alerts drone pilots if an aircraft is on a collision course with the drone and allows for him/her to take evasive action (DJI, 2019c).

As there is no intended commercial gain for this thesis there is no need for any specific certification in order to gather the required data.

2.2 Nearshore Currents

Nearshore currents are the driving process behind many engineering concerns including movement of sediment along the coastline, discharges into the coastline being carried by currents effecting dispersion and public safety when swimming (Olsson, 2004). Consequently, getting a better understanding of site-specific current magnitudes and flowlines is imperative to the success of any project.

2.2.1 Nearshore Current Generation

Nearshore currents are generated by a combination of components which themselves are each interconnected(U.S. Army Corps of Engineers, 2003), namely:

u_w	Steady current driven by breaking waves
u_t	Tidal current
u_a	Wind-driven current
u_o & u_I	Oscillatory flows due to wind waves and infragravity waves.

These components combine as follows:

$$u = u_w + u_t + u_a + u_o + u_I \qquad (2\text{-}1)$$

The currents can be illustrated on a time series plot seen in Figure 2-10 below which shows the velocity of the currents in the cross shore (U) and longshore (V) directions. The short period oscillations are due to the wind-wave orbital motion while the longer period oscillations are caused by infragravity waves and the overall average currents are due to the breaking waves, tides and wind (U.S. Army Corps of Engineers, 2003).

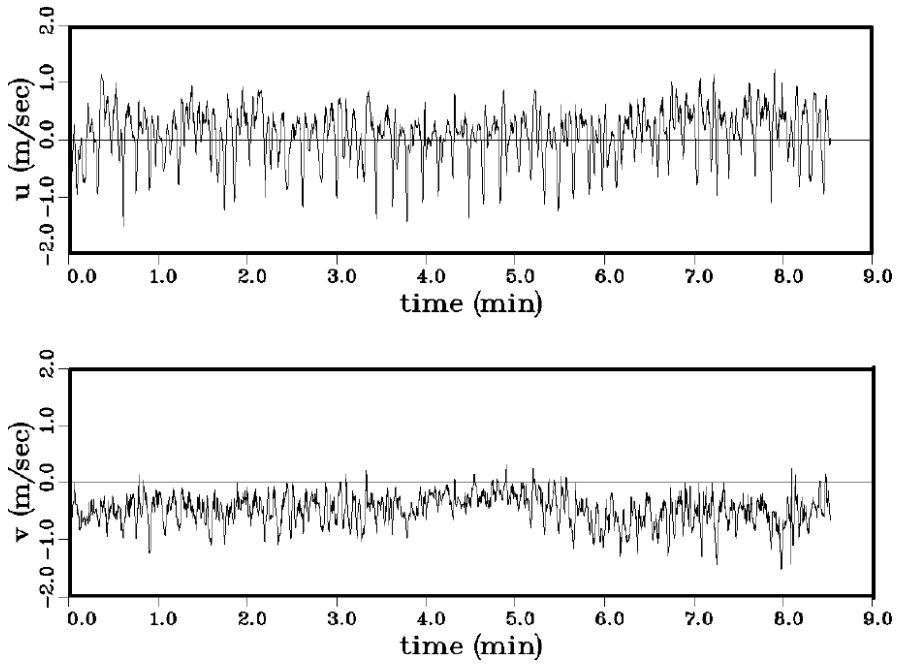

Figure 2-10: Measured Flow Velocities (U.S. Army Corps of Engineers, 2003)

In the surf zone, energy is dissipated as the waves break on the shore, causing a momentum flux gradient which in turn leads to wave setup (Kistner, 2016). When there is an angle between the

incoming wave crests and the shoreline, defined as α_b, a current develops along the shore from the waves breaking at an angle to the shoreline. This is caused by the component of the radiation stresses, perpendicular to the shoreline, driving the longshore current (Mangor, 2019).

The velocity distribution of these longshore currents increases quickly from the beach to a maximum within the surf zone (equation (2-2)) and then soon decreases beyond this (see Figure 2-11 showing a large angle α_b between the shore and the incoming waves). During normal conditions these currents will typically have a mean value of 0.3 m/s or less (U.S. Army Corps of Engineers, 2003).

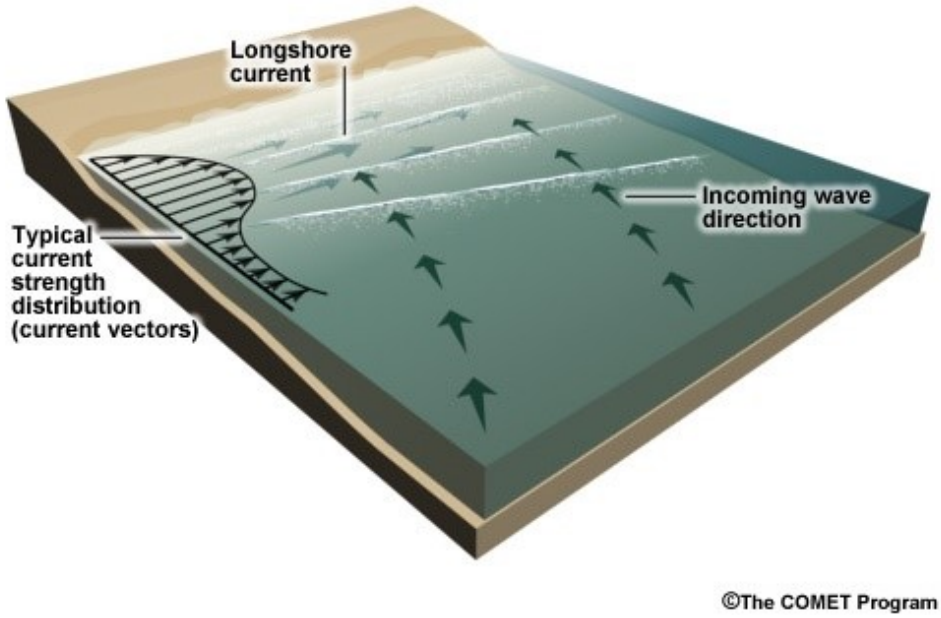

Figure 2-11: Typical Cross Shore Current Distribution (Plant, Long, Dalyander, Thompson & Raabe, 2013)

The maximum current velocity in the surf zone can be characterised by Komar and Inman with the following equation (U.S. Army Corps of Engineers, 2003). This illustrates that as the wave height increases, so does the current velocity.

$$V_{mid} = 1.17\sqrt{g\,H_{rms.b}}\sin\boldsymbol{\alpha_b}\cos\boldsymbol{\alpha_b} \qquad (2\text{-}2)$$

Where:

$H_{rms.b}$ = Root-mean-square wave height at breaking (m)

When the incoming waves are more shore normal (a smaller α_b or equal to 0) the currents tend to divert causing circular cells with currents running longshore until meeting an opposing longshore current where they both turn seawards, forming a rip current in both directions perpendicular to the shoreline, seen in Figure 2-12.

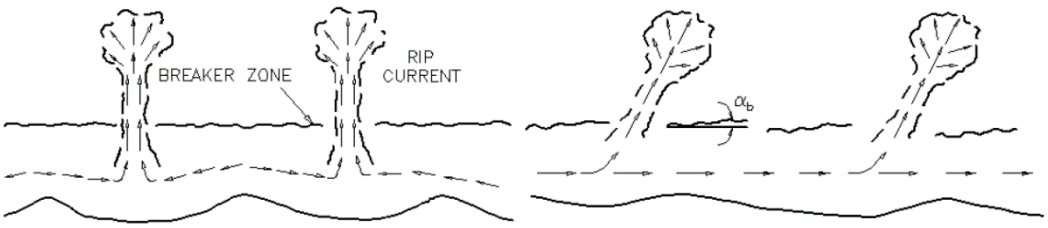

Figure 2-12: Nearshore Circulation Systems (U.S. Army Corps of Engineers, 2003)

The velocity of these longshore currents will increase from the point of diversion to a maximum where the rip current forms. A variation in wave setup can generate cell circulation which is often seen when an obstacle, such as a breakwater, creates a shelter from incoming waves (U.S. Army Corps of Engineers, 2003) creating cell circulation similar to that shown in Figure 2-13 below. This is specifically applicable at Monwabisi where the eastern breakwater shelters the predominant wave climate coming into False Bay.

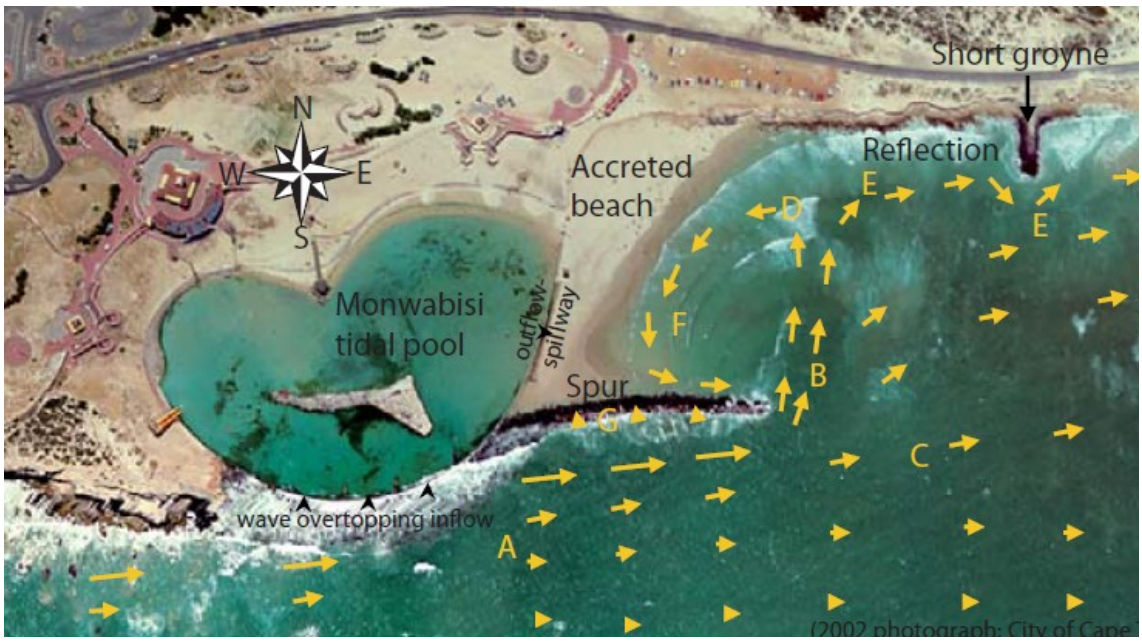

Figure 2-13: Schematic of Currents at Monwabisi (Theron & Schoonees, 2007)

The Agulhas Current and Benguela which are the predominant currents flowing along the South African coasts, has little effect on the nearshore currents at Monwabisi within False Bay. The Agulhas current moves away from the East Coast at approximately port Elizabeth, continuing southerly along the Agulhas bank (Roberts, van der Lingen, Whittle & van den Berg, 2010) while the Benguela current upwells between Cape Agulhas and Cape Frio (Hutchings, van der Lingen, Shannon, Crawford, Verheye, Bartholomae, van der Plas, Louw, Kreiner, Ostrowski, Fidel, Barlow, Lamont, Coetzee, Shillington, Veitch, Currie & Monteiro, 2009) North West of False Bay.

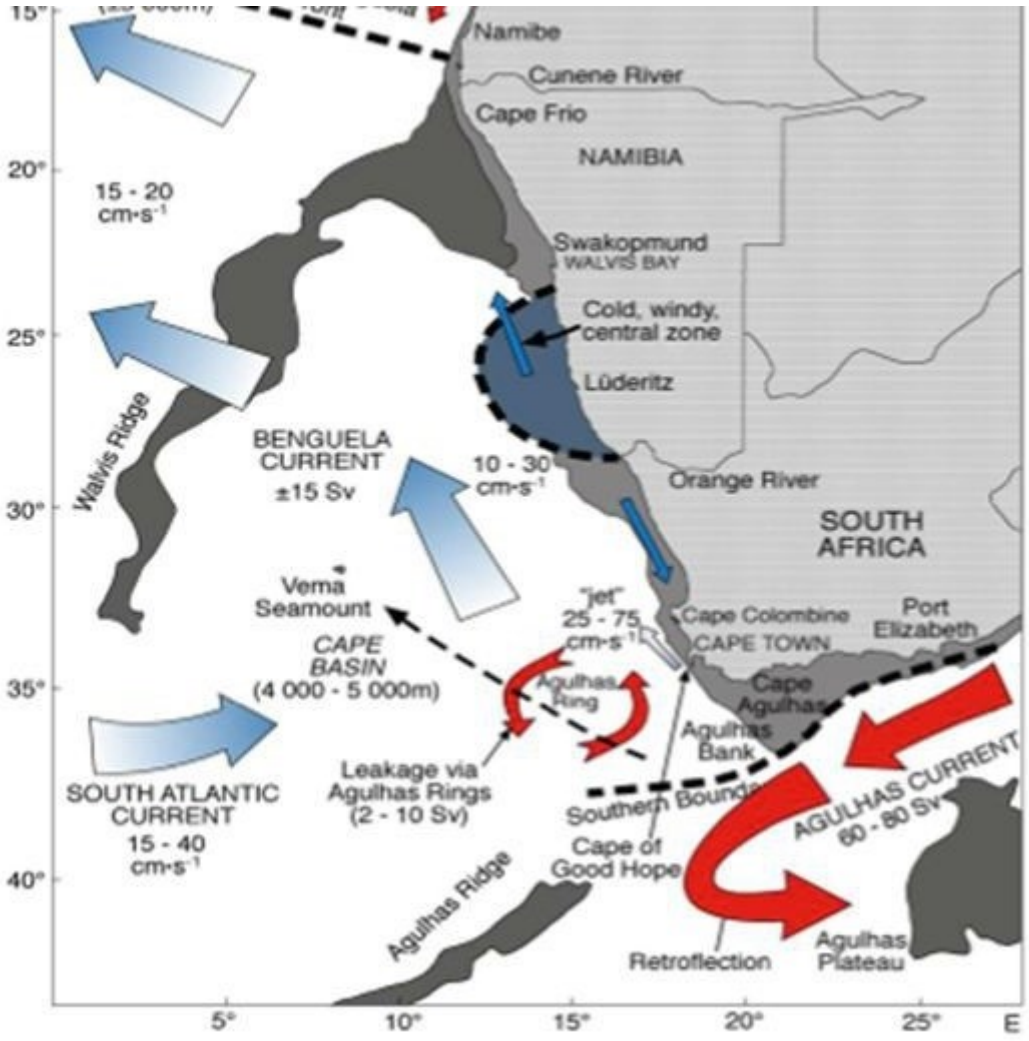

Figure 2-14: Currents off Southern Africa (Hamukuaya, Willemse, O'Toole & Attwood, 2013)

Coleman noted that the predominant large scale currents generated within False Bay were wind-driven, causing a clockwise (or cyclonic) gyre with a south-easterly wind (see Figure 2-15) while north-westerly winds would cause a spatially-uniform surface current field flowing out of the bay. However, he did note that his model did not include wave coupling which would account for wave generated longshore currents which are expected to be more significant in shallower regions of the bay (Coleman, 2019) such as Monwabisi.

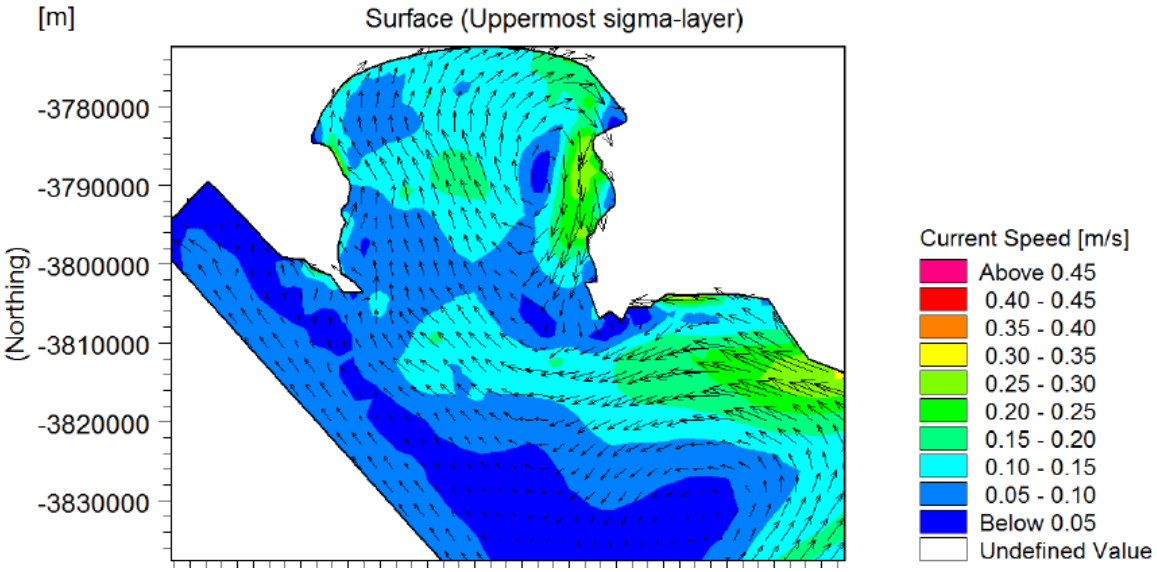

Figure 2-15: South-easterly Generated Surface Current Circulation Pattern (Coleman, 2019)

2.2.2 Vertical Velocity Distribution

Although horizontally, near-shore currents tend to vary greatly, especially where a rip current is present; vertically the velocity distribution tends to remain relatively constant (Visser, 1991) which has been confirmed in studies such as that carried out by Shin *et al.,* (2017) and shown in Figure 2-16. If an undertow is present, the shore normal currents may vary as depth increases with a strong offshore current near the seabed (U.S. Army Corps of Engineers, 2003). However, undertows are typically present when the nearshore bathymetry forms a uniform slope along the beach (Aagaard & Vinther, 2008) and hence would not be expected in Monwabisi Bay as the seabed is noted to contain rocky outcrops (Theron, Van Tonder, Blake, Barwell, Schoonees, Van Dulm & Vonk, 1997).

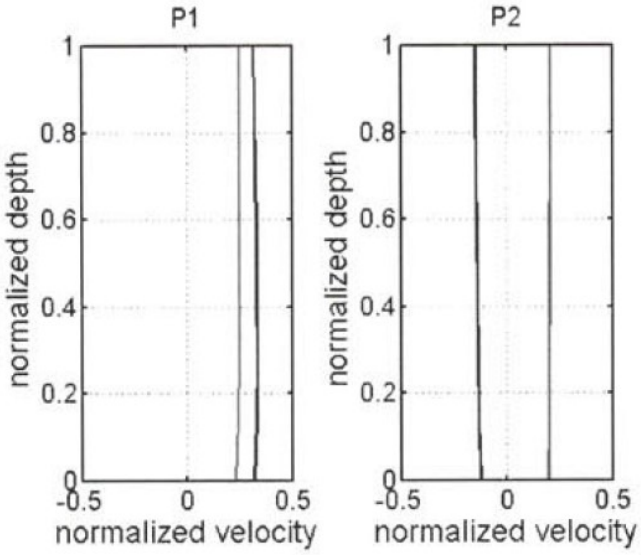

Figure 2-16: Example Vertical Distribution of Horizontal Current Velocity (Shin et al., 2017)

2.2.3 Rip Current Safety

Rip current related drownings are considered the most serious threat to beach goers, with more deaths attributed to rip current drownings than floods, hurricanes and tornadoes (Fietemeyer, 2014). It is estimated that annually there are 50 drowning related rip currents in Australia (Short & Hogan, 1994), 100 in the United States of America (Fallon, Lai & Leatherman, 2018) and 30 in Korea (Shin *et al.*, 2017). The World Health Organisation prioritises drowning as a leading killer worldwide with a total number of deaths at 320 000 in 2016 (WHO, 2019). South Africa is no exception with 1 411 deaths due to drowning in 2016 (Statistics South Africa, 2016) and reports coming out, nearly every year, of December/January beach drownings (Pijoos, 2016; Savides, 2017; Daniel, 2018) which is the period when the most drownings occur (Timeslive, 2017). From discussions with the NSRI there were 79 fatal drownings in 2017 and 111 in 2018 nationally (including inland) with 5 and 28 being reported as rip currents for these years respectively. Monwabisi, the study area, has been known for its dangerous rip currents with 10 drownings reported between 2011 and 2016 (Kistner, 2016), and as recent as 2018, three men drowned during a baptism ceremony after two men were swept out by a suspected rip current and then a third went after them (Etheridge, 2018).

Education is key to preventing these deaths as one's initial instinct would be to swim back to shore, which will be against the flow and hence tire one out to exhaustion. Informative posters, such as the one provided by the NSRI in Figure 2-17 below, provides guidance to the conventional wisdom as to what to do if caught in a rip current: Stay calm, swim slowly and go with the flow until the current dissipates where one can swim around the rip to use the waves to return to the beach (NSRI, 2018).

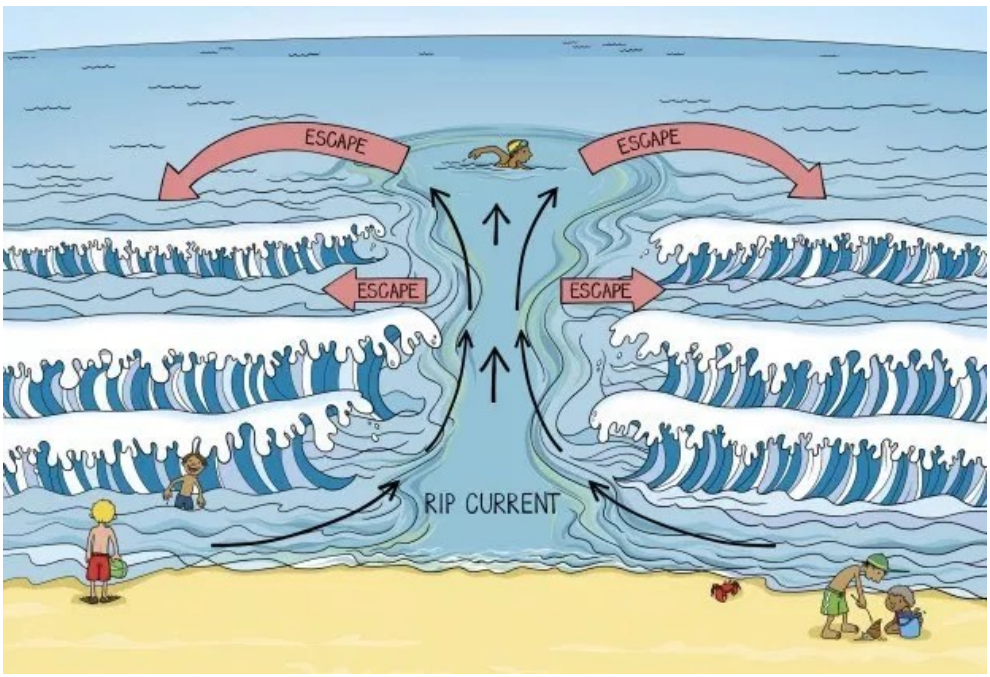

Figure 2-17: Rip Current Escape Figure (NSRI, 2018)

This approach was contested when Jamie MacMahan a rip current expert at the Naval Postgraduate School in Monterey, and strong swimmer himself found that escaping by swimming sideways led

him to be resisted by the rip current until he swam in the opposite direction (Ferry, 2016). He then co-authored a study which carried out a current survey using GPS Drifters as well as a number of GPS-tracked human participants to attempt to determine which escape method is preferable. However, a "silver bullet" approach could not be determined. The study recommended further studies to identify the hazards relating to rip currents and better inform the public on safe water usage (McCarroll, Brander, MacMahan, Turner, Reniers, Brown, Bradstreet & Sherker, 2014) which will inevitably require innovative methods for measuring currents.

2.3 Existing Methods for Current Measurements

Methods for measuring sea properties are generally split up into either Lagrangian or Eulerian measurements (Inch, 2014):

- Lagrangian measurements sample the movement of a particle of water hence floating along with the current. I.e. the GPS Drifter and Dye Tracer methods described below.
- Eulerian measurements typically sample a static point in the water body. I.e. Acoustic Doppler Current Profiler (ADCP).

2.3.1 GPS Drifter

A GPS Drifter, as seen in Figure 2-18 below, unit is a floating unit which contains a GPS unit which either records its location or allows for it to be tracked as it floats on the currents (Inch, 2014). The benefit of the GPS drifter is that it collects data on the current velocity as well as the flow path (Olsson, 2004) however each unit can be expensive depending on the GPS unit used (Austin & Atkinson, 2004) and needs to be recovered manually once they return back to the beach or exit the study area (Scott, Austin, Masselink & Russell, 2016) (Olsson, 2004).

Figure 2-18: Example of a GPS Drifter System (Scott et al., 2016)

A similar study achieved a spatial accuracy of 0.4 m horizontally and 0.01 m/s in velocity while finding a wind slippage effect of less than 0.08 m/s when the wind velocity was below 7.2 m/s. The drifter was fitted with dampening plates underneath which extended 450 mm into the water to prevent the float surfing down waves and their tests found that the GPS floats achieved similar results to dye tracer tests (Scott *et al.*, 2016). A parachute drogue, seen in Figure 2-19 below, can also be fitted to the underside of the drifter to prevent surfing. Results with this setup have been tested and shown to be on average within 5% of depth averaged measurements from fixed Eulerian instruments (Olsson, 2004).

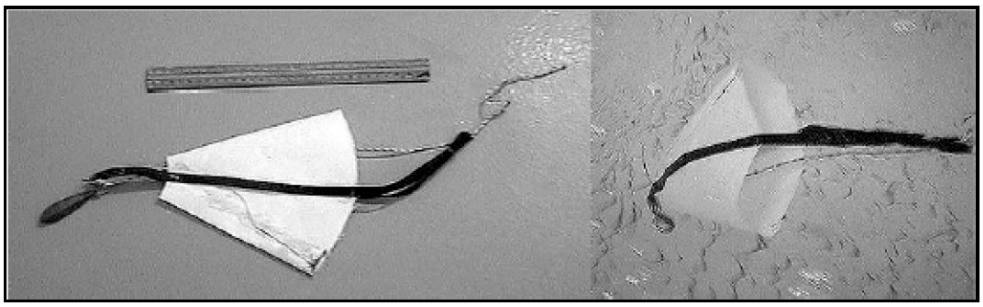

Figure 2-19: Parachute Drogue (Olsson, 2004).

2.3.2 Dye Tracers

Measuring currents using dye involves releasing a highly visible compound such as fluorescene into the current and then observing its movement through the water column. Previously a land based camera would observe this movement over time but more recently drones have been used to track the movement (Leatherman, 2017), as seen in Figure 2-20. At times the use of dye tracers may require obtaining a permit prior to use and in South Africa “artificial tracer testing” is regulated by the National Water Act (Act 36 of 1998) (Wolkersdorfer & LeBlanc, 2012). Releasing a bright substance into the sea will attract unwanted attention of the public.

Figure 2-20: Dye Tracer as Captured from Aerial Drone (Leatherman, 2017)

2.3.3 ADCP Current Meters

An Acoustic Doppler Current Profiler (ADCP) or Acoustic Wave Current Profiler (AWAC), seen in Figure 2-21 below, and similar Acoustic Doppler Velocimeter (ADV) are all based on the same principle that a frequency will be shifted as it is reflected off a moving object, like a train's horn changing pitch as it goes past you on the tracks (Palmer, 2002). All three instruments send out acoustic wave pulses via transducers which then reflect off passing currents and return to the instrument and can provide readings in three axes depending on the setup. The AWAC is similar to the ADCP with the addition of a vertical transducer which measures the sea surface directly and allowing for wave measurements to be recorded (Nortek, 2019) although similar capabilities are available to a ADCP with the addition of a pressure sensor (Olsson, 2004).

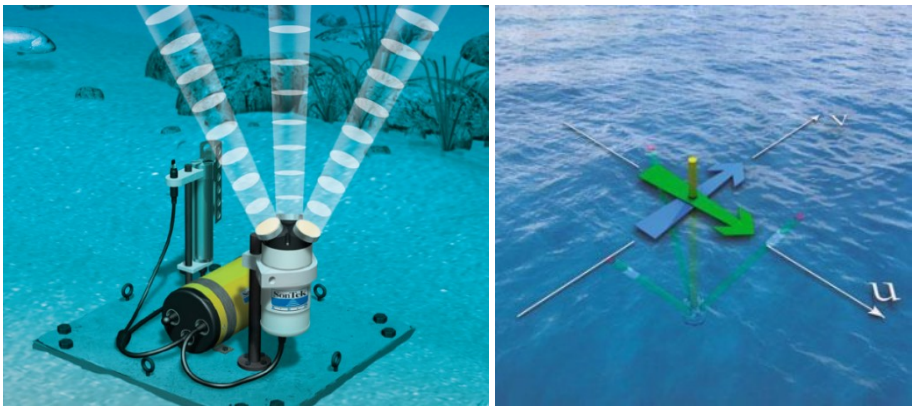

Figure 2-21: ADCP Seafloor Deployment (left) (SonTek, 2017) and AWAC Beam Arrangement (right) (Sutron, 2019)

The ADCP and AWAC measure a current profile over a long distance of up to several hundred metres, depending on the model, while the ADV takes a measurement nearby to the instrument (see Figure 2-22). This makes the ADV more suited to the turbulent currents around the nearshore zone (DOSITS, 2019). An issue with these methods is that they are prone to error in the presence of bubbles and/or suspended sediment (Inch, 2014) which may be detrimental in the near-shore surf zone.

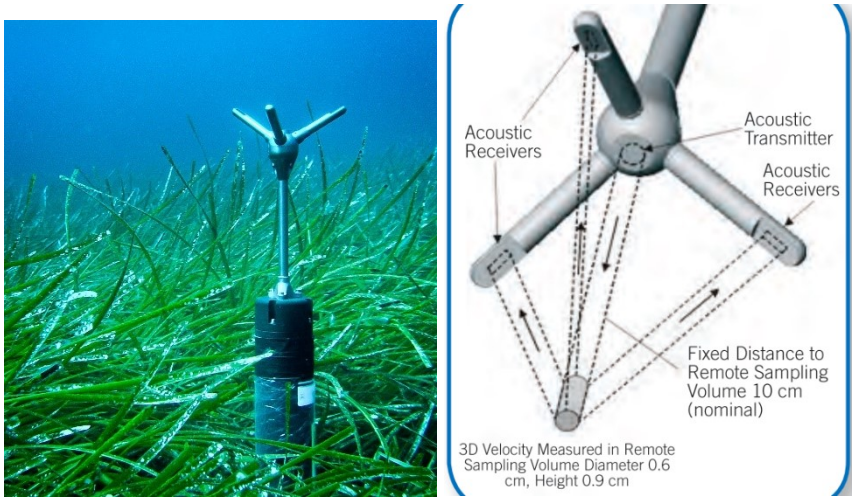

Figure 2-22: An ADC Deployment in Sea-Grass (left) (Oanes, 2011) and the Instrument Arrangement (right) (SonTek, 2010)

2.3.4 High Frequency Radar Ocean Tower

Currents and surface waves can be measured using high frequency radio signals which are transmitted from towers along the coastline, such as the tower installed on a farm near St Francis Bay, Eastern Cape by Lwandle Technologies in 2018 (CTS Heritage, 2017) shown in Figure 2-23 below. The measurements are gathered as the radio signal is reflected off waves and currents and then returns to the tower. Similar to the acoustic instruments above, the current or wave velocity near the ocean surface causes a doppler shift in the return signal that can be measured; by combining information from two or more towers, a 2-D structure of the measurements can be calculated (Roarty, 2014).

Figure 2-23: A High Frequency Ratio Ocean Tower Installed in South Africa (Actimar, 2018)

These instruments can measure up to approximately 200 km from the shore with a resolution typically ranging from 500 m to 6 km (NOAA, 2018) which does not provide enough detail to quantify rip currents (see Figure 2-24).

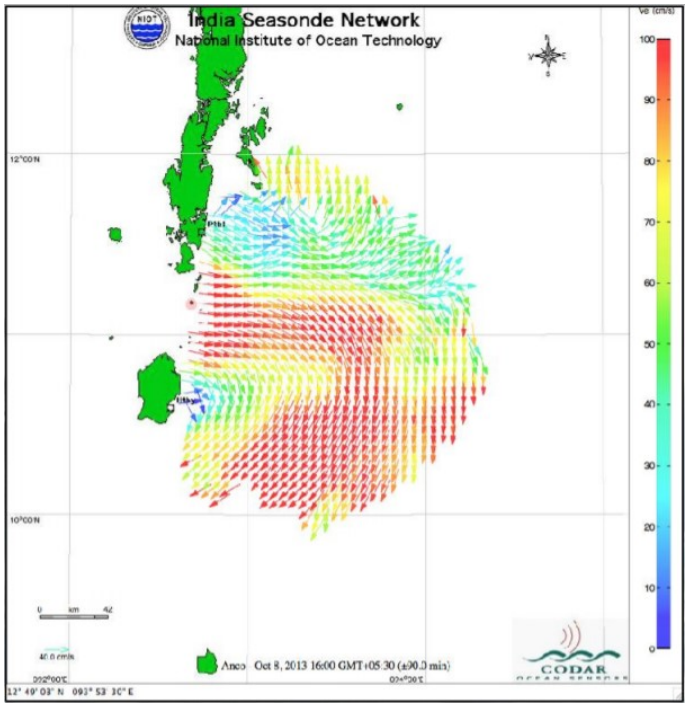

Figure 2-24: Example of HF Radar Measured Surface Current During Cyclone Crossing

2.3.5 Tilt Current Meters

Tilt current meters are comprised of a float tethered to a seabed anchor which then uses an accelerometer in the float to measure the effect of the current on the tilt of the float in relation to the anchor, as seen in Figure 2-25 below. In low currents, the float will be in a 0° position above the anchor and as the velocity increases the angle will increase proportionally. Anarde and Figlus (2017) checked the validity of results for the surf zone and determined that this type of meter provides comparable results as an ADV for low-frequency currents in low wave energy conditions.

Figure 2-25: TCM-1 Tilt Current Meter Diagram (left) and Deployment (right) (Lowell Instruments LLC, 2015)

At a price of between 1000 and 1500 USD for a TCM-1 Tilt Current Meter (Lowell Instruments LLC, n.d.) along with the relatively simple installation required, they provide a good solution for this application. However, these are Eulerian instruments and will require either more than one deployment or numerical modelling of the bay to determine flow paths.

2.3.6 Video Surveillance

Video surveillance systems involve a camera mounted at a high vantage point behind the beach which allows for the surf zone to be recorded and monitored. Systems such as the ARGUS system, developed in 1989, can quantify the spatial variability of sand bar morphology over time while the Coastal Conditions Monitoring System (CoastalCOMS) uses advanced image processing to provide environmental data for the coastline. The largest benefit of a video surveillance system is the consistency of data provided and the ability to monitor over long periods. However, there are some drawbacks such as sun glare which makes interpreting the image difficult at times (Murray, Cartwright & Tomlinson, 2013). While determining the duration and frequency of rip currents using video surveillance is achievable, estimating the magnitude of the velocity would be more complicated as distances are not constant over the entire cameras frame.

2.3.7 Satellite Remote Sensing

On a much larger scale, Satellite altimetry measurements can provide a global surface current estimate at a resolution even larger than HF radio (approximately 10km). However, these require worldwide measurements along with complex calculations. Recent advancements in sensor

capabilities allow for water body features such as temperature and colour fluctuations, seen in Figure 2-26 below, to be tracked while estimating current eddies and flow every hour at a special resolution of 500m (Sun, Song, Shao & Schlicke, 2016).

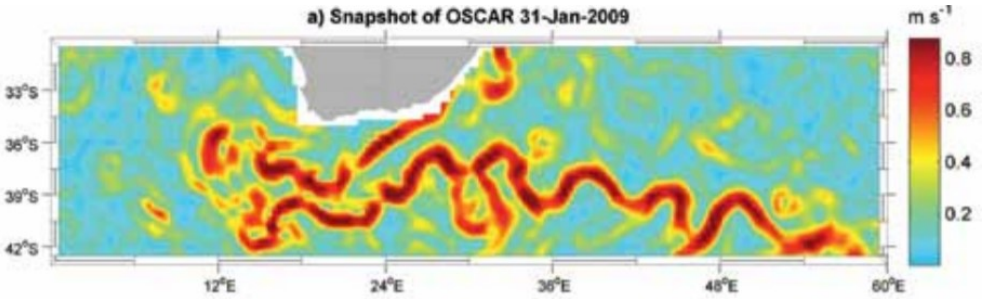

Figure 2-26: Altimetry Derived Surface Currents *(Dohan & Maximenko, 2010)*

2.4 Previous Monwabisi Studies

Monwabisi tidal pool has long been a recreational facility used by the local community. A spur, approximately 170 m long, was added seaward from Monwabisi tidal pool and was completed by February 1997. This was put in place in the hope of creating a safe bathing area adjacent to the pool while preventing excessive overtopping from the pools eastern overflow. Due to an unexpected beach response along with subsequent drownings in December 1996/January 1997, further studies were commissioned (Theron *et al.*, 1997). Theron & Schoonees also presented a paper in 2007 on the sediment transport response to the breakwater attached to a large tidal pool at the site.

The safety of the area was studied by the CSIR in 1997, then again by Kistner as part of his MSc research in 2016. The findings are summarised below.

2.4.1 CSIR: Monwabisi Beach Safety

The CSIR built on their initial 1994 study looking at the physical conditions at Monwabisi with a site investigation which included timing dye/drifter movements for limited calibration (see Figure 2-27), physical model testing, then proposed and tested some possible solutions. These solutions ranged from new groynes within the bay to creating a gap in the existing spur. After initial testing, a new T groyne (see Figure 2-28) between the spur and the existing groyne was tested more extensively which illustrated a reduced overall current magnitude, although it could possibly increase the beach width and then exacerbate the windblown sand problem in the area. The tests showed that there are always risks to bathers around near-shore groyne type structures. These risks cannot be eliminated without a larger scale intervention of an offshore structure. Therefore, keeping the layout as is should be considered along with more stringent beach management strategies (Theron *et al.*, 1997).

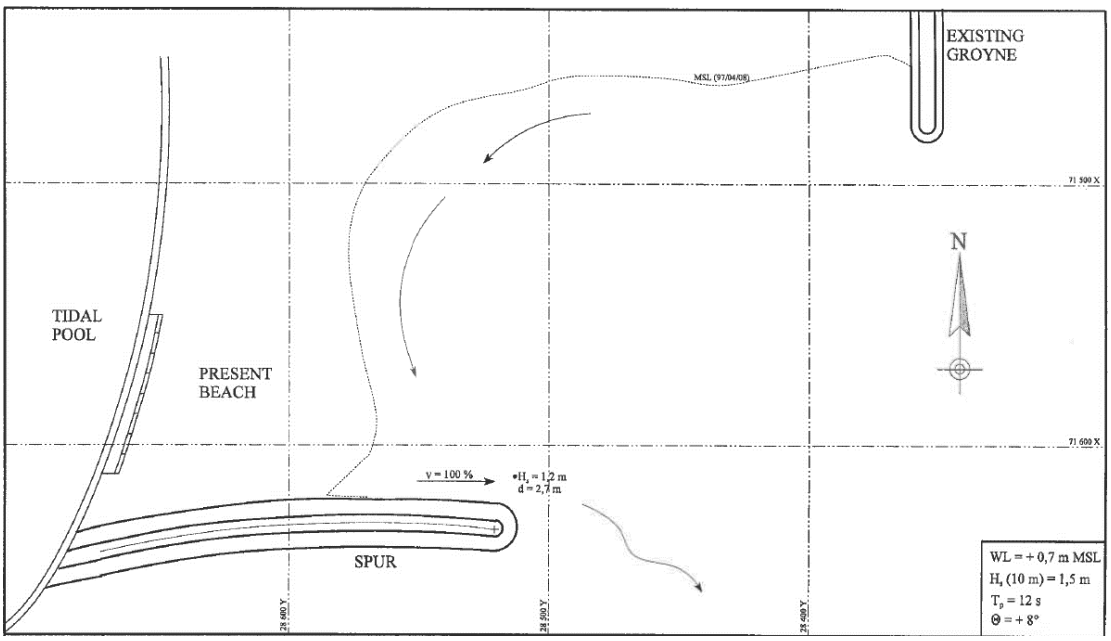

Figure 2-27: Physical Model Calibration Test Layout (Theron et al., 1997)

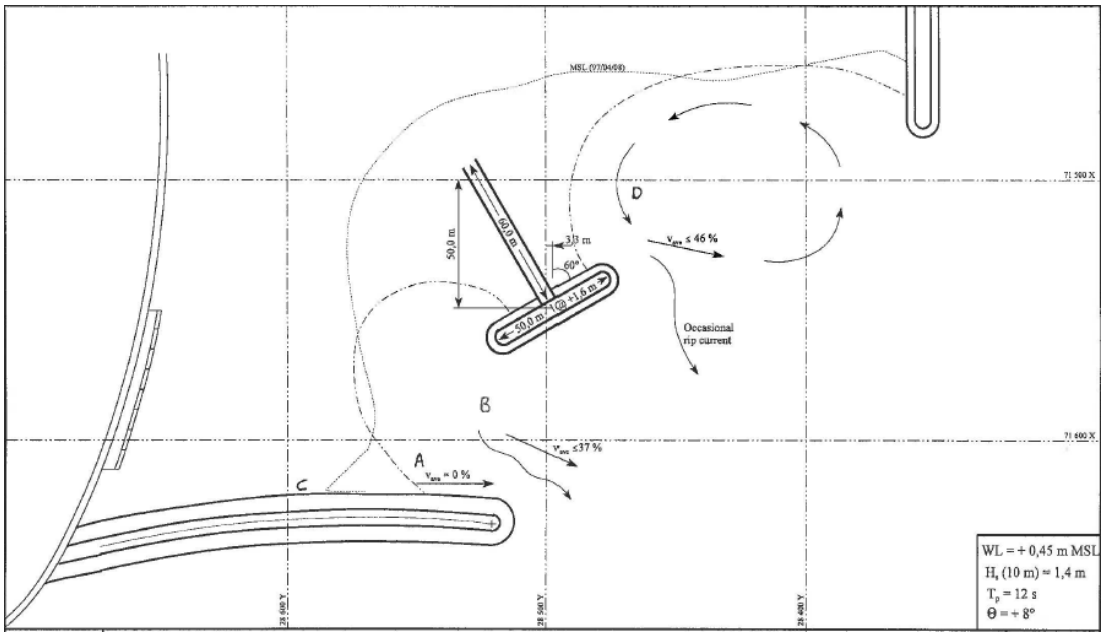

Figure 2-28: Example CSIR Proposed T-Groyne Solution (Theron et al., 1997)

2.4.2 Kistner (2016): Hydrodynamic Study of the Hazardous Cell Circulation and Potential Related Solutions to a Safer Bathing Facility.

Kistner looked at testing the same cases as tested by CSIR in 2016 with a two-dimensional Boussinesq numerical model. This model resolves wave-induced currents using of phase-averaged, depth-integrated formulations, which implies that the currents are limited to stable, time-averaged and depth-uniform flow on a 2D-horizontal grid. The model could then not account for any cyclic events which was noted in the physical model testing (Kistner, 2016).

Additionally, he noted another limitation to his study was that there was insufficient current data available for calibration; hence his results were provided as a change in magnitude from the original layout. He was able to replicate the observed cell circulation, shown in Figure 2-13 above on page 14, and then confirmed that the T-groyne tested by CSIR did in fact reduce the currents in the area overall but a similar hazard still persisted to the east side of the new T-groyne (Kistner, 2016).

Kistner used the 30 m peak average current velocity (U_{PA30}) to report his findings which he defined as the average velocity along a 30 m length, however a range of velocities would be measured over the model's domain as seen in Figure 2-29.

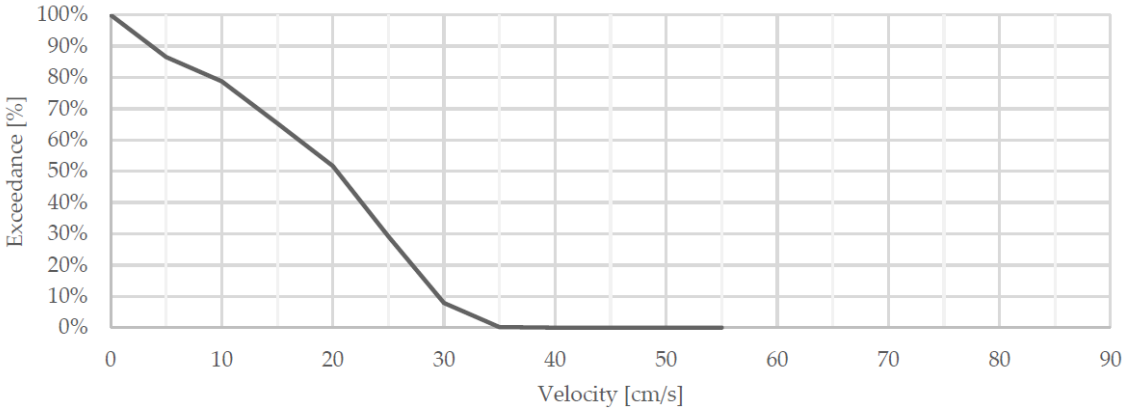

Figure 2-29: MB610 Velocity Exceedance Graph (Kistner, 2016)

A summary of the U_{PA30} calibration test results for the current groyne layout carried out by the CSIR and Kistner are provided in Table 2-2 below.

Table 2-2: Baseline Test Simulation Summary with U_{PA30} Results (Kistner, 2016)

Kistner	Hs (m)	Tp (s)	Dir (° N)	Tide (m)	Model Velocity Results [cm/s]			
					$U_{(H)}$	$U_{(I)}$	$U_{(J)}$	$U_{(K)}$
MB110	1.3	12	188	-0.3	17.8	21.2	45.9	18.6
MB210	1.1	12	188	-0.1	15.2	26	38.2	21.9
MB220	1.4	12	188	-0.1	21.1	31.5	43.6	24.7
MB310	1.3	12	188	0.3	18.7	31.4	35.7	30.1
MB410	1.1	12	188	0.4	16.3	26.5	27.6	29.3
MB420	1.4	12	188	0.4	22.1	30.9	37.3	32.2
MB430	1.1	8	188	0.4	25.3	28.8	36.7	29.1
MB510	1.4	12	188	0.45	24.4	30.2	35.7	31.3
MB610*	1.5	12	188	0.7	25.2	30.4	34.1	32.1
MB710	1.4	12	188	0.9	23.7	30	26.9	29.2
MB720	1.8	12	188	0.9	34.9	36.7	42	34.3

*CSIR baseline test

The locations of the reported results are marked in Figure 2-30 below which shows the plot of the results from test MB610 which also served as calibration for the CSIR model.

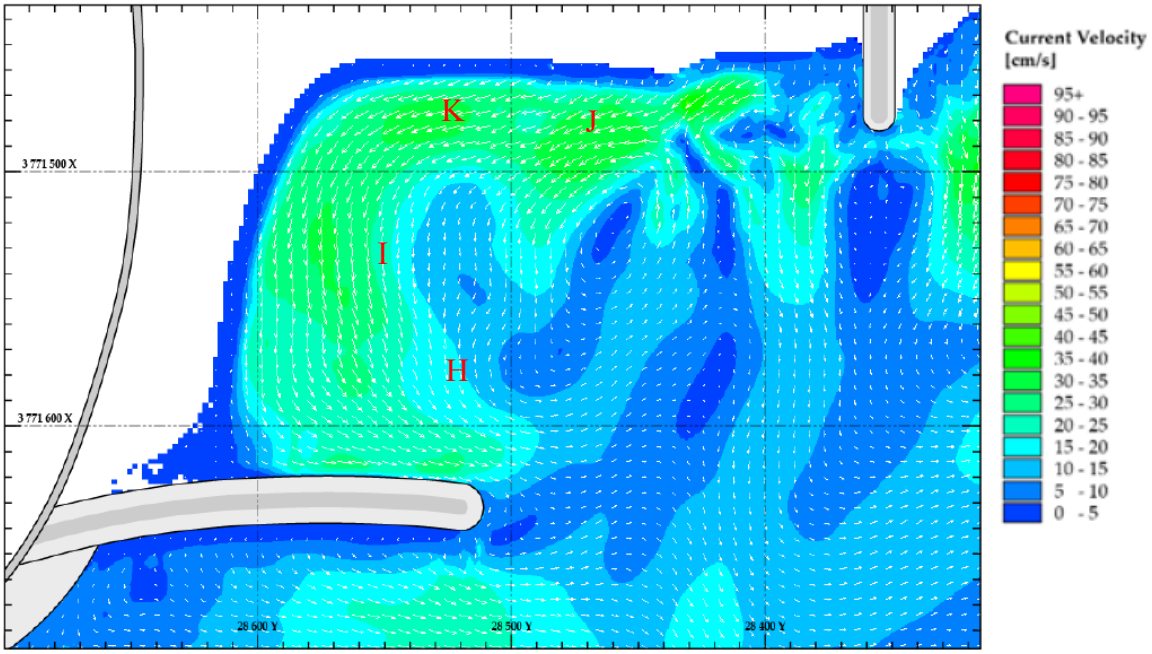

Figure 2-30: Results from Kistner Calibration Test MB610 (Kistner, 2016)

Kistner used a bathymetry for his calibration testing based on that used in the CSIR's 1997 model testing, as seen in Figure 2-31. This bathymetry is derived from a number of sources from survey data within the bay in 1997, offshore of the spur in 1994 as well as shoreline profiles from a CSIR topographic survey and Google Earth (Kistner, 2016)

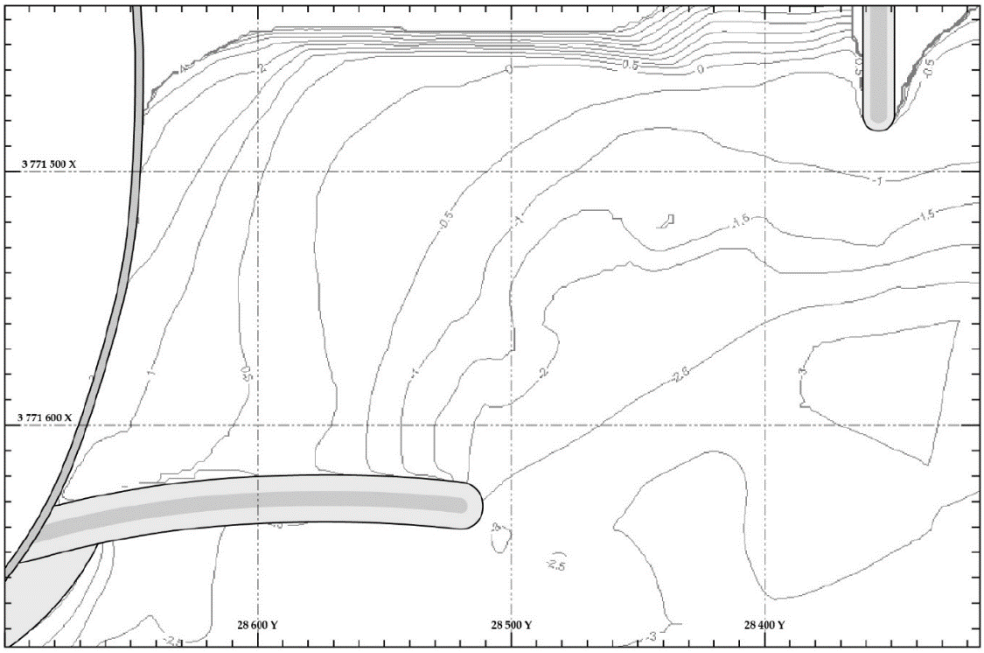

Figure 2-31: Bathymetry Profile Used in Kistner's Model Testing (Kistner, 2016)

2.5 Literature Study Conclusion

Aerial photography and platforms such as drones have been advancing in leaps and bounds since the 1800's with each advancement improving our view of the world and what we can learn from it. More recently this technology has become more accessible to everyone and widely used in industry to address a multitude of problems.

Images taken remotely from a consumer drone can be located spatially using GPS data, and can be processed to provide outputs which would have previously been limited to direct measurements such as ADCP's or GPS Drifters. These drone measurements could possibly provide a more accessible method for providing current data in the nearshore zone to help prevent dangers such as rip currents.

The intention of this thesis is to use consumer drones to build on these methods and provide in-situ current measurements to compare with those cases tested by the CSIR and Kistner for Monwabisi in the hope of providing a magnitude of the current. The methodology as to how to achieve this continues in Chapter 3.

Chapter 3: Methodology

3.1 Drifters

For the purpose of this study, citrus fruit was used as floating drifters due to their;

- near neutral buoyancy, allowing for a low profile in the water reducing the wind effects
- bright colour which stands out compared to the water colour in aerial photographs
- abundant availability at supermarkets which allow for many simultaneous deployments during testing
- biodegradability hence not requiring the drifter to be collected should it float out of the bay
- light weight providing ease of a person throwing them behind the surf zone from the beach

As the current velocity was assumed uniform through the water column, see Section 2.2.2 above, the movement of this drifter on the surface was assumed to be indicative of the currents below.

3.2 On-Site Measurements

For each on-site test the following procedure was followed:

1. The drone was flown up to an altitude of 30 m with the camera facing perpendicularly down and with the field of view just behind the breaking waves.
2. The camera was set to take a photo as often as possible, 2 seconds (s) in the case of the Mavic Air, and then left to hover in one place.
3. A set of drifters, normally 2 or 3, could then be deployed by standing at the bottom of the beach and then thrown out underneath the drone with some space between each to provide a spread of tracking points.
4. The video feed on the remote (if available) could then be monitored such that the drone was manoeuvred to keep the drifters as central in the frame as possible.
5. This was maintained until the battery low warning signal was given from the remote at which point the drone returned home (the initial take off point). The time span was typically 10 minutes for a Mavic Air.
6. The battery could then be replaced with a fully charged one and the test reset.
7. When possible, any drifters which returned to the beach could be retrieved and reused.

During the first few flights on-site, it was noted right away that the local kelp seagulls were quite interested in the drone, especially during take-off. The drone was hovered at 15 m above the take-off location for 30 seconds to a minute to allow for the bird's interest to be assessed, as well as for them to get used to the drone. This minimised the risk of one of the birds attacking the drone and causing it to crash into the water. Should a bird knock the drone at this time it should fall onto the beach relatively unscathed. Typically, after this time the birds have lost interest and flew away. Although, during one or two data collection flights the drone was brought back to the beach when birds were circling too close.

3.2.1 Dealing with Distortion

While it is common for lens distortion to introduce errors in measurements at the edges of an image, as seen at the edges of Figure 2-3 on page 6 above, no distortion correction has been explored as part of this study. Lens distortion is most often corrected with a calibrated lens profile, which at the time of this study was not available for the Mavic Air, and could possibly be determined in future studies. It was assumed that the effect of this distortion on the current measurements would be minimal as during testing the drifters were kept in the centre of the image frame where little to no distortion was present, as discussed in section 2.1.3. The distortion for current measurements should have less of an effect than for distance measurements; as it would most likely affect the coordinate readings at both time-steps by a similar magnitude and hence become negligible when used in calculating the velocity.

3.3 Simple Drone Testing

Initially tests were carried out using a very cheap DJI Phantom 2 with a GoPro mounted to the underside with a Gimbal. As this system was first released in 2013, it was rudimentary and did not have the capability for recording the GPS location with the recorded images (DJI, 2013). A test was carried out to determine if some current measurements could be taken with this platform, but it was soon apparent that a more capable drone would be required.

3.4 Intermediate Prosumer Drone Testing

3.4.1 DJI Mavic Air

The DJI Mavic Air is a prosumer class drone which is small, portable and retails for approximately 20 000 ZAR. With that in mind it is still a capable platform with a 12 mega pixel camera and a dual-GNSS positioning system as seen in Table 2-1 on page 5 above. While it can't operate in wind conditions as high as the more professional drones it is also able to view the camera through the remote control while recording the GPS and Altitude data in the metadata of any image taken.

3.4.1.1 Camera Calibration

The drone was taken into a car park and flown over a measuring tape on the ground in order to take a set of images of the tape and calculate its length using the proposed method (see Figure 3-1). The calculated length could then be compared to the known tape length to provide a scaling factor for the images from the camera. If the measured length was shorter than that of the tape, the scaling factor would be more than 1 and the images size would need to increase, and vice versa. The scaling factor of the image is related to the actual field of view, to the camera's properties and the height of the drone above ground, elaborated on in section 3.5.1.3 below. The values for the DJI Mavic Air recommended on the manufacturer website, was tested to get a set of calculated measurements which were compared with the known length to check for accuracy. If an error was found the camera properties could be adjusted to align the calculations with the measurements.

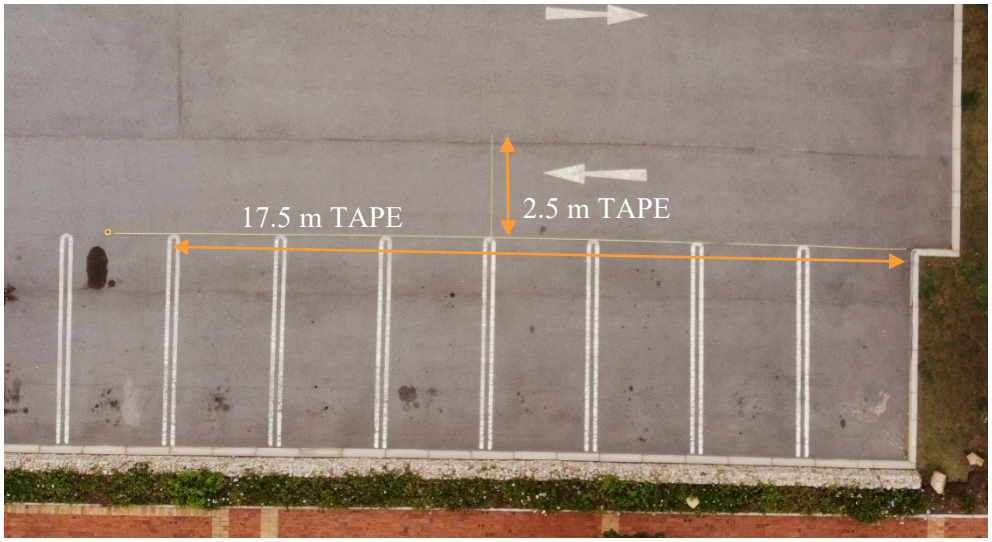

Figure 3-1: Car-Park Calibration Setup

During later tests at Monwabisi, a tape was laid out near the water line to get a second calibration test prior to measuring drifters. In addition to the camera properties, an "elevation correction" would be assessed as the drone's altitude was measured relative to the take-off location, which on the beach was from a hand-held position behind the highest wave run-up. An initial value of 1.6 was used which was made up of 1.2 m from beach level to the average hand-held height, plus an additional 0.4 m from the assumed current tide mean water level to the elevation of the beach where the drone was launched (see Figure 3-2).

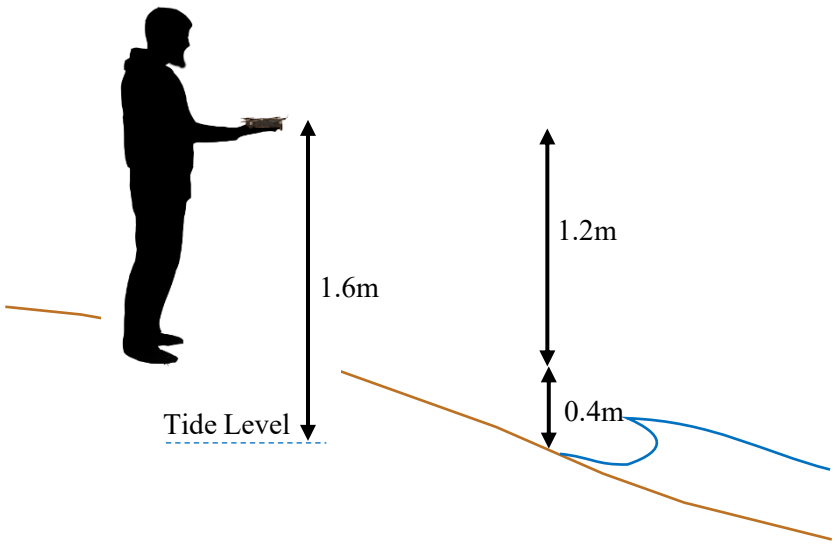

Figure 3-2: Elevation Correction Component Makeup

3.4.1.2 Error Testing

An initial simple GPS error check was carried out where a fixed ground point was used to provide a reference point to determine the error generated by GPS drift as well as any movement of the aircraft due to wind. A stationary point was used, and several aerial images were collected such that the theoretical coordinates could be calculated, as per Section 3.5.1 below, and these were compared to

each other to determine the difference. Data collection was carried out at different heights as well as while the drone was in motion to determine if there was any influence of these factors on the location error.

Additionally, the final site test included a long stake which was driven into the sand just behind the breakers (see Figure 3-3 & Figure 3-4 below) to provide a GCP which could be used to compare the generated error to a set of drifter velocity measurements directly.

Figure 3-3: Monwabisi GCP Test Setup

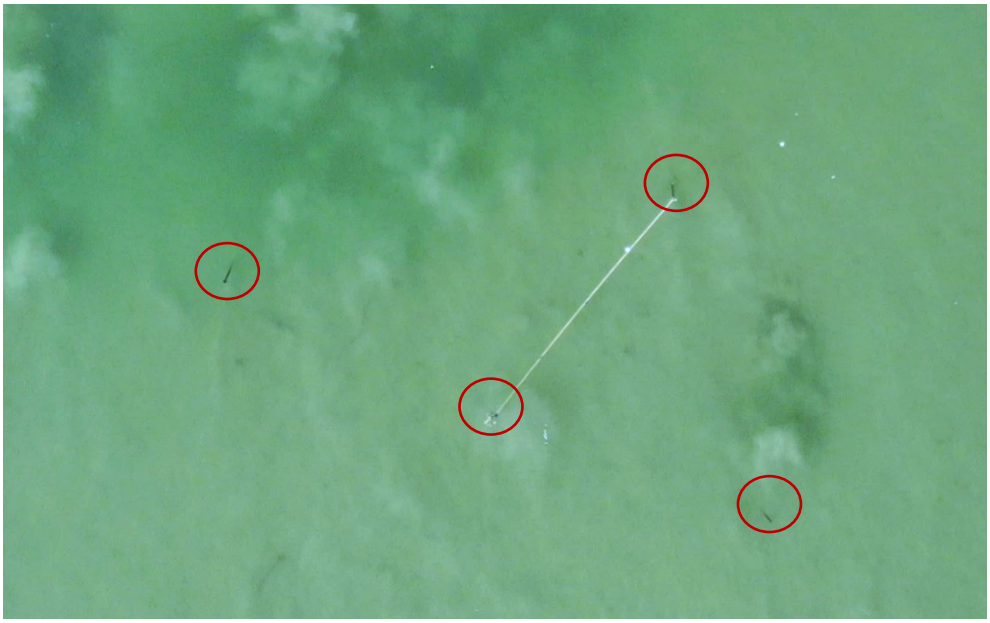

Figure 3-4: Aerial View of Monwabisi GCP Test Setup

3.4.2 DJI Inspire 2

To provide a comparison with a more advanced drone model, the DJI Inspire 2 provided by the Stellenbosch University Civil Department was included in the study. Being a much larger drone with increased flight time and a better camera, it comes with a much higher price tag at around three times that of the Mavic Air. No calibration or error testing was carried out for this drone as the time on site was limited to one data collection trip due to logistics.

3.5 Extracting Data from Photographs

3.5.1 Reference Coordinate System Conversion

3.5.1.1 Extracting data from each set of images

Each image captured by a digital camera included additional information, called tags, in the file such as camera make/model, lens details, date at which the photo was taken and GPS location (if available). This metadata is called the exchange image file format (EXIF) data (CIPA & JEITA, 2016). In the case of a DJI drone this EXIF data included the tags listed in Table 3-1 below.

Table 3-1: Summary of EXIF Tags Used in this Study

EXIF Tag	MavicAir Output	Description	Use
FileName	DJI 1414.JPG	Name of the image from the drone.	Reference
Make	DJI	Make of the drone.	Info
Model	FC2103	Model of the drone corresponding to the Mavic Air.	Info
DateTimeOriginal	2018:12:11 07:45:38	Date and time at which the image was taken.	Reference
ApertureValue	2.8	Fixed amount of light let into the camera.	Scaling
FocalLength	4.5 mm	Fixed lens focal length which.	Scaling
ExifImageWidth	4056	Number of pixels on the sensor horizontally.	Scaling
ExifImageHeight	3040	Number of pixels on the sensor vertically.	Scaling
FocalLengthIn-35mmFormat	24 mm	Photographic standard metric for lens focal distance.	Scaling
GPSLatitude	34° 4' 22.29" S	GPS output for latitude in degrees, minutes and seconds.	Omitted*
GPSLongitude	18° 41' 32.62" E	GPS output for latitude in degrees, minutes and seconds.	Omitted*
Latitude	-34.0728700	Decimal degree latitude reference, -'ve for south.	Geolocating
Longitude	18.6924006	Decimal degree longitude reference, +'ve for east.	Geolocating
AbsoluteAltitude	1.2	Absolute altitude of take-off location above sea level.	Omitted**
RelativeAltitude	29.2	Relative altitude of drone when photo was taken.	Scaling

EXIF Tag	MavicAir Output	Description	Use
GimbalYawDegree	-13.9	Orientation of camera in relation to magnetic north.	Geolocating
GimbalPitchDegree	-89.9	The vertical angle of the camera in relation to the horizon.	Check
FlightRollDegree	-7.3	Orientation of the drone to the right or left.	Check
FlightYawDegree	-13.1	Orientation of the drone in relation to magnetic north.	Check
FlightPitchDegree	-12.7	Orientation of the drone to the forward or back.	Check
ScaleFactor35efl	5.3	Hypothetical scale factor of actual focal length to 35mm equivalent focal length.	Check
FOV	73.7°	Angle of image width field of view.	Scaling

** The official GPS Latitude and Longitude provided by DJI was rounded to two decimal seconds which was found to have an insufficient accuracy and hence omitted. See Section 4.1.1.*

*** The Absolute Altitude for the Mavic Air was found to be fixed at 1.2 and hence of no use. However, the Inspire 2 did provide results for review.*

Table 3-1 does not include all the EXIF data tags available in the image file; however, these were the tags relevant to this study. These were extracted from each image using a freeware application called ExifTool version 10.08 by Phil Harvey (2018). ExifTool is a command line application which can read and write EXIF tags on an image file with functionality which allowed for the tags from an entire folder of images to be read and then written into a .csv file. The command prompt code used was as follows:

```
exiftool -a -csv 2019-02-07_Inspire_Comparison > 2019-02-07_ExifData.csv
```

This calls the ExifTool application, then reads all tags (term: -a) in files from the folder "2019-02-07_Inspire_Comparison" and wrote them to a .csv called "2019-02-07_ExifData". The columns corresponding to the tags shown in Table 3-1 were then extracted into an Excel spreadsheet for further processing.

3.5.1.2 Coordinate Transformation

Excel was used to convert the geographical latitude/longitude coordinates written in the image file to gauss conform (x : y) and then UTM (Y : X) coordinates. This was done as the UTM coordinates are measured in metres (m); hence displacement and velocity calculations could be carried out with ease. The transformation was set out based on Parker (2011). The transformation equations provided in the article have been adapted for Monwabisi to suit the World Geodetic System (WGS) 1984 ellipsoid with the central meridian 19 East, see Appendix: C, which could be simplified as follows:

$$x = B_\Phi + \frac{\ell^2}{2}.N.\sin\Phi.\cos\Phi + \frac{\ell^4}{24}.N.\sin\Phi.\cos\Phi^3.(5 + 9\eta^2 + 4\eta^4 - \tau^2) + \frac{\ell^6}{720}.N.\sin\Phi.\cos\Phi^5.(61 - 58\tau^2 + \tau^4 + 270\eta^2 - 330\eta^2.\tau^2) \quad (3\text{-}1)$$

$$y = \ell.N.\cos\Phi + \frac{\ell^3}{6}.N.\cos\Phi^3.(1 + \eta^2 - \tau^2) + \frac{\ell^5}{120}.N.\cos\Phi^5.(5 - 18\tau^2 + \tau^4 + 14\eta^2 - 58\eta^2.\tau^2) \quad (3\text{-}2)$$

Where:

Φ	= Absolute value of Latitude	(radians)
λ	= Absolute value of Longitude	(radians)
Η, τ, B_Φ, N	= Input equations provided in Appendix: C	

The convention for the South African Gauss Conformal Projection has the x coordinate (3-1) running positive towards the south and the y coordinate (3-2) running positive towards west. These need to be converted further in order to work with AutoCAD which uses Universal Transverse Mercator (UTM) convention which has Northings, Y values increasing north, and Eastings, X values increasing east. Hence in AutoCAD the coordinates (Y=-x , X=-y) as per Figure 3-5 below and this study used the UTM convention for all calculations *(Parker, 2011)*.

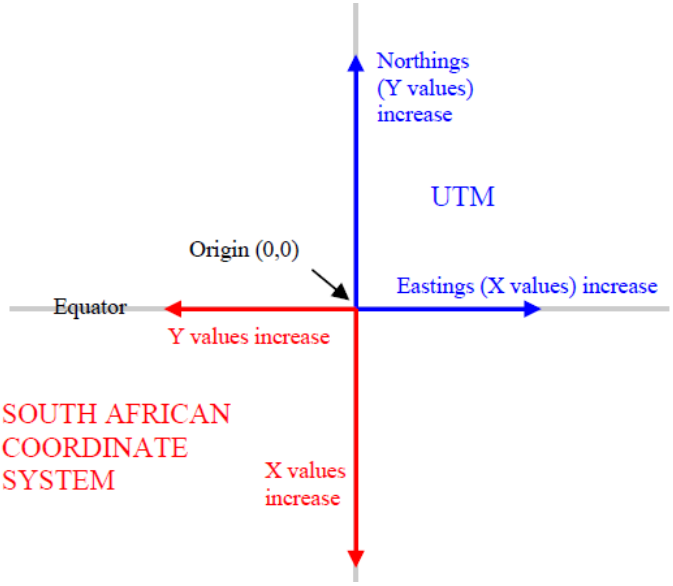

Figure 3-5: Gauss Conform & UTM Conventions (Parker, 2011)

3.5.1.3 Scaling the Images

In order to determine the coordinate for the drifter in relation to the drone's GPS, the image required scaling based on the height above ground. This scaling was based on the camera's focal length as

well as the image sensor size. This relationship can be seen in Figure 3-6 below which illustrates the ratio:

$$\frac{S_W}{f} = \frac{FOV_w}{h} \qquad (3\text{-}3)$$

Where

S_w = Sensor Width (mm)

f = Focal Length (mm)

FOV_w = Field of View width (m)

h = Altitude/Distance to subject (m)

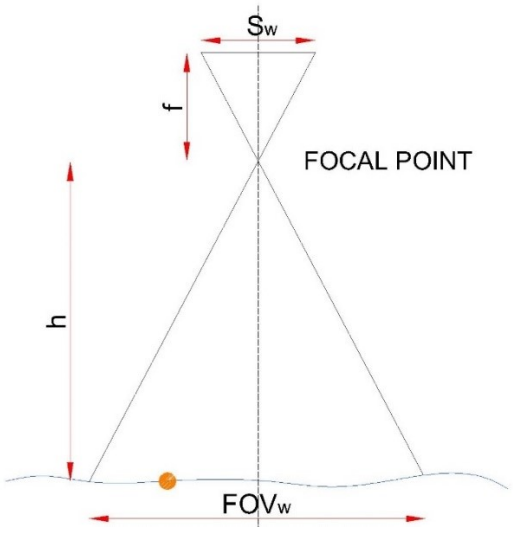

Figure 3-6: Image Scale Ratio

The Mavic Air and the Inspire 2's Zenmuse X4S cameras are reported to have specifications as indicated in Table 3-2.

Table 3-2: Sensor Properties (D'Agostino, 2018)

Description	MavicAir	Inspire2's Zenmuse X4S camera
Sensor Size	1/2.3"	1"
Maximum Resolution (pixels)	3840 x 2160 (12 MP)	4096 x 2160 (20 MP)
S_w Sensor Width (mm)	6.17	12.8
S_h Sensor Height (mm)	3.47	7.2

Assuming an average flight height of 30 m and f = 4.5 mm as per Table 3-1 above, the FOVw of the image would be 41.1m.

3.5.1.4 Reference Output

The image name, the coordinates, the Gimbal Yaw Degree and the FOVw was then exported from EXCEL to a .csv file in a list which could be read into AutoCAD.

3.5.2 Processing the Images

All readily available software packages for processing aerial photography that were found as part of this study, focused on stitching all images together to form a 3D model and a map. While the functionality of packages such as Agisoft© Metashape could easily orientate each image in coordinate space, the ability to locate, track and then export the coordinates of the drifters along each time-step was limited; hence, the decision was made to import each image into AutoCAD which allowed for Visual Basic for Applications (VBA) Macro's to be developed to build-in the required functionality.

3.5.2.1 Importing Photo Series into AutoCAD

The VBA macro is provided in Appendix: D but the code executes as follows:

Firstly, the code needed to be modified to define the fileDirectory variable in which the images were stored as well as the file path of the .csv file which contains the image data list, as seen in Figure 3-7.

```
Function DefineDirectory()
    fileDirectory = "C:\Users\Ryan\Documents\Thesis Working\2019-04-11_LastTest" & "\"  ' File directory path
    imageList = "2019-04-11_LastTest_CalculationsF4.18+1.6m(1).csv" ' Image list .csv filename"
End Function
```

Figure 3-7: VBA Code for File Path Definition

The AttachMultipleImages() function could then be called which initialises the files by reading the .csv file into memory, then looping through each image in the list and carrying out the following steps:

1. The image was inserted at the coordinates (FOVw/2 , FOVh/2), the top left as seen in Figure 3-8 below, which was the convention used by AutoCAD.
2. The scale factor was applied from the top left corner such that the width of the image was now equal to the FOVw which also brought the centre of the image to the coordinate (0,0) or the origin.
3. The imageVisibility AutoCAD attribute was turned off to prevent the computer being overwhelmed with a large amount of data, affecting performance.
4. The image was rotated by the GimbalYawDegree.
5. Finally, the image was moved from the origin to the coordinates at which the image was taken.

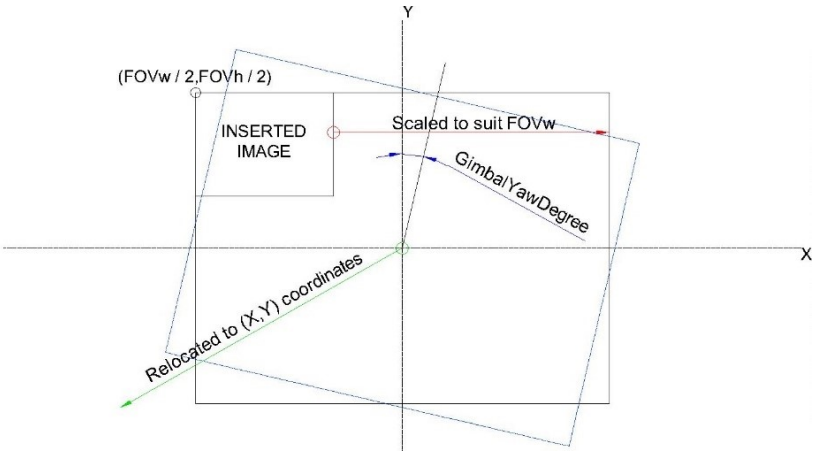

Figure 3-8: AutoCAD Image Insertion

As part of the initialisation process an index of image names needed to be stored in AutoCAD's memory which was carried out by the ReadNames() function. Like the function above, it worked through the list of images and read each name into memory. The total number of images was also recorded. Once the entire list has been worked through the first image in the list was made visible.

3.5.2.2 Moving Through Images

Two functions NextImage() and PreviousImage() allow for images to be sequentially worked through. This was achieved by turning the visibility of the current image off and then turning on the Next/Previous image. If the end of the list of images was reached then the first image was turned on, and vice versa if working backwards.

3.5.2.3 Marking Drifter Locations

Starting at the first image each time-step was worked through until a drifter had entered in the frame. A point node was placed at each drifter location using a custom VBA function which pulls up the image and then inserted a point, as seen in Figure 3-9 below, and any features of interest were recorded in the calculation Excel sheet, such as a passing wave which may have led to surfing effects. This process was repeated until the drifter was lost or the drone has finished the flight. These points also provided an indication of the surface current pattern. Before moving onto the next flight/drifter deployment, the colour attribute in AutoCAD for the set of points corresponding to the previous drifter were all set to a unique colour for identification.

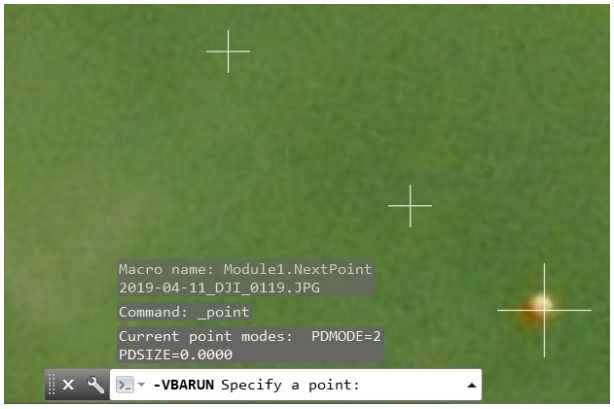

Figure 3-9: Marking Drifter Locations in AutoCAD

3.5.2.4 Exporting Drifter Coordinates

Another VBA function was created to run through the entire drawing and export the coordinates of each point as well as the corresponding unique colour id, which was a number between 0 and 255, to a *.csv file, as see in Figure 3-10. This function also allowed for the coordinates of a polyline or single line to be exported if any reference lengths had been placed for calibration as described in Section 3.4.1.1 above.

```
Handle,Length,StartX,StartY,EndX,EndY,Colour
836,,-28630.4734636741,-3771842.96879783,,,10
837,,-28631.927815918,-3771840.94626448,,,10
838,,-28632.4210307179,-3771840.20045564,,,10
839,,-28631.8139967567,-3771840.75665215,,,10
83A,,-28631.2954887005,-3771840.78193383,,,10
```

Figure 3-10: AutoCAD Drifter Coordinate Output

3.5.3 Analysing Currents from Coordinates

Once back in the Excel calculation file the current velocity of the drifter at each time-step could be calculated using the following equation:

$$u_i = \sqrt{\frac{(X_{i+1} - X_i)^2 + (Y_{i+1} - Y_i)^2}{|T_{i+1} - T_i|.(24.3600)}} \qquad (3\text{-}4)$$

Where:

u_i	= Overall current velocity at time-step i	(m/s)
X_{i+1} & X_i	= X coordinate of drifter at time-step i and i+1	(m)
Y_{i+1} & Y_i	= Y coordinate of drifter at time-step i and i+1	(m)
T_{i+1} & T_i	= Timestamp of image at time-step i and i+1	(decimal days)

The noisy data included any orbital motions and surfing effects of passing waves, along with any errors generated by the drone's GPS. If any notable events were to be excluded this could be done at this stage and then the data could be averaged out over several time-steps. Tests were carried out to adjust this period and optimise accordingly to smooth out the orbital motions as well as to reduce the GPS error.

Assuming that the GPS error was scattered in all directions, one way of reducing the velocity error generated was to average out a number of coordinate readings to provide an average coordinate which could then be used to calculate the velocity. This essentially applied an averaging filter to the data set, smoothing out the results where the frequency in Hz was 1 divided by the period over which the averaging took place, in seconds.

The following example equation was used to calculate the velocity of the points every 6 seconds, as each time-step equated to 2 seconds when each photo was taken:

$$U_{t=2} = \frac{\sqrt{(\sum_{t=4}^{6} Xt - \sum_{t=1}^{3} Xt)^2 + (\sum_{t=4}^{6} Yt - \sum_{t=1}^{3} Yt)^2 . 100}}{|T_{t=5} - T_{t=2}| . 24.3600} \quad (3\text{-}5)$$

Where

$U_{t=2}$	= Velocity at time-step 2	($cm.s^{-1}$)
$\sum_{t=1}^{3} Xt$	= Average X coordinate over time-steps 1 through 3	(m)
	(Similar notation for other X and Y coordinates)	
$T_{t=5}$	= Exif time tag at time-step 5 (or 2)	(day)

This equation averaged out the three coordinates around time-step 2 and 5, then provided the average velocity between these time-steps over 6 seconds. The next velocity was then calculated between time-step 5 and 8, then 8 and 10 and so on.

A similar filtering method has been used on drifter data results in previous studies to average out short wave motions and noise. Olsson (2004) used a 0.1 Hz filter, Mccarroll *et al.* (2014) used a 0.4 Hz filter while Gallop *et al.* (2018) used a 0.05 Hz filter. This equated to an averaging period of 10 , 25 and 20 seconds respectively and a similar range of averaging periods was used when averaging out the drifter data. Similar to these studies, the data was then grouped into 5 m by 5 m grids to resolve the current velocity spatially to provide adequate resolution over the study area while also providing enough data to characterise each cell.

The current's components in the X and Y direction was calculated, in such a way that once grouped, the overall current direction at each grid cell could be displayed using the MATLAB quiver function. This was calculated using the following equations which were also averaged as per equation (3-5):

$$u_{xi} = \sqrt{\frac{(X_{i+1} - X_i)^2}{|T_{i+1} - T_i| . (24.3600)}} \;\&\; u_{yi} = \sqrt{\frac{(Y_{i+1} - Y_i)^2}{|T_{i+1} - T_i| . (24.3600)}} \quad (3\text{-}6)$$

Where:

u_{xi}	= Current velocity in the x direction at time-step i	(m/s)
u_{yi}	= Current velocity in the y direction at time-step i	(m/s)

3.6 Environmental Data

WindGuru© and Windy (weather forecasting websites focussing on wind and waves) were followed in the week prior to each data collection excursion in order to plan for the best conditions for flying the drone as well as attempting to vary the metocean conditions.

A few hours after the data had been collected, a set of wind and wave estimates for Monwabisi, as well as Muizenberg and Strand were recorded from WindGuru©, Windy and windreport.co.za assuming that the sites had been updated with the actual readings, examples of which can be found in Figure 3-11 and Figure 3-12 below.

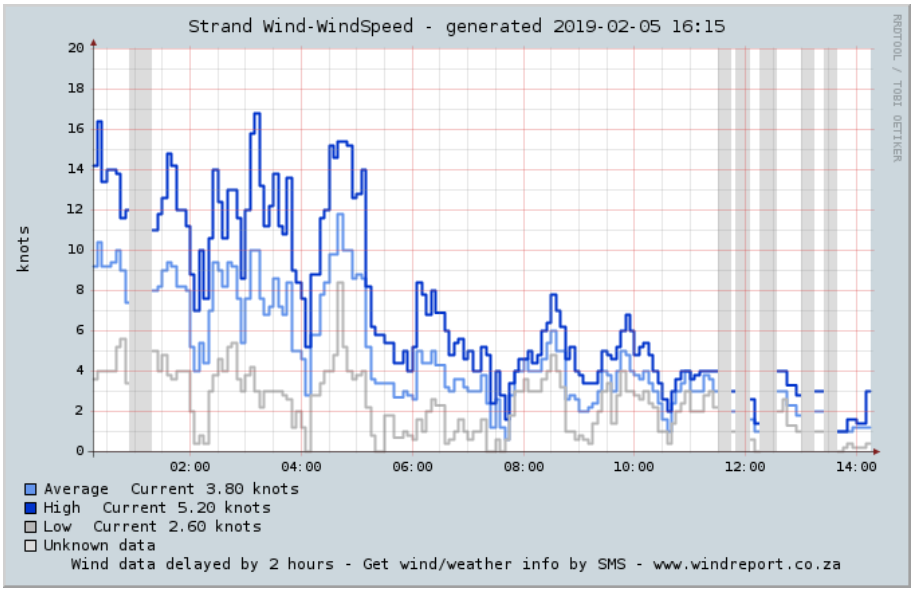

Figure 3-11: Windreport.co.za Example Wind Data for Strand

Note: "Current" in Figure 3-11 refers to the Average, High and Low at the time: 2019-02-05 16:15

Init: 05.02.2019 06 UTC	Tu 05. 08h	Tu 05. 11h	Tu 05. 14h	Tu 05. 17h	Tu 05. 20h	We 06. 05h	We 06. 08h	We 06. 11h	We 06. 14h	We 06. 17h	We 06. 20h
Wind speed (km/h)	6	11	18	19	17	14	16	17	20	22	18
Wind gusts (km/h)	8	11	18	24	26	19	22	21	23	27	26
Wind direction	↖	↑	↑	↑	↖	↖	↖	↖	↑	↑	↖
Wave (m)	1.5	1.5	1.5	1.5	1.4	1.7	1.9	2	2.2	2.4	2.6
Wave period (s)	12	12	12	12	11	11	10	10	9	9	9
Wave direction	↗	↗	↗	↗	↗	↗	↑	↑	↑	↑	↑
*Temperature (°C)	22	27	28	26	21	19	22	28	31	31	26

Figure 3-12: Example Data for Macassar (near Monwabisi) (WindGuru, 2019)

The South African Weather Service (SAWS) was also contacted at the end of all data collection sessions to provide actual wind data recordings from the Strand and Cape Town International Airport weather stations. PRDW Port and Coastal Engineer's also provided extracts for Monwabisi from a Boussinesq wave numerical model, which was set up for False Bay to provide wave results from NCEP hindcast data. A combination of these was used to compare conditions between each of the data sets and those tested previously.

3.7 Comparison with Previous Studies

The 1997 CSIR report did not provide any current magnitudes in the model results; hence, it was not possible to make a direct comparison between the results and the drifter velocities measured in this study. Therefore, the comparison focused on Kistner's results which provide current magnitudes while also correlating with the current patterns found in the CSIR's calibration tests. In order to provide a comparison to Kistner's 30 m peak average velocity (U_{PA30}) results, a lookup table was used to average out the entire set of velocity results over a 25m by 25m grid. This provided a balance between an average 30 m path length through the domain, as seen in Figure 3-13, as well as for ease of data processing in Excel. This provided an approximation of the U_{PA30} distributed over the domain of the drifters.

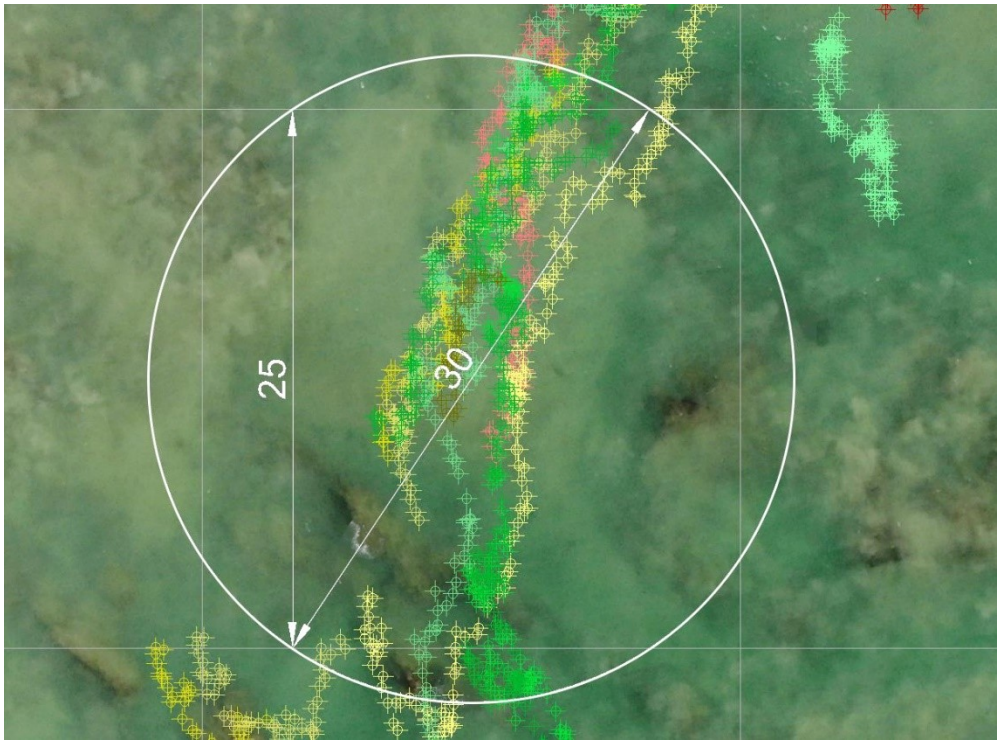

Figure 3-13: 30m Current Averaging Domain Sketch

Chapter 4: Results

4.1 Drone Output Review

It was noted early in the review of the collected images that the results would rely on the ability of the drone to provide accurate positioning data. Initially with the original Phantom 3 drone it was found to be extremely difficult to orientate the images with no recorded drone location data and no reliable GCP's, as the water surface below was always moving and evolving such that photogrammetry could not align the images post collection. Therefore, the study hinged changing to the more advanced MavicAir drone which did record the drone's GPS and altitude reading in the images EXIF tags. The results from the tests described in section 3.4 are as follows:

4.1.1 Scaling

In order to get the correct scaling factor, a tape was used as a reference measure as described in section 3.4.1.1. The following section describes the calibration results carried out at a controlled car-park as well as on site at Monwabisi Beach.

4.1.1.1 Car-Park Calibration

Initial calibration tests included setting a tape measure out on a car-park. This gave a mean drone measurement of 2.29 m which was approximately 90 % of the actual length measured which was 2.5 m (see Figure 4-1). This was due to an incorrect FOW scaling factor of the $\frac{Sw}{f}$ term from equation (3-3). While the S_w was constant at 6.17 mm the actual f may differ from that reported on the EXIF file. DJI also provided the angle of view (AOV) for the Mavic Air as 85° diagonally (DJI, 2019a) and this was proportional to the FOV divided by the height. Because of this, the following relationship could be used:

$$\tan\frac{AOV_d}{2} = \frac{FOV_d}{2}.\frac{1}{h} \qquad (4\text{-}1)$$

Equation (4-1) could be rearranged and substituted into equation (3-3) in the diagonal form to provide the following equation for f:

$$f = \sqrt{{S_w}^2 + {S_h}^2}.0.5\cot\frac{AOV_d}{2} \qquad (4\text{-}2)$$

If the values from Table 3-2 on page 35 and the angle above were substituted into (4-2), the calculated focal length for the camera equals 4.18 mm which was less than the 4.5 mm reported by DJI. This reduction of the focal length led to a 7.6 % increase in the scale factor which would increase the measured length of the tape to 2.46 m, which was approximately 98 % of the actual measurement.

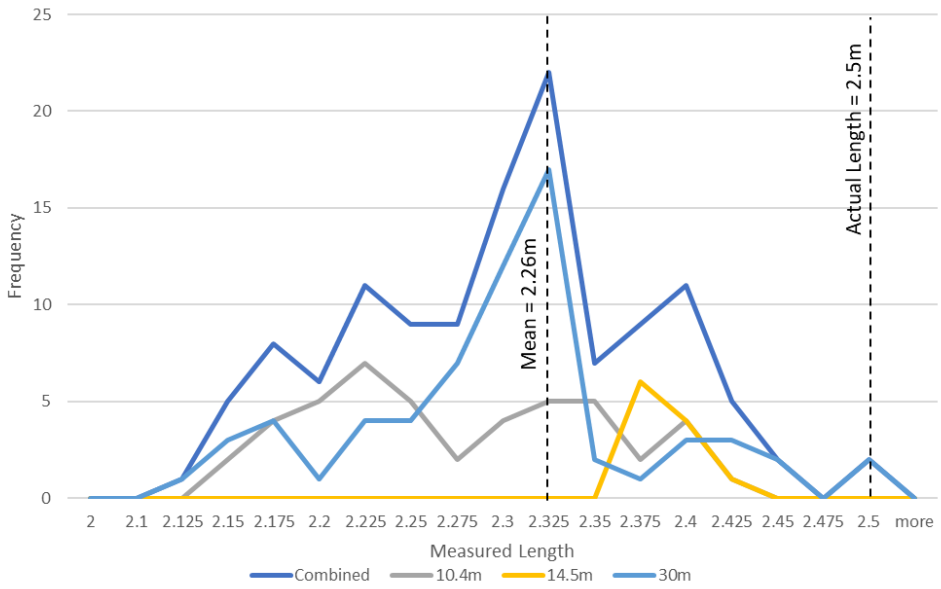

Figure 4-1: Initial Calibration Test Length Distribution Results Taken at Drone Altitudes of 10.5, 14.5 and 30m Above Ground

Figure 4-1 also highlighted that at lower altitudes, such as the set of readings at 10.4 m altitude, the effect of the barometer sensitivity being 0.1 m was more prominent and hence the results were more spread out. At higher altitudes the tape was less clear as the image was more enlarged, and some variation was introduced when selecting the start and end points. Therefore, there was a trade-off between flight height and visibility of the point of interest.

It should also be noted that the results above exclude measurements taken as the drone was moving between these altitudes as these generated outlying errors with readings as low as 1.65 m. It was assumed that as the drone altitude changed drastically, the absolute altitude tag stored in the image file was for slightly before/after the photo was taken. A similar effect was noted for the coordinates which will be elaborated on in section 4.1.2.

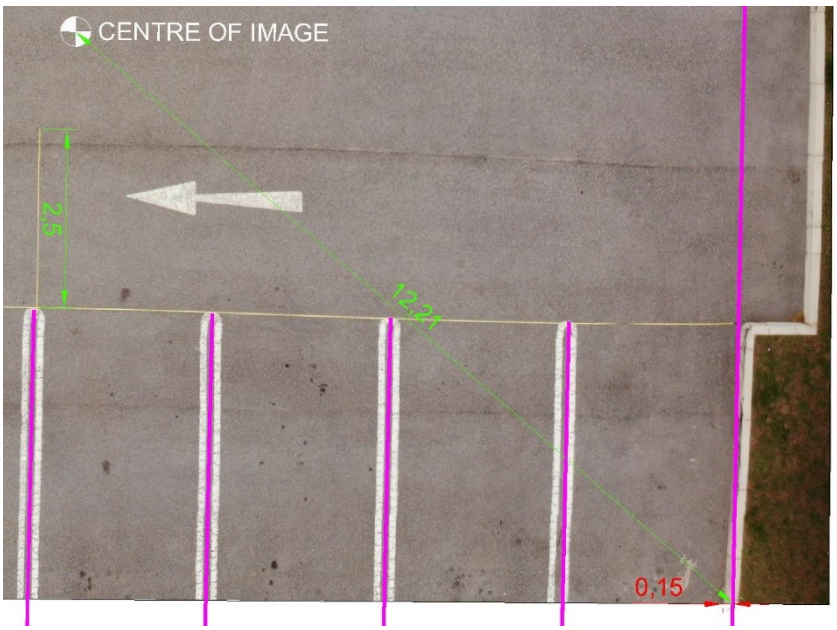

Figure 4-2: Bottom Right Quadrant of Image Showing Car-Park Edge Distortion

The images from the car-park calibration tests were also used to assess the effect of the lens edge distortion, as discussed in section 3.2.1. Although some distortion was noted, it only became noticeable at the edge of the image. This is shown in Figure 4-2 where only the last bay markings became distorted. The kerb was ±15 cm out of alignment, which when considering that this point was ±1221 cm from the centre of the image, equated to an error of 1% in distance. As noted in section 3.2.1 this should not affect the current measurements as both coordinates experienced similar distortions if measured at the corner of the image, while the drifters were kept in the centre of the frame, where possible.

4.1.1.2 On Site Calibration

Results from the calibration testing at Monwabisi showed a high variability in the measurements for length over three different flights. Figure 4-3 below illustrates the histogram for the three sets of results showing that the mean value varied from 2.57 m to 2.83 m. This could be due to the elevation correction value which was set at 1.6 m when processing all three sets of results below. The on-board barometer reference altitude on the drone could have drifted over the tests with atmospheric changes, and this coupled with launching the drone from different arm heights/beach elevations could lead to some variability in the altitude between flights. Therefore, an elevation correction may be required for each flight with the 3rd flight requiring a much lower value to bring the mean in line with the expected measurement of 2.5 m. This would also be expected as the take-off location was approximately 7m down the beach. Again, measurements were excluded if the drone was gaining/losing altitude and the results below were taken while the drone was hovering around 15.1 m, 15.6 m and 29.9 m. The results near an altitude of 30 m are highlighted in the figure as that was the altitude at which the drifter testing was due to take place.

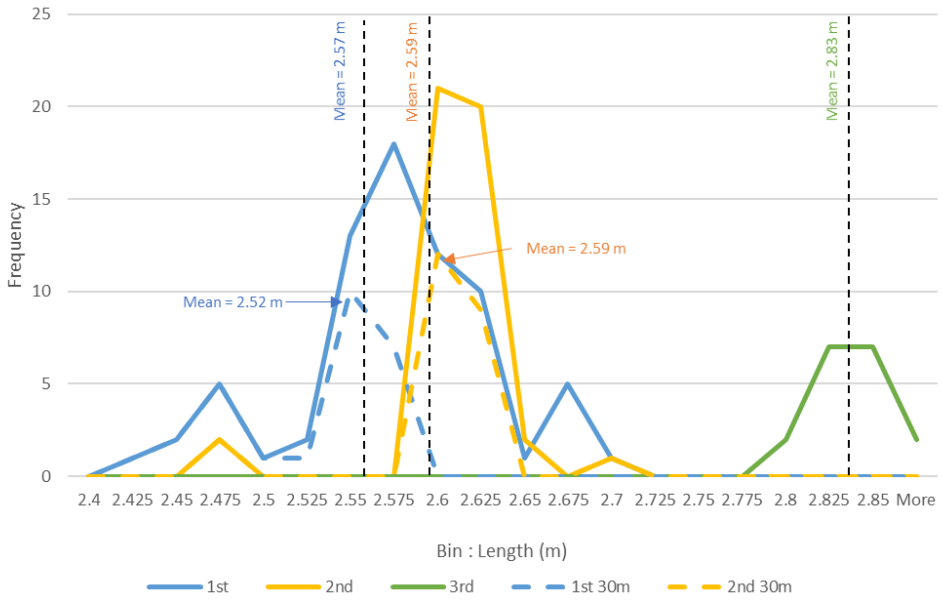

Figure 4-3: Calibration Results of Three Flights at Monwabisi

Only the first flights measurements were used to compare the two proposed focal length values to eliminate the effect of the elevation correction, as indicated in Figure 4-4 below. These tests also

confirm those of the car-park in that the f value of 4.18 mm was more likely the focal length of the Mavic Air's camera. With an f of 4.5 m the mean measurement was 2.33 m, while at an f value of 4.18 mm the mean measurement was 2.52 m.

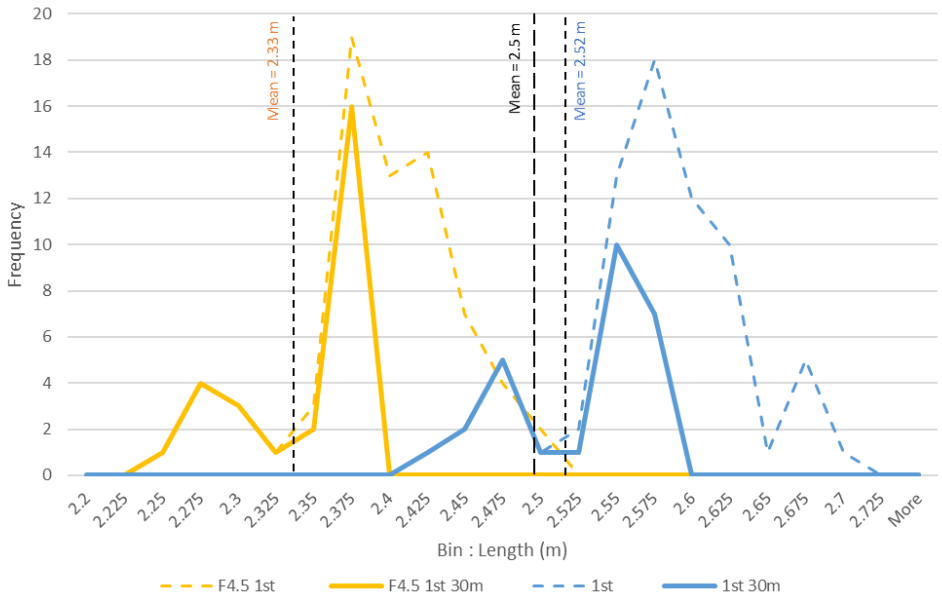

Figure 4-4: On-Site Calibration 1st Flight Results Comparing f = 4.18 mm & 4.5 mm

This figure also highlighted that the additional variability of measurements at lower elevations have a larger range which implied that the height used in the calculations has a notable influence on the results. As the drone hovering accuracy was a constant, the recorded height of the drone, as seen in Figure 4-5 below, had a larger percentage of the overall height measurement due to the hovering error than compared to higher altitudes where this error was small compared to the overall height.

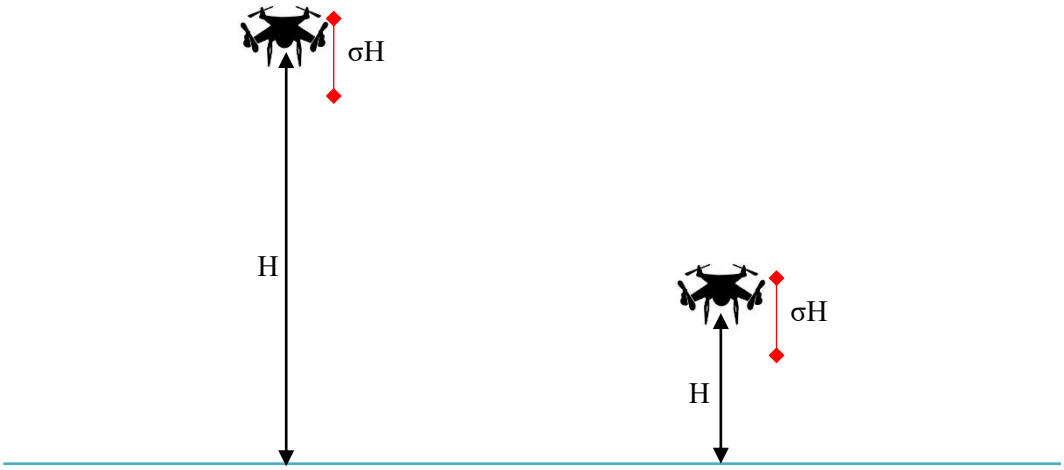

Figure 4-5: Drone Altitude Error Effect

Typical drone applications, such as photogrammetry, circumvent this problem by requiring an overlap between adjacent images, as described in section 2.1.3. In this application however, the continually moving sea surface would not facilitate correlating two temporally spaced images; hence, the drone's internal altitude determination was relied on in this study. This could be addressed by

drones such as the Phantom RTK which utilises superior positioning technology, or by implementing a specialised stereoscopic camera, also described in section 2.1.3, which would record at least two images simultaneously, allowing for of the distance from the drone to the water's surface to be calculated at each time-step, along with the distance to the drifters below.

4.1.2 Coordinates

4.1.2.1 On Beach Testing

The site measurements provided not only the lengths for calibration, but the coordinates from one side of the tape could be used to assess the measurement error. Figure 4-6 shows the set of measurements taken for the three flights at Monwabisi. The centre of all the coordinates can be seen in the centre of the image, and 95% off all coordinates were within 1.75 m of this point. A subset of coordinates was selected based on the horizontal velocity of the drone, which was limited to 20 cm.s^{-1}. This cleaned subset provided a second point which appeared to be more centred over the expected coordinates. The radius in which 95 % of this subset falls, was also reduced to 1.14 m.

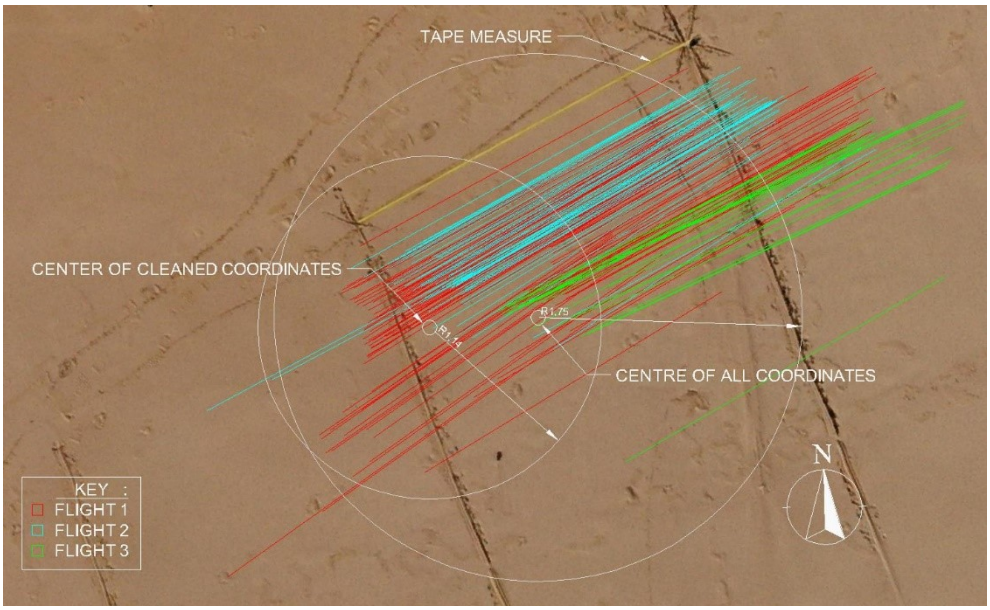

Figure 4-6: On-Site Measurements

The overall spread may be quite large, but the distance from one coordinate measurement to the next was not as drastic, with an average point to point distance of 0.079 m over the entire set of results. To determine the effect of this error on current velocity, the velocity of the points at each time-step was calculated and compared to the known velocity of the point, which was stationary and hence 0 cm.s^{-1}. Figure 4-7 provides a time-series plot of the velocity error for the points calculated using an f value of 4.5 mm and 4.18 mm as well as the horizontal velocity over of the drone over the same period. For simplicity's sake the time has been benchmarked at the start of the first flight and each period in which the drone was not over the tape has been condensed to 30 seconds and highlighted in grey below.

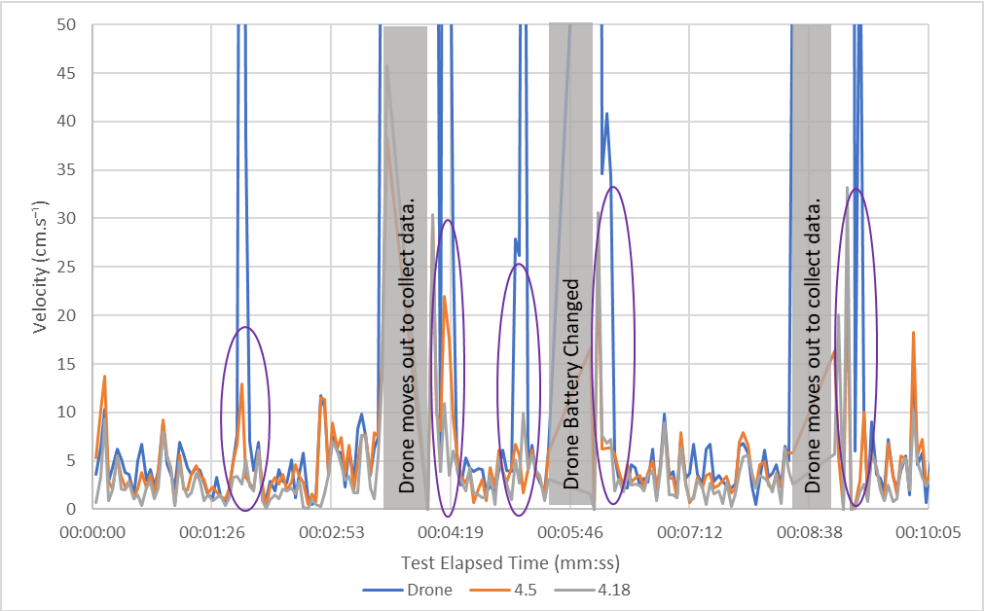

Figure 4-7: Time-Series Plot of Calculated Error Velocity

What was notable was that the velocity error of the measurements with an f set at 4.18 mm were lower than that of 4.5 mm which further pointed to the use of the f value calculated in section 4.1.1.2. Also, for the most part the horizontal velocity of the drone was quite low as it hovered above the tape, with a magnitude similar to the calculated velocities below. This could be due to the drone sensing that it was moving, within the accuracy of the on-board GPS, refer to Section 2.1.2; however, this appears to be much more accurate than the 0.3 m reported by DJI.

There were 5 events of interest along the time-series plot which have been highlighted with circles, which correlate to times at which the drone was no longer hovering and was moving horizontally. As the drone velocity increased so did the "error" velocity of the point below which indicated that the accuracy of the results decreased as the drone was in motion, like the vertical movement noted in 4.1.1.1 above. Therefore, a drone velocity threshold could be set at which point the measurements were excluded from the results. It was suggested that 20 $cm.s^{-1}$ was used as this allows for some autopilot correction of the drone in the wind but was far less than when operator input was provided, and the drone velocity could reach up to 630 $cm.s^{-1}$.

This was processed in excel to get the average velocity every 6 , 10 , 14 , 18 and 22 seconds which is indicated in Figure 4-8 below.

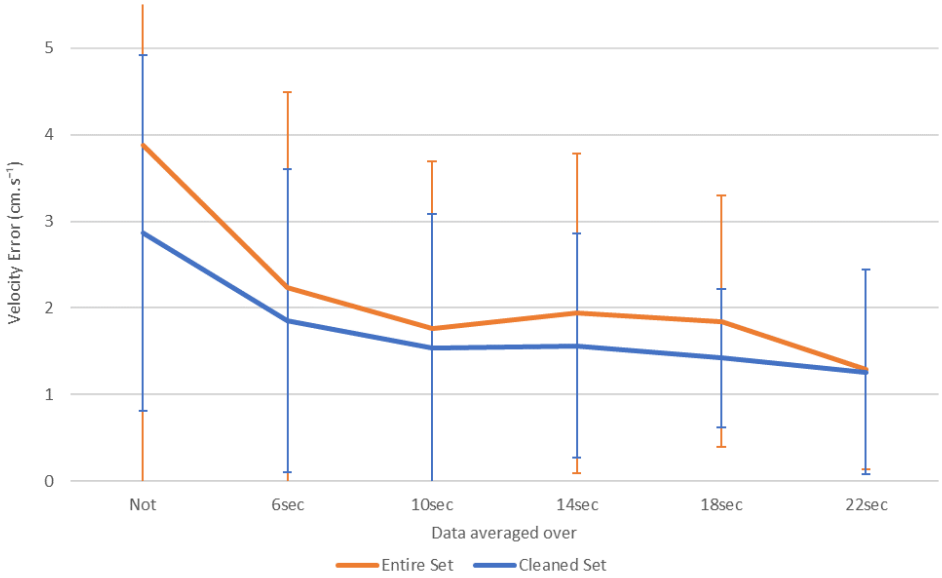

Figure 4-8: Averaged Velocity Error Mean ±1σ Results

This illustrates how cleaning up the data from measurements while the drone was in motion already reduced the mean error from 3.9 cm.s^{-1} to 2.9 cm.s^{-1} (a 26 % reduction), even before any averaging took place. Once the set had been averaged the mean error dropped further to 1.9 cm.s^{-1} but the reduction soon flattened out at around 1.5 cm.s^{-1} when averaging every 10 to 22 seconds. The deviation reduced to a minimum when averaging every 18 seconds with all calculated velocity being between 0.26 and 2.8 cm.s^{-1}.

4.1.2.2 Over Water Testing

The poles used for GCP's just behind the breakers, as described in section 3.4.1.2 above, proved to be quite successful and stationary points were easily tracked. This provided a good reference point to compare to the movement of the drifter which was placed nearby. Figure 4-9 below shows an extract from velocity time-series plot for the first flight which highlights the typical relationship between the GCP error found and the velocity of drifters 1D, 2D and 3D. The GCP velocity shown were the averages of the four stakes placed behind the breakers. On average the velocity error found at the GCP's was approximately 22% of the current velocity found at the drifters.

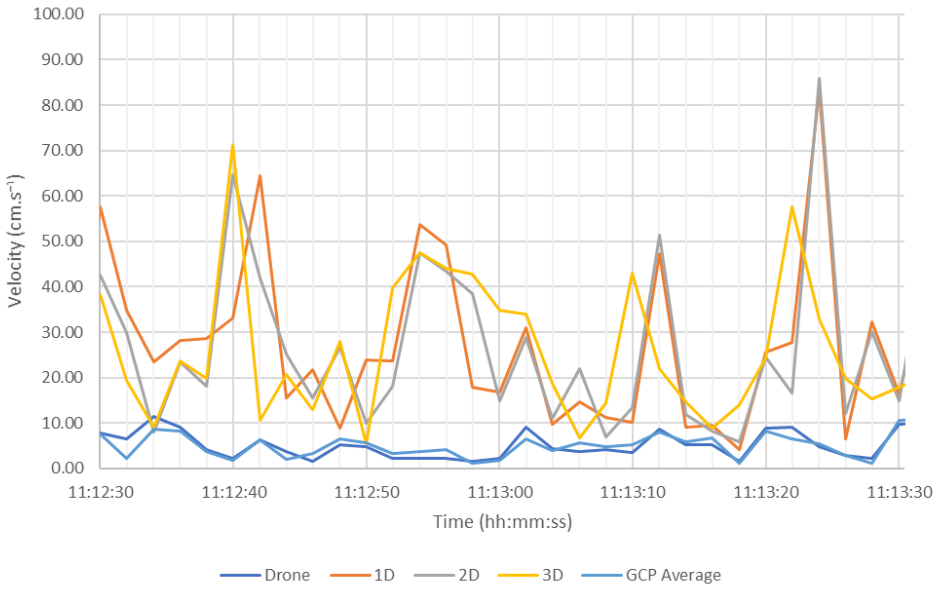

Figure 4-9: Example of Velocity Time-Series Plot from Calibration Test Flight 1

This figure also highlights that the error follows the movement of the drone which implied that this error could be reduced easily with better GPS technology, such as the Phantom RTK, which increases the hovering accuracy.

It was also found that during these tests when the drone rotated to return to the beach, an inaccurate yaw reading was recorded in the images which in turn generated excessive drifter movements between 3.75 m and 5.63 m, shown in Figure 4-10. It appears as if the underlying sediment location similarly shifts, implying that it was not current induced and must be due to incorrect readings. This again highlighted the need to clean up the raw data from flight induced errors when the drone was in motion.

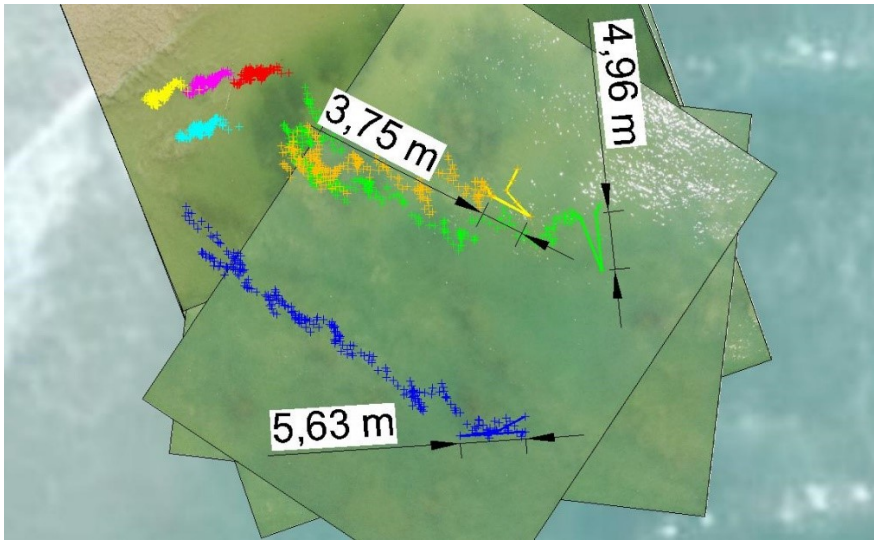

Figure 4-10: Drifter Coordinate Result Example During Drone Rotation

The GCP's may have worked for the conditions on the specific day of testing, but if the wave climate was any larger, there would have been an increased deployment risk in attempting to place the stakes behind the breakers. This would also negate some of the benefits of using this drone method over a

more traditional method such as GPS drifters. As it was there were instances when a large set of waves came in obscuring the GCP stakes, as seen in Figure 4-11. This also risked moving the stakes and influencing the error results. To mitigate this more than one stake was used to average out any movements during testing.

Figure 4-11: Waves Obscuring the GCP Stake During Testing

Another effect which was noted was any instance where a wave picked up the drifter which surfed along generating excessive velocity, as seen in Figure 4-12 and Figure 4-13. This was easily picked up from the images and it could be flagged when processing the images in AutoCAD such that these coordinates could then excluded from the data set if required.

Figure 4-12: Drifter Surfing Effects

Figure 4-13: Drifter Caught in Wave

During testing sunlight could obscure the drifter if in the correct angle for the glare to reflect to the drone, as seen in Figure 4-14. This would typically occur as a wave passed underneath but would

need to be considered in planning the time of data collection. A polarised filter fitted to the camera lens could reduce this effect somewhat.

Figure 4-14: Sunlight Reflection

During large wave events where sea foam was generated in abundance within the bay it became difficult to detect the drifters as seen in Figure 4-15 below, which shows a drifter entering foam in frames 2 seconds apart. This could be mitigated by using a larger drifter protruding further above the water surface which would in turn require additional baffles below to prevent surfing. A drifter which reflects a specific colour spectrum coupled with an enhanced spectral camera or a thermal camera could presumably see through the foam. One such solution is the Zenmuse XT camera which is a commercially available thermal camera which is compatible with the DJI Inspire 2 drone (DJI, 2019d).

Figure 4-15: Drifter Obscured by Sea Foam

Again, the data was cleaned from high drone movements and then averaged over different periods to smooth out the error. Figure 4-16 provides the results of this process and shows that when averaging over 14 seconds the difference between the cleaned data and the entire set appears minimal. When averaging over more than 14 seconds the effect of the localised errors generated by the drone movements seem to be averaged out. The overall mean error decreased with increased averaging periods, like the tests on the beach; however, this flattened out after 14 seconds just under 2 $cm.s^{-1}$.

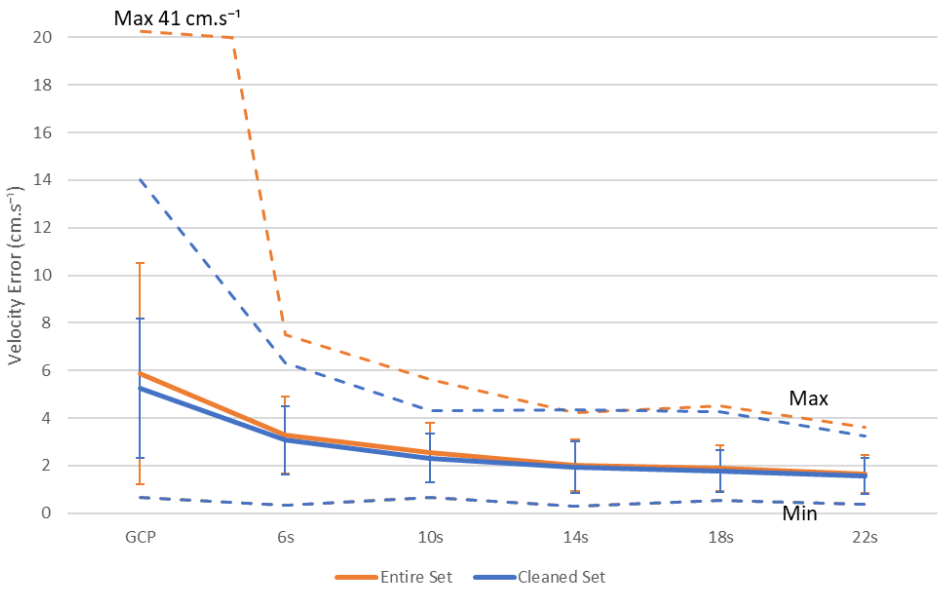

Figure 4-16: GCP Velocity Error Results for Flight 1

Over the same flight the drifter velocity followed a similar trend with the mean reducing with higher averaging periods as seen Figure 4-17 below. Increasing the averaging period past 10 seconds only provided incremental reductions in the velocity mean and range of results.

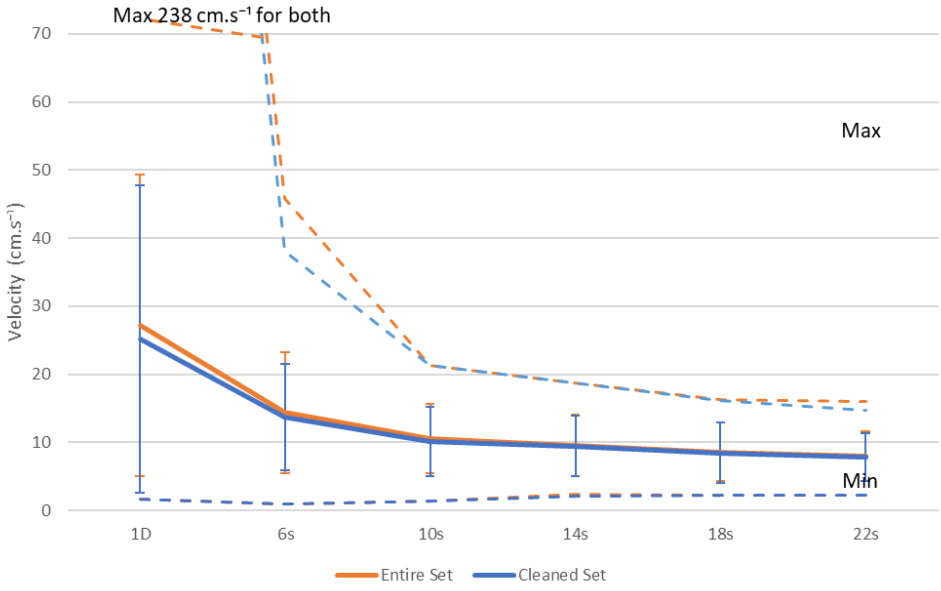

Figure 4-17: Drifter Velocity Results for Flight 1

The results for the second flight where correlated with the first, as shown in Figure 4-18 and Figure 4-19 below. The GCP velocity error and drifter velocity decreased at 6 seconds and then flattened out with increasing averaging periods. The average difference between the cleaned set and the entire set also bacame minimal after averaging.

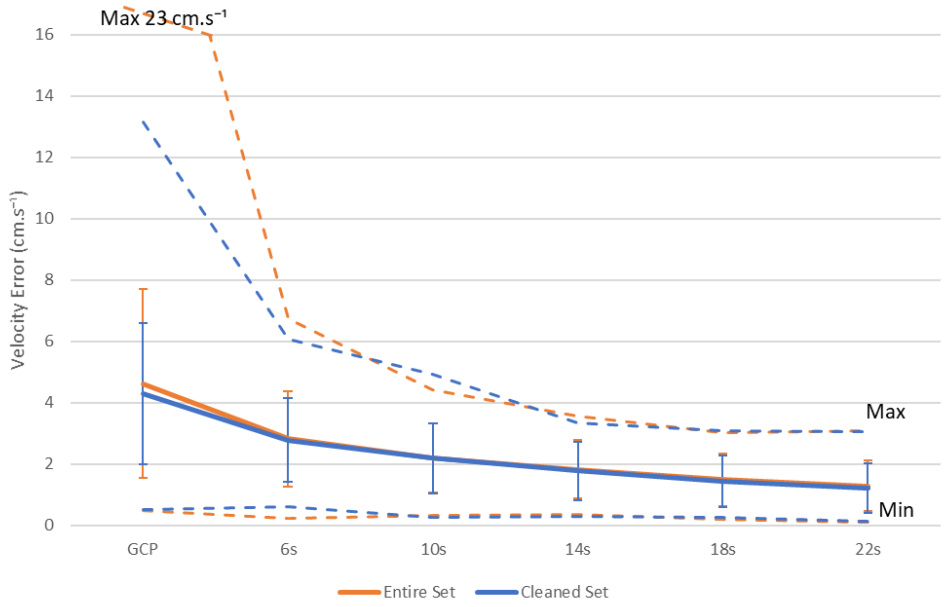

Figure 4-18: GCP Velocity Error Results for Flight 2

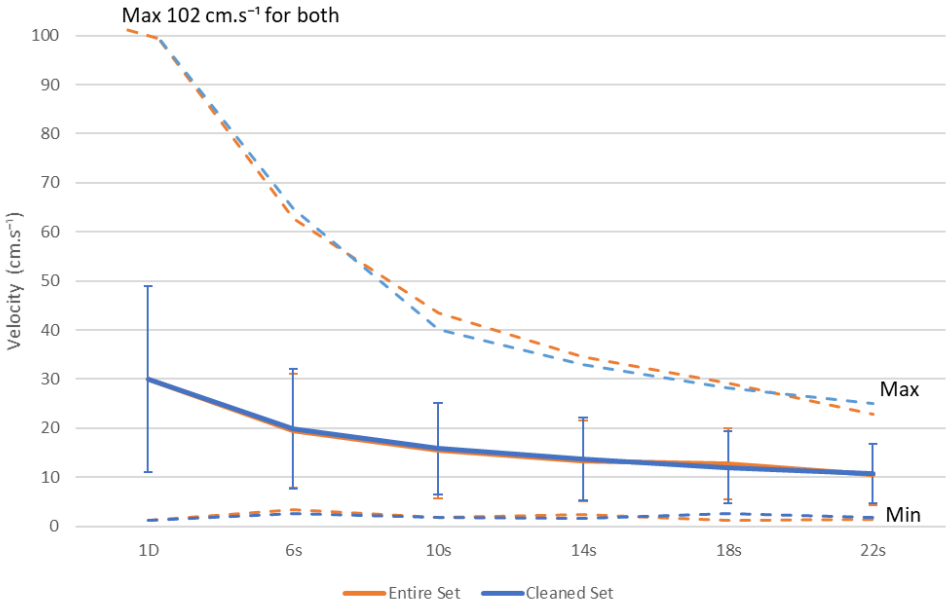

Figure 4-19: Drifter Velocity Results for Flight 2

The trend for the measured velocity and error to decrease with increasing averaging periods was due to the coordinates used in the calculations all tending towards the centroid of the entire set of data, see. This lead to movements of the drifter, such as the arc back (circled in Figure 4-20 below), being averaged out and hence a much lower current velocity being calculated. The green path averaged over 6s, followed the drifters as they moved north and then south in line with the incoming waves. The red path averaged over 6s, does not show this movement rather moving to the centre of all these points. This may be beneficial in excluding the wave effects and providing an overall current, but this also reduced the resolution of the data.

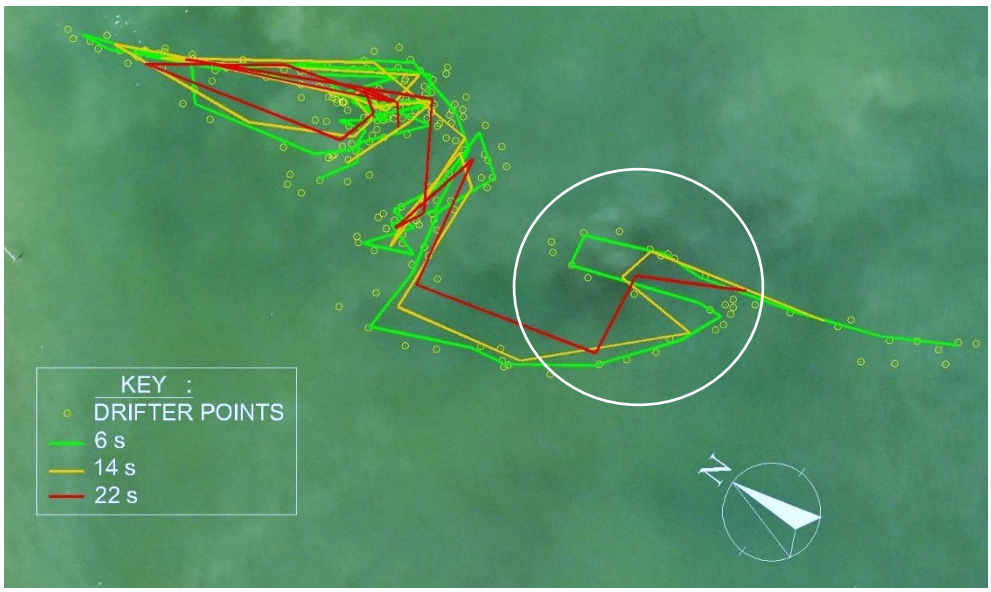

Figure 4-20: Drifter Tracks Averaged

A lower averaging period would be useful should local small-scale movements be of interest, such as oscillatory currents, or if the current magnitude was small. In these circumstances, a 6 to 10 seconds averaging period seemed reasonable for processing data although a higher velocity error was then included in the results. In cases where a longer-term current trend was required, such as a steady longshore current or tidal current, an averaging period longer than 22 seconds would smooth out short term wave effects while further smoothing any errors generated during data collection.

4.1.2.3 Drone Elevation Tests

The elevation of the drone influenced the number of pixels which picked up the drifter making it harder to track. The less clear image on the right of Figure 4-21 was taken with the drone at an altitude of 100 m and while a larger area could be covered at once, the drifter only took up a few pixels.

Figure 4-21: Drifter Imaged from Altitudes 30 m (left) and 100 m (right)

A higher resolution camera such as the Inspire 2's 20 MP camera, vs the Mavic Air's 12 MP would allow for clearer images at a higher altitude. Figure 4-22 illustrates the drifter taken from the Mavic Air at an altitude of 30 m, shown on the left, while the Inspire 2 took the same drifter at an elevation

of 40 m, shown on the right. The Inspire 2 has a much sharper image even at the higher altitude which allows for the drifter to be picked out easier.

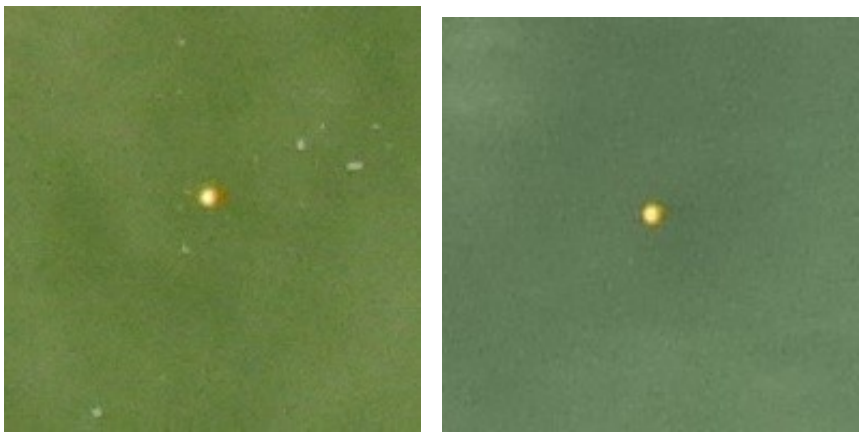

Figure 4-22: Comparison Between Drifter from Mavic Air (left) & Inspire 2 (right)

4.1.3 Calibration Conclusions

Initial scaling found that the focal length of 4.5 mm for the Mavic Air reported by DJI led to a 10% underestimation of a 2.5 m length measured on the ground; hence, the focal length was calibrated and set to 4.18 mm which resulted in better overall results. This could be due to slight discrepancies in the camera manufacture; hence the calibrated number was used for the remainder of the calculations. An elevation correction of 1.6 m was also added to each altitude to account for the take-off location of the drone in relation to the water level.

It was noted that whenever the drone velocity increased, either horizontally or vertically, the error increased accordingly. This led to some measurements during calibration being excluded as the drone ascended from one elevation to the next where outlying measurements as low as 1.65 m for the 2.5 m tape were noted.

The average instantaneous error, characterised as a velocity determined by tracking stationary points on the ground, ranged between 4 $cm.s^{-1}$ and 6 $cm.s^{-1}$ which then reduced to around 2 $cm.s^{-1}$ when averaging out the points over 10s for all calibration tests. During the same tests the average drifter velocity measured were around 30 $cm.s^{-1}$ instantaneously (which included orbital velocity from waves) and then reduced to between 18 $cm.s^{-1}$ and 10 $cm.s^{-1}$ for the averaged results corresponding to longer period currents.

4.2 Environmental Conditions

In total, 10 trips were made to Monwabisi with the Mavic Air to collect data for currents. This excluded the preliminary flights with the Phantom which did not yield usable images. Each data collection trip was labelled sequentially FA to FJ and listed in Table 4-1. During each trip up to three flights took place, with the batteries changed in between.

Table 4-1: Data Collection Trip List

	Date	Number of Flights	Time (hh:mm)		Comments
			Start	End	
FA	2018-05-15	1	10:15	10:29	First Mavic-Air test.
FB	2018-07-17	1	10:37	10:40	Further initial testing.
FC	2018-12-11	3	06:51	07:33	
FD	2019-01-07	3	06:54	07:39	Big wave conditions.
FE	2019-01-11	2	07:32	08:00	
FF	2019-01-17	3	07:55	08:39	
FG	2019-01-28	0	08:00	08:40	High winds prevented flight.
FH	2019-02-05	3	08:17	10:13	
FI	2019-02-07	3	08:17	09:52	Inspire 2 comparison.
FJ	2019-04-11	3	11:07	11:52	Calibration testing.

Wave data was provided by Kistner on behalf of PRDW Port and Consulting Engineers, on the date each data collection took place and is provided in Table 4-2. These measurements were located at the wave generation line, approximately 1000m offshore from the Monwabisi groyne, in Kistner's Model which was set up to correlate with CSIR's wave measurements. Of the tests, FE on the 11th Jan 2019 had very similar conditions to that of Kistner's case MB610 which was tested from the CSIR report. In the rest of the conditions the wave heights were generally lower than those tested previously, as seen in Figure 4-23. The spread of water levels during collection was in a similar range to that tested previously and the wave periods were close to the 12 seconds tested by Kistner.

Table 4-2: Sea Conditions During Data Collection

	Hs (m)	Tp (s)	Dir (°)	Predicted Tide (m MSL)	
				Start	End
FA	1.8	16	180	-0.6	-0.6
FB	0.8	10	180	-0.2	-0.2
FC	0.7	11	189	0.7	0.5
FD	2.2	19	187	0.5	0.2
FE	1.5	12	192	0.7	0.6
FF	1.0	12	185	0.0	0.2
FG	1.1	9	150	0.6	0.7
FH	0.9	11	178	0.0	-0.3
FI	1.2	10	158	0.2	-0.2
FJ	0.8	12	190	-0.1	-0.3

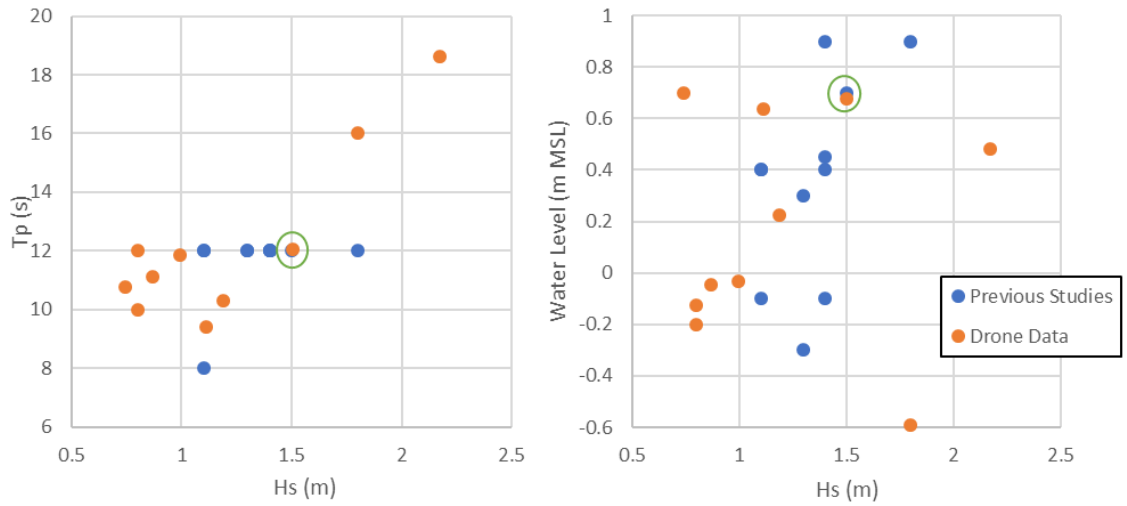

Figure 4-23: Data Collection Comparison to Previous Studies

Most of the data collection trips took place in the morning before the wind picked up. With no access to an anemometer, or a local wind station the most reliable wind measurement was for Strand provided by SAWS (see Table 4-3). This does provide an indicative magnitude of the wind conditions during testing. The wind did not prevent testing taking place apart from test FG on the 28th of Jan. On this day the wind was substantially higher than the others, with readings nearly double that of the next highest reading at Strand.

Table 4-3: Wind Conditions During Data Collection

	Strand		Cape Town Airport	
	Speed (kts)	**Wind Dir (°)**	**Speed (kts)**	**Wind Dir (°)**
FA	1.9	230	1.2	175
FB	1.3	235	1.4	159
FC	1.6	49	1.2	138
FD	0	0	6.7	206
FE	4.1	350	7.7	328
FF	1.4	223	3.3	328
FG	10.2	118	4.3	206
FH	3.2	177	5.2	223
FI	6.05	104	3.3	204
FJ	5.0	260	6.0	200

4.3 Current Velocity

For the processing of the remainder of the tests the focal length f was kept at 4.18 mm and an elevation correction factor of 1.6 m was used to account for handheld drone release from the beach.

4.3.1 Summary of Tests

The results of each data set are shown below.

4.3.1.1 Data Set FA

During the first data collecting test with the Mavic Air drone, the sea conditions were energetic with a Hs of 1.8 m at a period of 16 seconds which was above average for the area. The test was carried out during low tide; hence, the drifters often experienced surfing effects before being washed up on the beach. The longest path, shown in Figure 4-24 below, was 30 m with some oscillations due to waves before being lost in wave sea foam and turning up on the beach. Still, 370 points were collected which provided initial currents along the beach towards the spur.

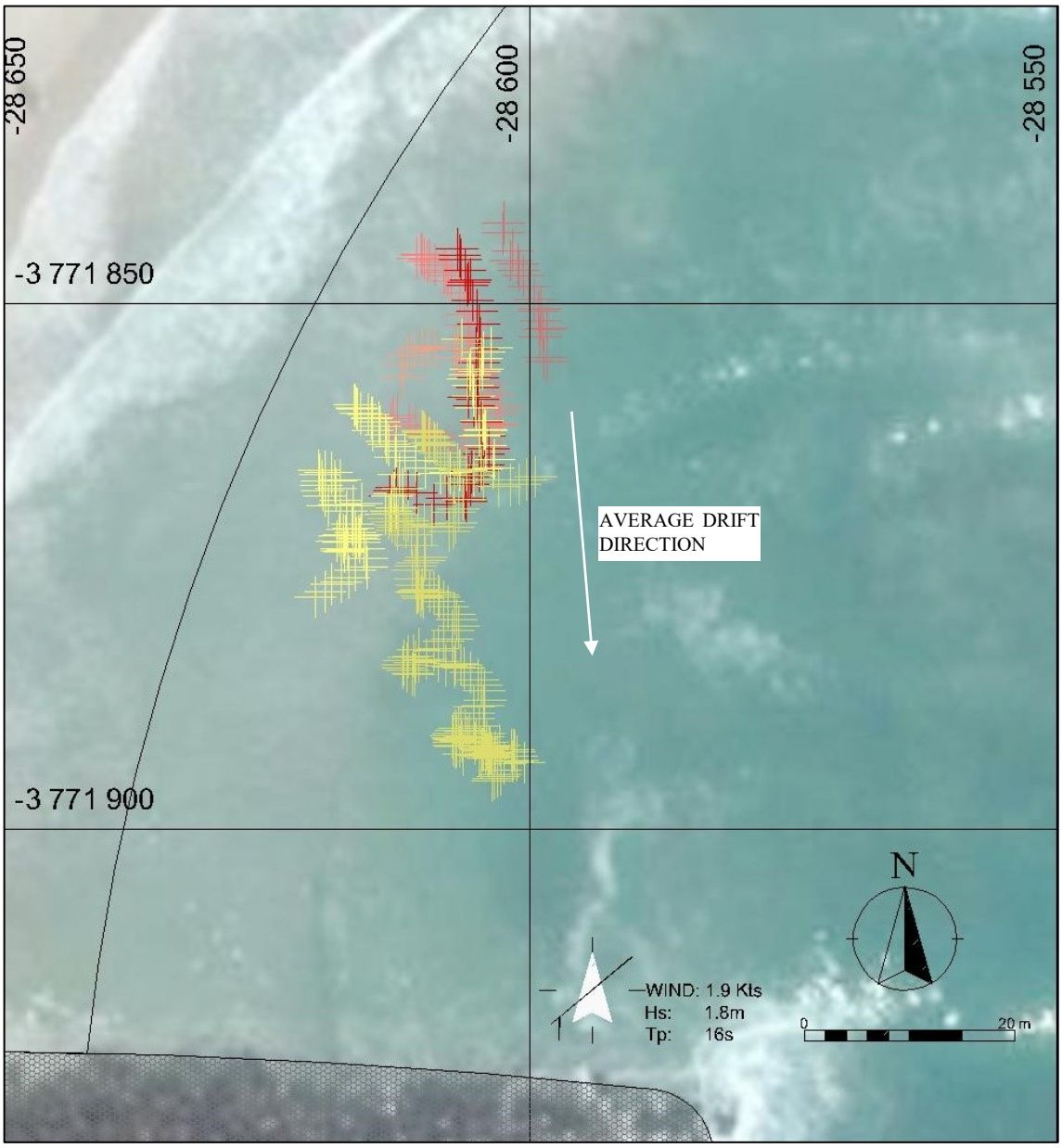

Figure 4-24: Flight FA Drifter Paths

The conditions during the test most resembled that modelled by Kistner in MB110 as both occurred at similar low tide levels. However, the wave conditions were stronger during the on-site measurements. Therefore, as expected through equation (2-2), the overall velocity exceedance profile was found to be higher than that found by Kistner (see Figure 4-25).

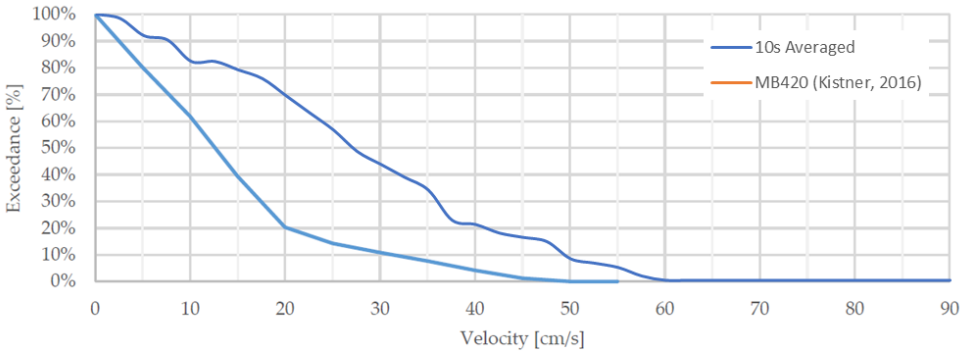

Figure 4-25: FA – MB420 Velocity Exceedance Comparison

With the stronger wave conditions, it was expected that the maximum U_{PA30} current velocity of 31 cm/s^{-1} measured at point I, as seen in Figure 4-26 below, was larger than that modelled by Kistner of 21.2 cm/s^{-1}. The current pattern aligns with the model, but there were not enough measurements to get a full characterisation within the bay.

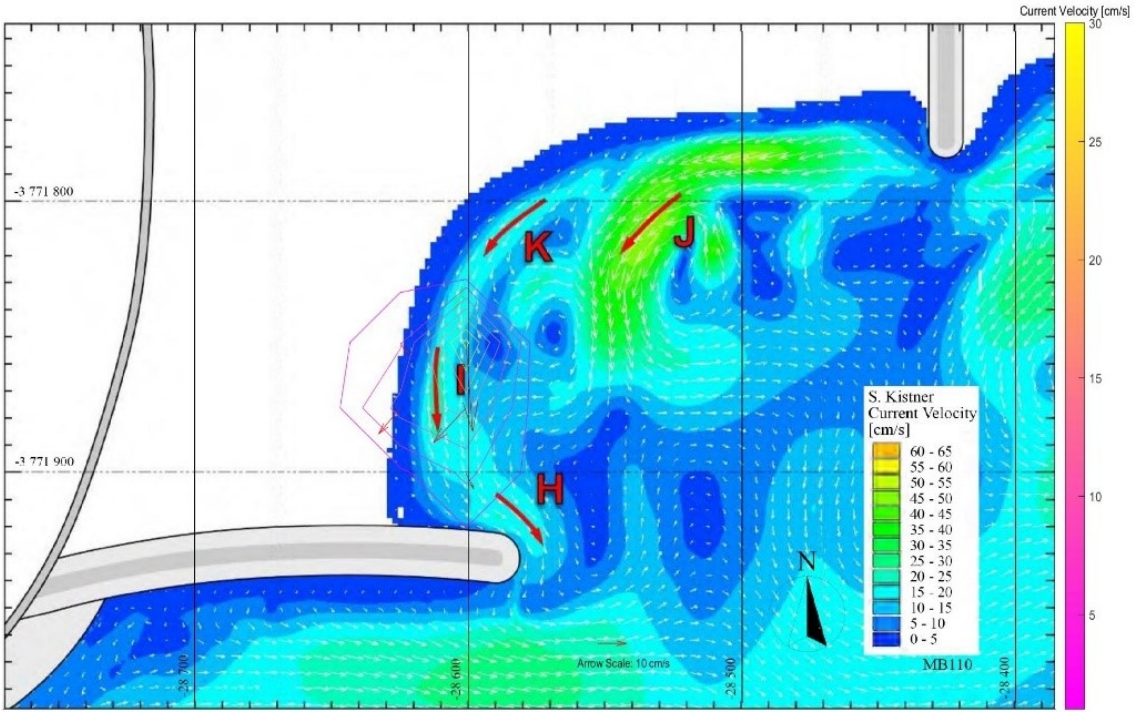

Figure 4-26: FA – Comparison of U_{PA30} Results

The 10s averaged results, in Figure 4-27 below, showed a maximum current of 56 cm/s^{-1} near where the drifters were launched from the beach and then moving towards the head of the spur in an anti-clockwise direction around the bay.

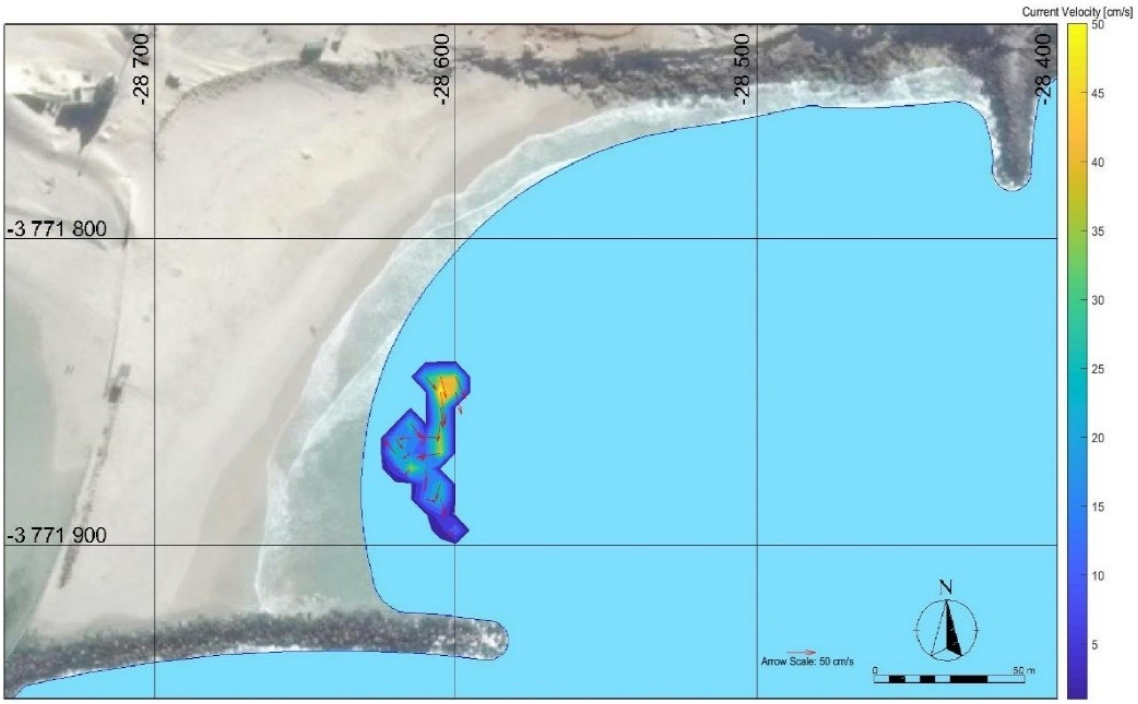

Figure 4-27: FA – 10 Seconds Averaged Current Velocities

4.3.1.2 Data Set FB

The next set of data was collected along with a site inspection of the nearby desalination plant construction and an attempt to use Drone Deploy to survey the area with Photogrammetry. A small number of 217 drifter coordinates were collected, as shown in Figure 4-28 below, which did not lead to substantial current measurements.

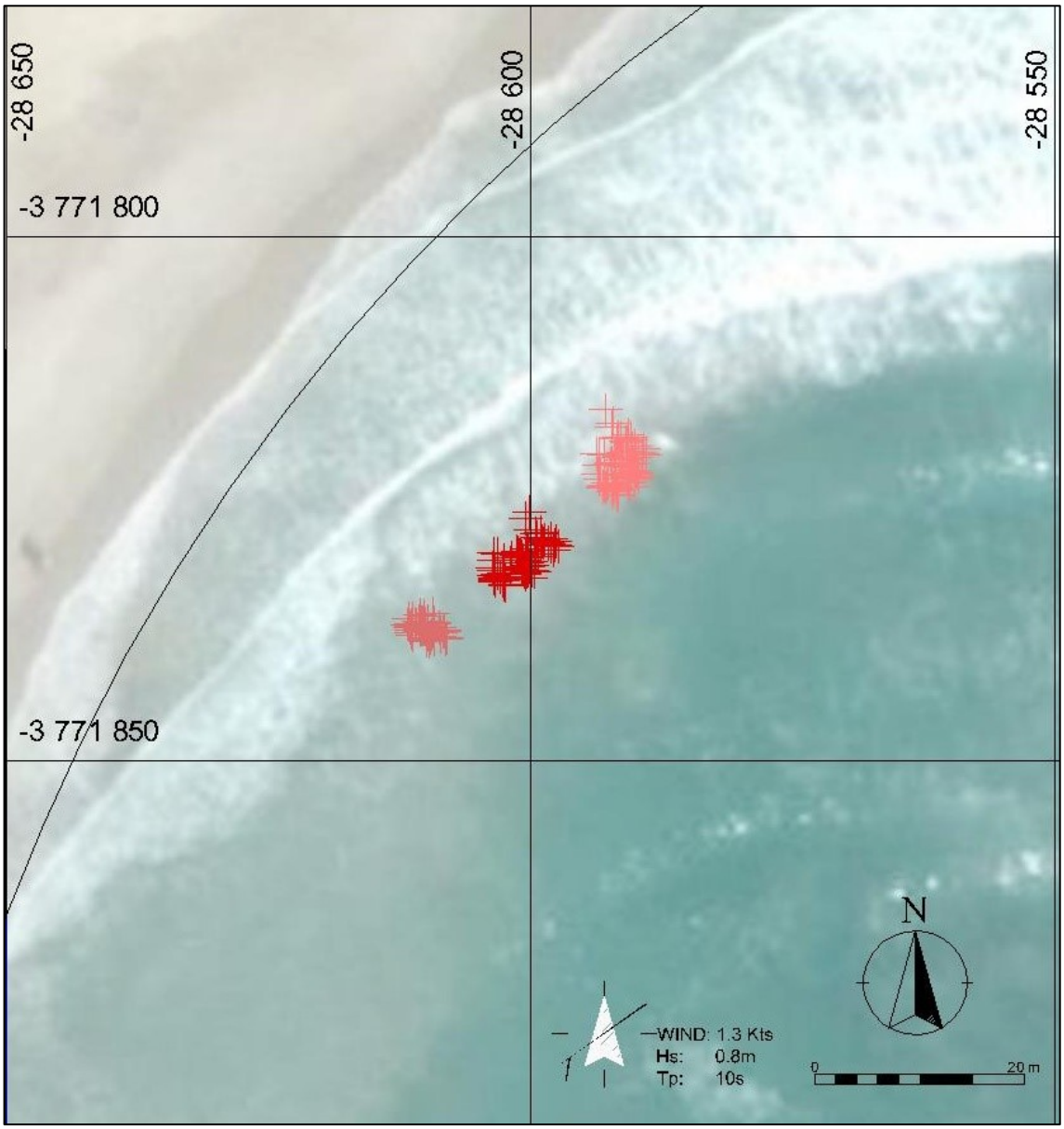

Figure 4-28: Flight FB Drifter Paths

The lack of sufficient measurements resulted in an erratic exceedance curve which was below that of Kistner, as seen in Figure 4-29.

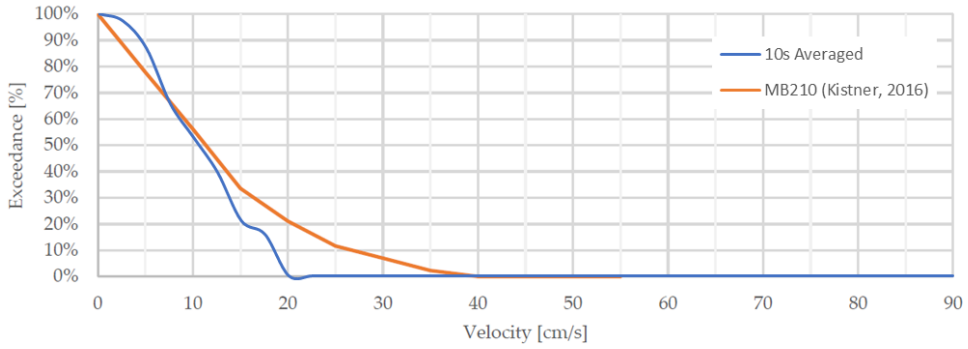

Figure 4-29: FB – MB210 Velocity Exceedance Comparison

The three drifters deployed remained in close proximity of the area they were deployed and bobbed in the waves. This resulted in vectors which pointed towards themselves when averaged over the

25 m for the U_{PA30} results with a maximum of 5 cm/s^{-1}. These vectors were in an opposite direction to Kistner's results of 26 cm/s^{-1} from his MB210 model tests which had similar tide levels although the waves were smaller during the on-site tests, as seen in Figure 4-30 below.

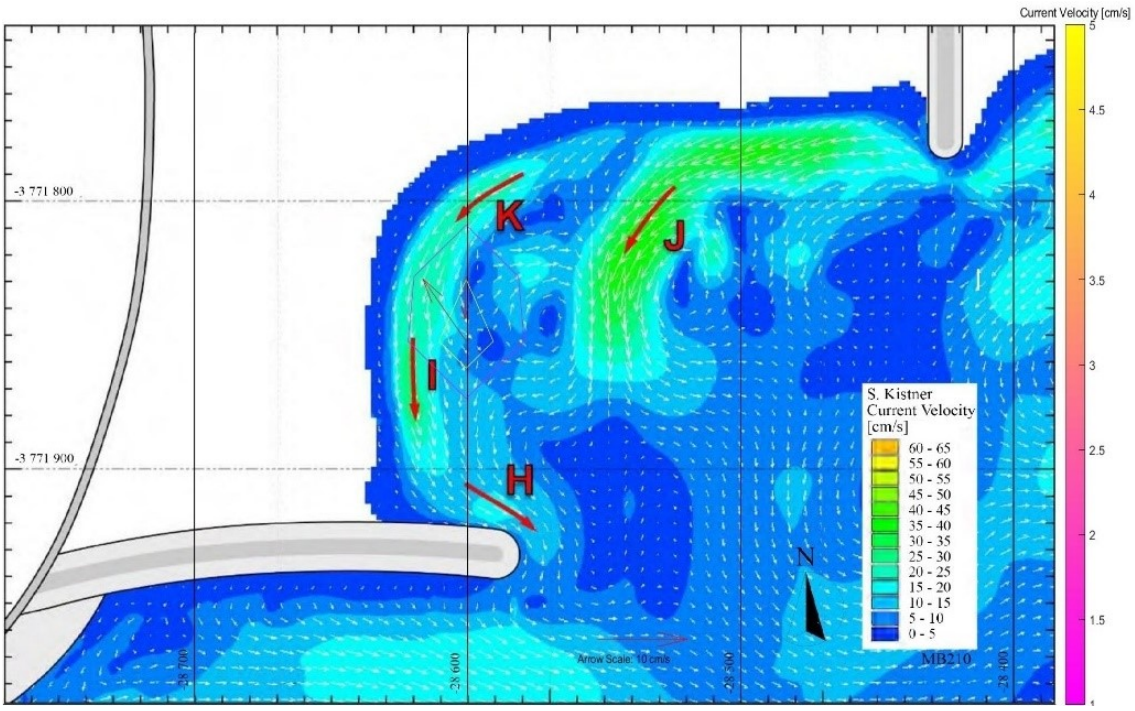

Figure 4-30: FB – Comparison of U_{PA30} Results

The 10 seconds averaged results, shown in Figure 4-31, provided a maximum current of 18 cm/s^{-1} with the remainder of the results averaging around 5 cm/s^{-1} with no clear directional pattern as the drifters bobbed in the waves. Substantially more readings are required to characterise the current patterns being studied.

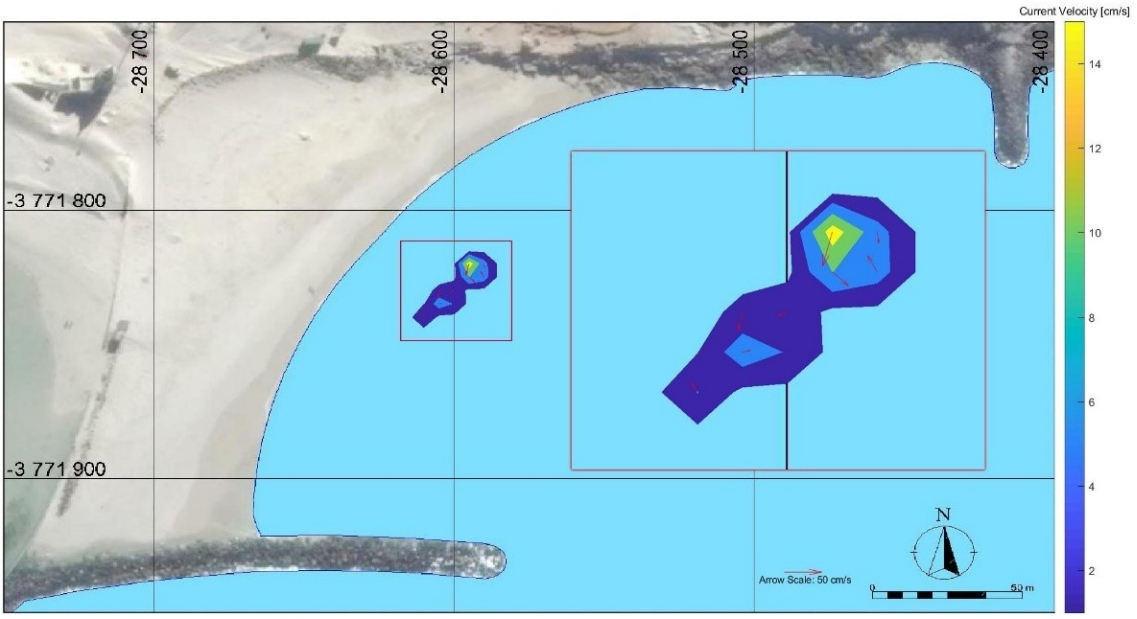

Figure 4-31: FB – 10 Seconds Averaged Current Velocities

4.3.1.3 Data Set FC

During the third set of current measurements the currents where found to be quite low with the longest drifter path along the shoreline, 50 m towards the spur over the 12-minute flight. A test was therefore carried out at the groyne in the hope of stronger currents, shown to the right of Figure 4-32 below. 2157 drifter measurements were taken; 1312 over two tests at the beach and 845 during a third at the groyne.

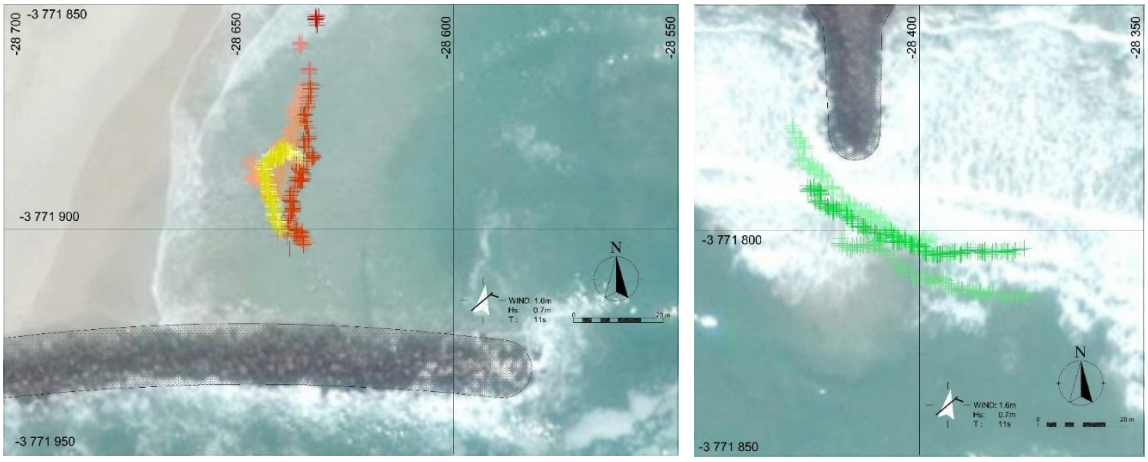

Figure 4-32: Flight FC Drifter Paths

This test provided a much better idea of the currents in the bay with a maximum U_{PA30} current of 6 cm/s^{-1} measured at point I, as can be seen in Figure 4-34 below, with the maximum over the entire test being 15 cm/s^{-1} at the breakwater. The low currents were possibly due to the low wave height and period along with the high tide during the test, which is shown in Figure 4-33 below. The closest test by Kistner, namely MB430, resulted in currents of 28.8 cm/s^{-1} at point I most likely due to the higher wave height of 1.1m tested.

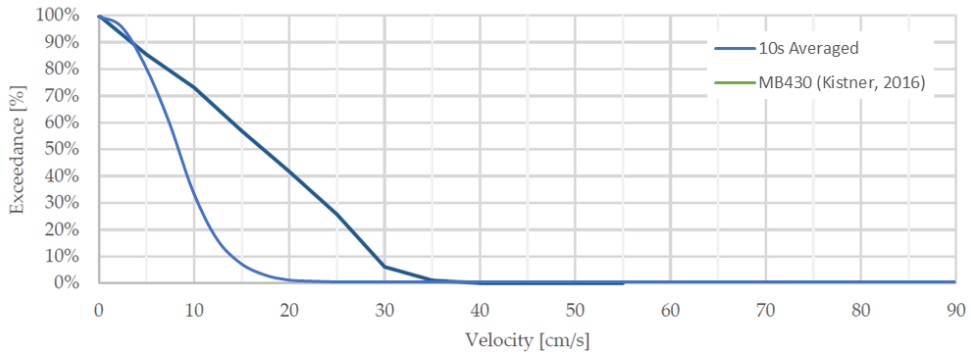

Figure 4-33: FC – MB430 Velocity Exceedance Comparison

The currents off the groyne start from 8 cm/s^{-1} at the head increasing to 15 cm/s^{-1} off the end which corresponds to those read off Kistner's MB430 results, also provided in Figure 4-34, which seems to be between 5 and 25 cm/s^{-1} while also following a similar flow path, as expanded in Figure 4-36.

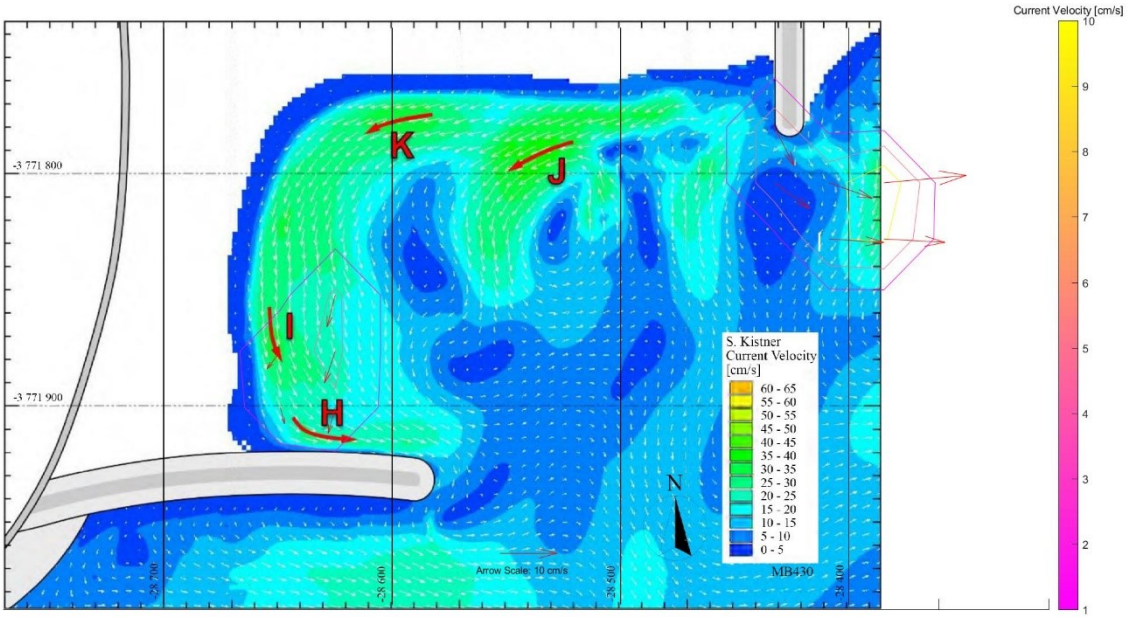

Figure 4-34: FC – Comparison of U_{PA30} Results

The 10 seconds averaged results showed currents of 14 cm/s^{-1} running longshore in a clockwise direction and 19 cm/s^{-1} at the tip of the groyne to the east, as seen in Figure 4-35 and expanded in Figure 4-36 below.

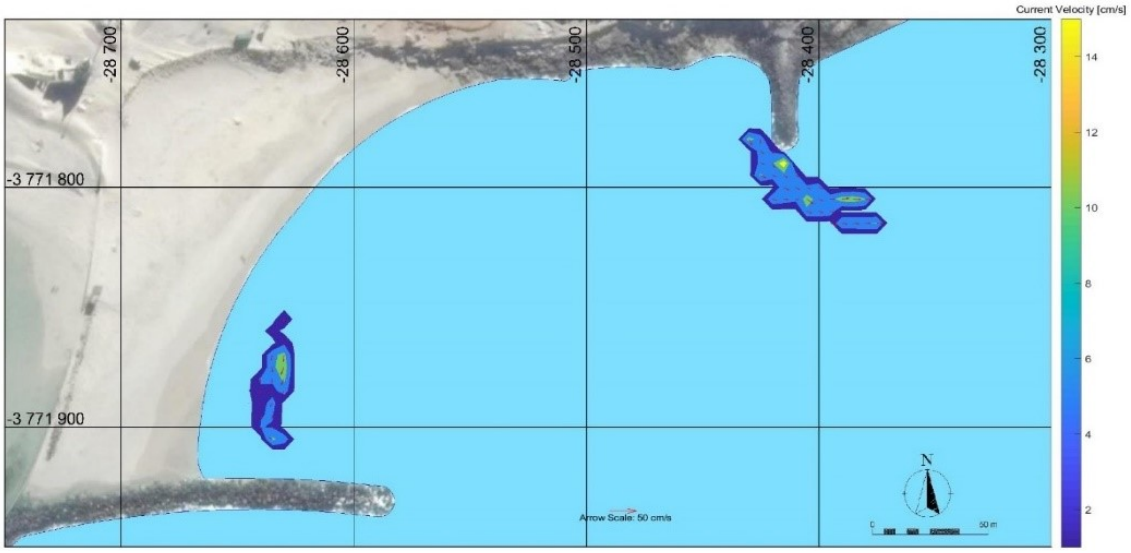

Figure 4-35: FC – 10 Seconds Averaged Current Velocities

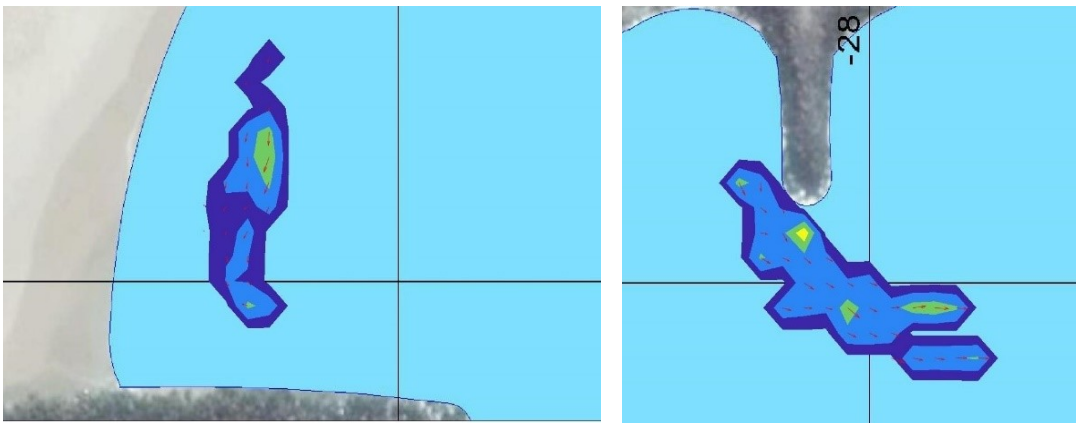

Figure 4-36: FC - 10 Seconds Averaged Current Velocities (Zoomed-In)

4.3.1.4 Data Set FD

Set FD was taken during the largest Hs at 2.2 m for the study during an average water level of 0.3 m which was comparable to Kistner's calibration test MB420 which had a water level of + 0.4 m and a Hs of 1.4m. A total of 3936 drifter positions were recorded during the test. Of these, 288 points were omitted, shown as light green in Figure 4-38 below, as it appeared that the drifter was caught in the surf zone and hence moved clockwise along the bay near the beach until being washed up on the beach. This movement seemed unusual as it was contrary to the predominant current pattern during this set of measurements, circled in red in Figure 4-37 below.

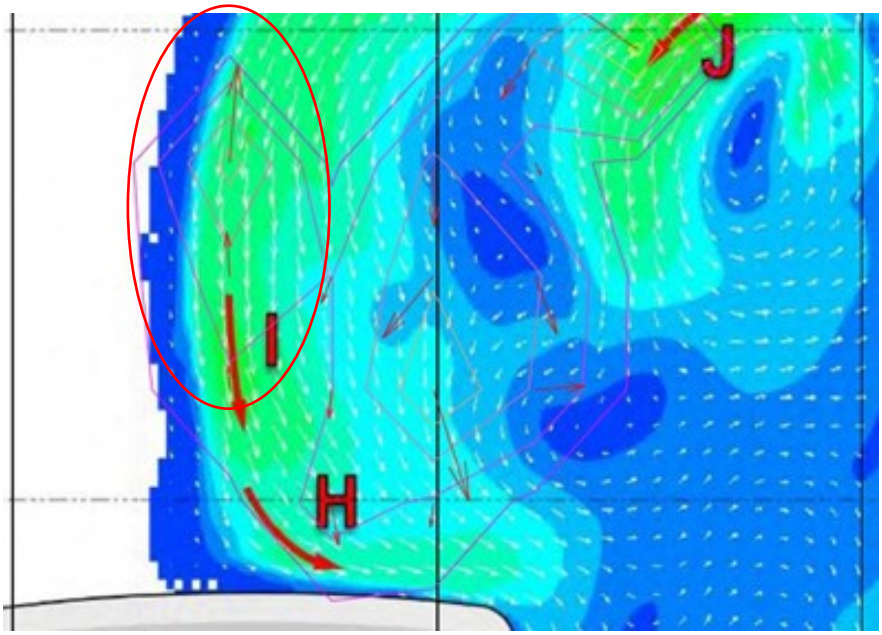

Figure 4-37: Entire FD Drifter Data Results with Excluded Currents Circled in Red

Figure 4-38 shows the predominately clockwise route of the drifters within the bay with the two green paths originating from the top right corresponding to drifters from the first deployment which had circulated around the entire bay and then picked up in the third deployment. Most drifters progressed towards the head of the spur in a zig-zag pattern as the wave sets entered the bay although some did appear to be trapped in a lull behind the spur

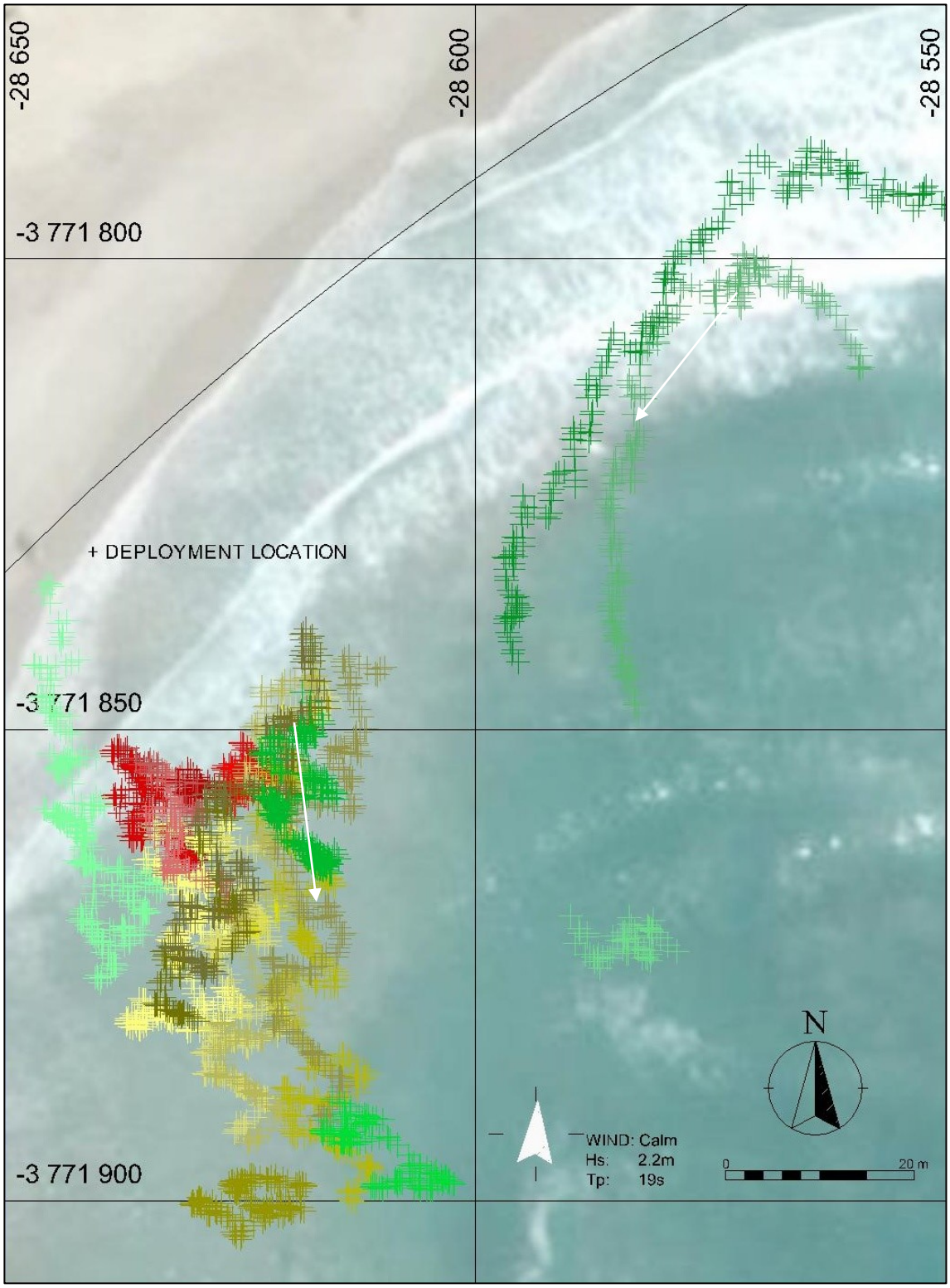

Figure 4-38: Flight FD Drifter Paths

Unfortunately, it was difficult to pick up any drifters near the head of the spur as the sea foam generated by the waves breaking past the spur obscured the floating drifters (see Figure 4-39).

Figure 4-39: Sea Foam Generated by Large Waves at the Spur Head on the 2019-01-07

During test condition MB420, Kistner estimated the U_{PA30} velocity to be 30.9 cm.s^{-1} longshore near the beach, at point I, towards the spur, and a rip current of 37.3 cm.s^{-1} at point J. The drifters showed a U_{PA30} longshore current of 20.1 cm.s^{-1} at point I with a current of 26.5 cm.s^{-1} at point J towards the beach, as indicated by Figure 4-41 below. The overall velocity exceedance profile for the test matched the measured results well, as seen in Figure 4-40.

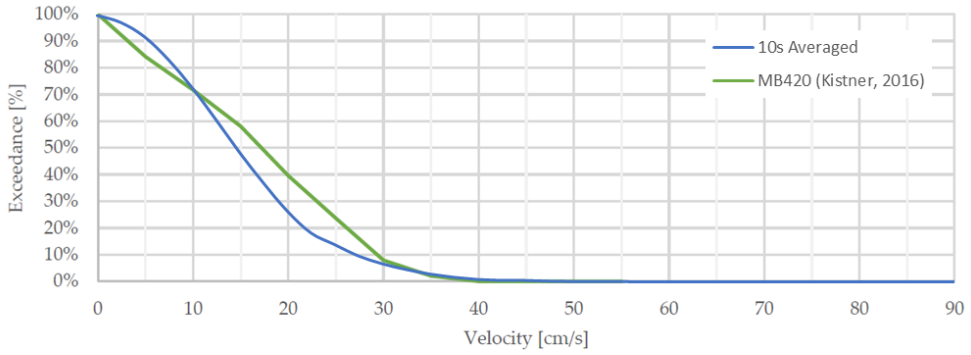

Figure 4-40: FD – MB420 Velocity Exceedance Comparison

The difference in the direction of the rip current at point J could be due to the waves entering the bay causing surfing effects with the drifters pushing them more towards the flow direction at point K.

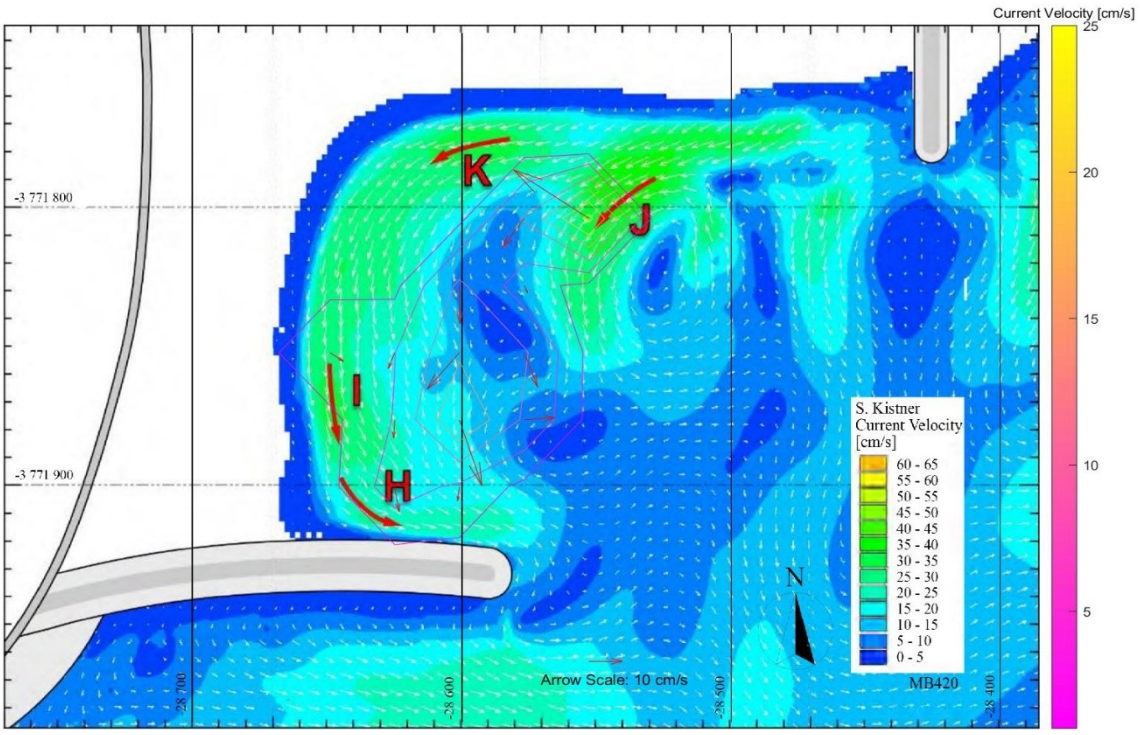

Figure 4-41: FD – Comparison of UPA30 Results

Figure 4-42 is a better representation of the flow pattern within the bay with the anti-clockwise circulation forming a rip along the beach and out the spur.

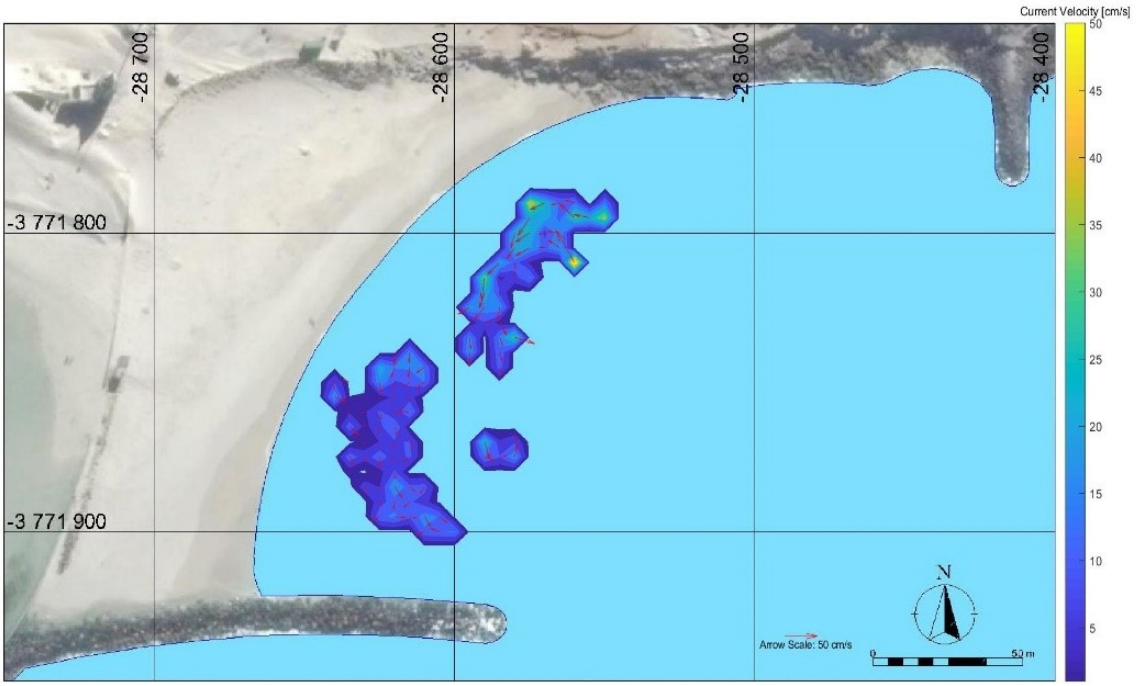

Figure 4-42: FD – 10 Seconds Averaged Current Velocities

4.3.1.5 Data Set FE

It was expected that the results from FE would correspond to the results from Kistner's calibration test MB610, which also corresponded to the CSIR's calibration test, as the sea conditions were similar. However, the drifters did not follow the anti-clockwise circulation pattern found in their results as the drifters were launched from the beach to the west and then moved in a clockwise

direction around the bay as seen in Figure 4-43 below. During this test the drifters were launched during the first flight and then picked up again for the second flight and hence the entire drifter path was approximately 130 m over approximately 25 minutes.

This could be due to the wind and the waves coming from the south and consequently the drifter surfed towards the beach on the north. Unfortunately, as it was overcast and the sea was murky, it was not possible to observe sediment movement below the drifter to test if the surface was moving in a different direction to the column below. It should be noted that the water surface did not show signs of high winds such as white caps or excessive wind waves.

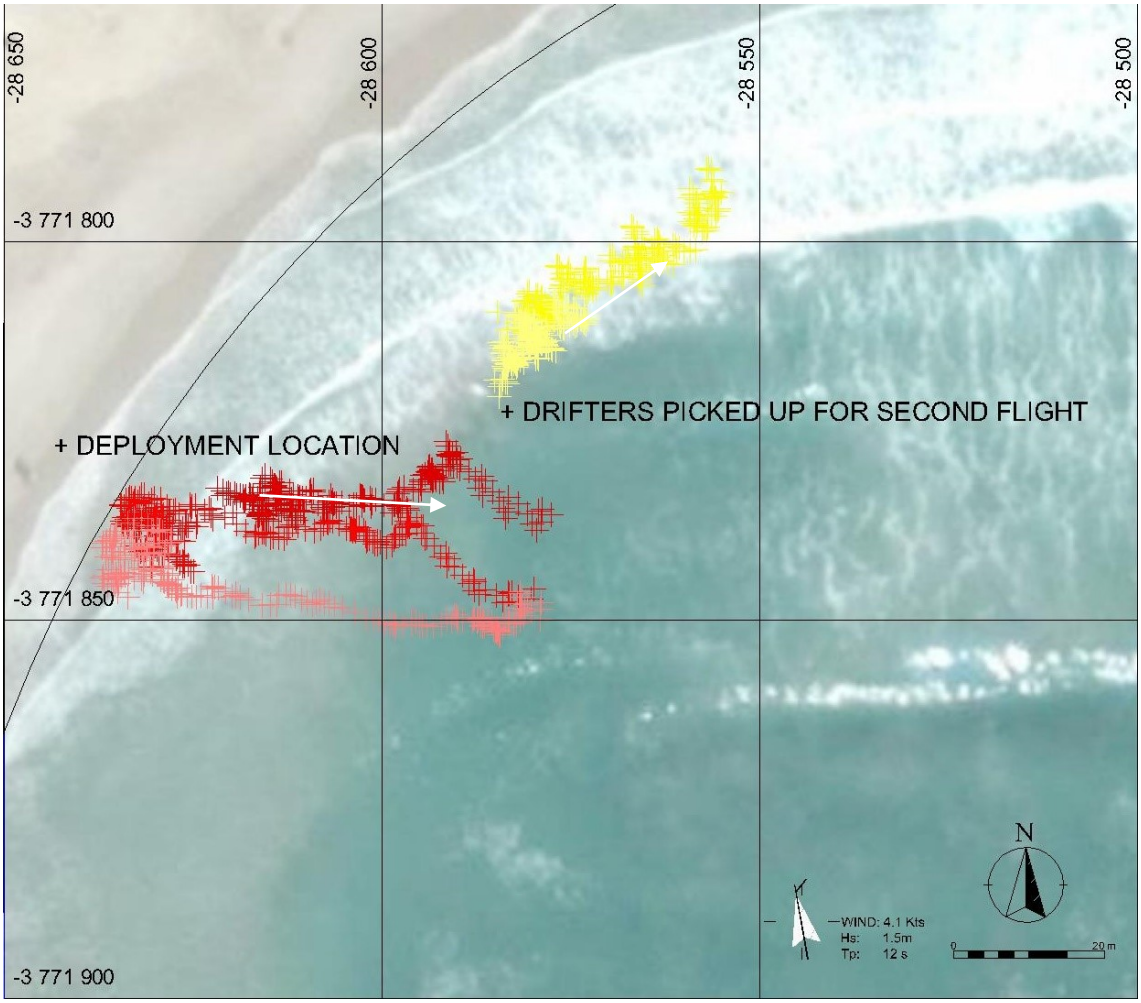

Figure 4-43: Flight FE Drifter Paths

The final test conditions corresponded to the test condition MB610 where Kistner estimated a U_{PA30} velocity of 30.2 cm.s^{-1} longshore towards the spur near the launch point at the beach, and a current of 32.1 cm.s^{-1}, still anti-clockwise at the north of the bay (points I & K respectively in Figure 4-45 below). The overall velocity exceedance profile was similar to that of Kistner's model as seen in Figure 4-44.

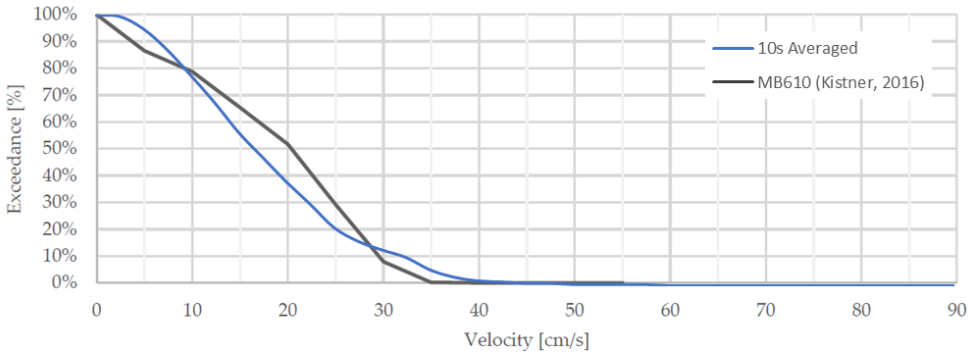

Figure 4-44: FE – MB610 Velocity Exceedance Comparison

The drifter paths however, showed a U_{PA30} rip current of 47 cm.s^{-1} off the beach and then a clockwise longshore current of approximately U_{PA30} 11 cm.s^{-1}, as shown in Figure 4-45.

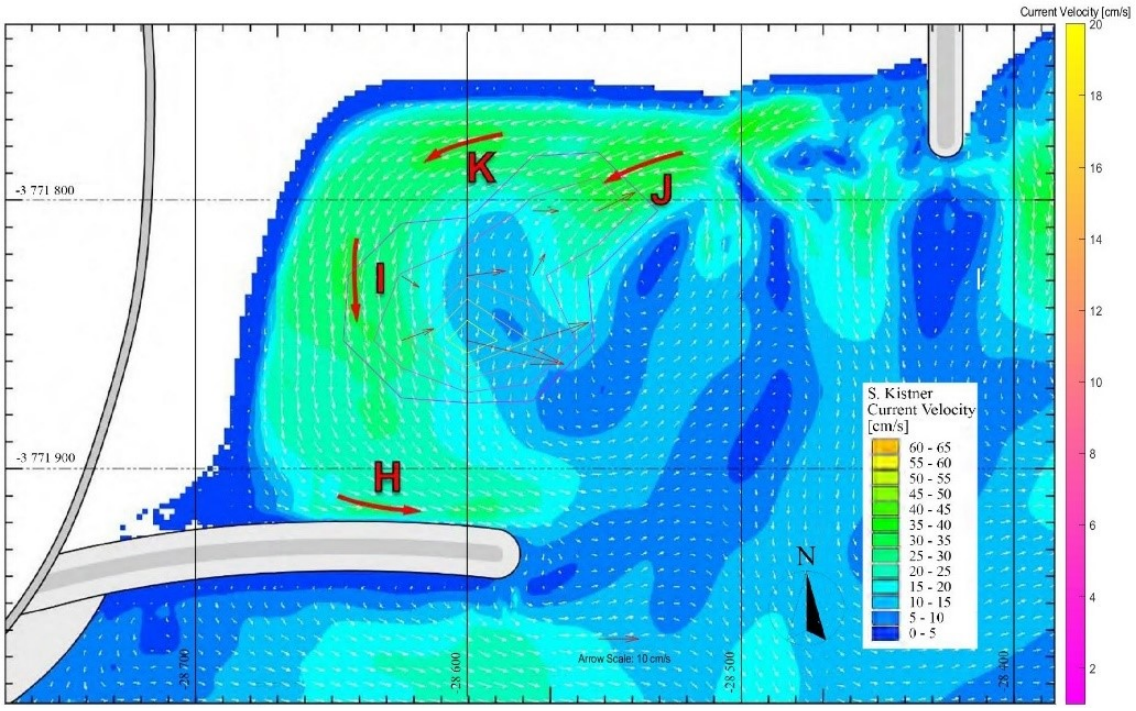

Figure 4-45: FE - Comparison of U_{PA30} Results

The 10 seconds averaged current velocities indicated an average of 18 cm.s^{-1} with a maximum of 58 cm.s^{-1}, as seen in Figure 4-46.

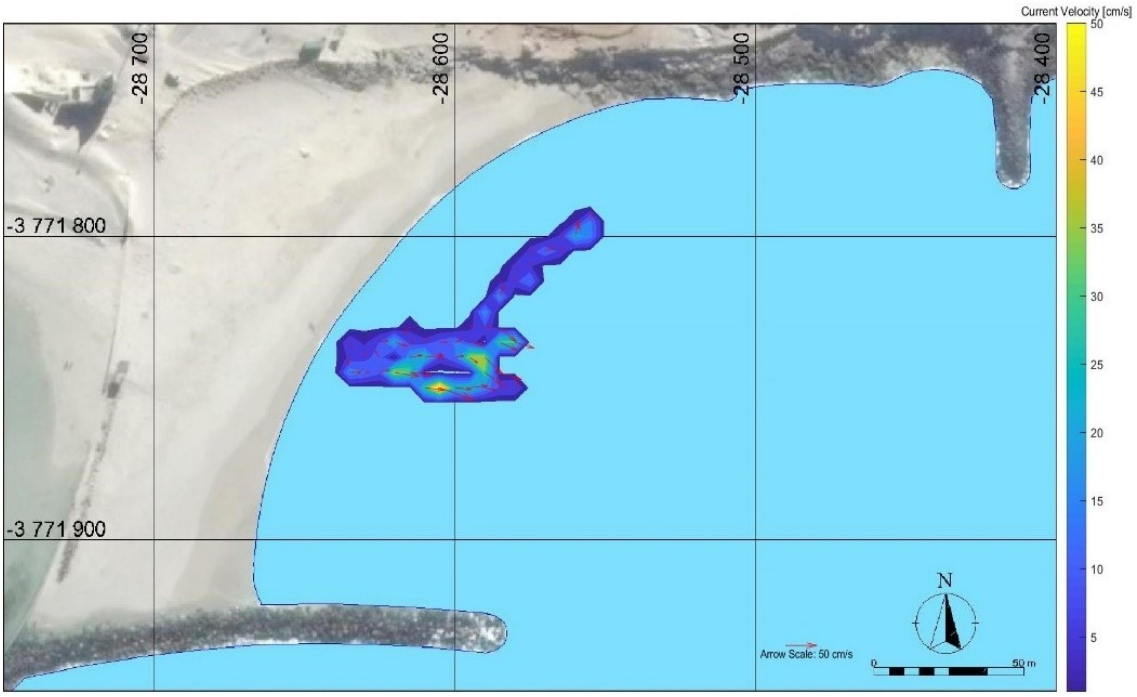

Figure 4-46: FE – 10 Seconds Averaged Current Velocities

4.3.1.6 Data Set FF

During collection for data set FF, 1455 drifter positions were collected over three flights. Drifters were launched from the beach for the first two then as these drifters moved towards the head of the spur, the third flight found one of these drifters to get measurements further in the bay (see Figure 4-47). The longest drifter path during the test was approximately 60 m from its launch position after 7 minutes.

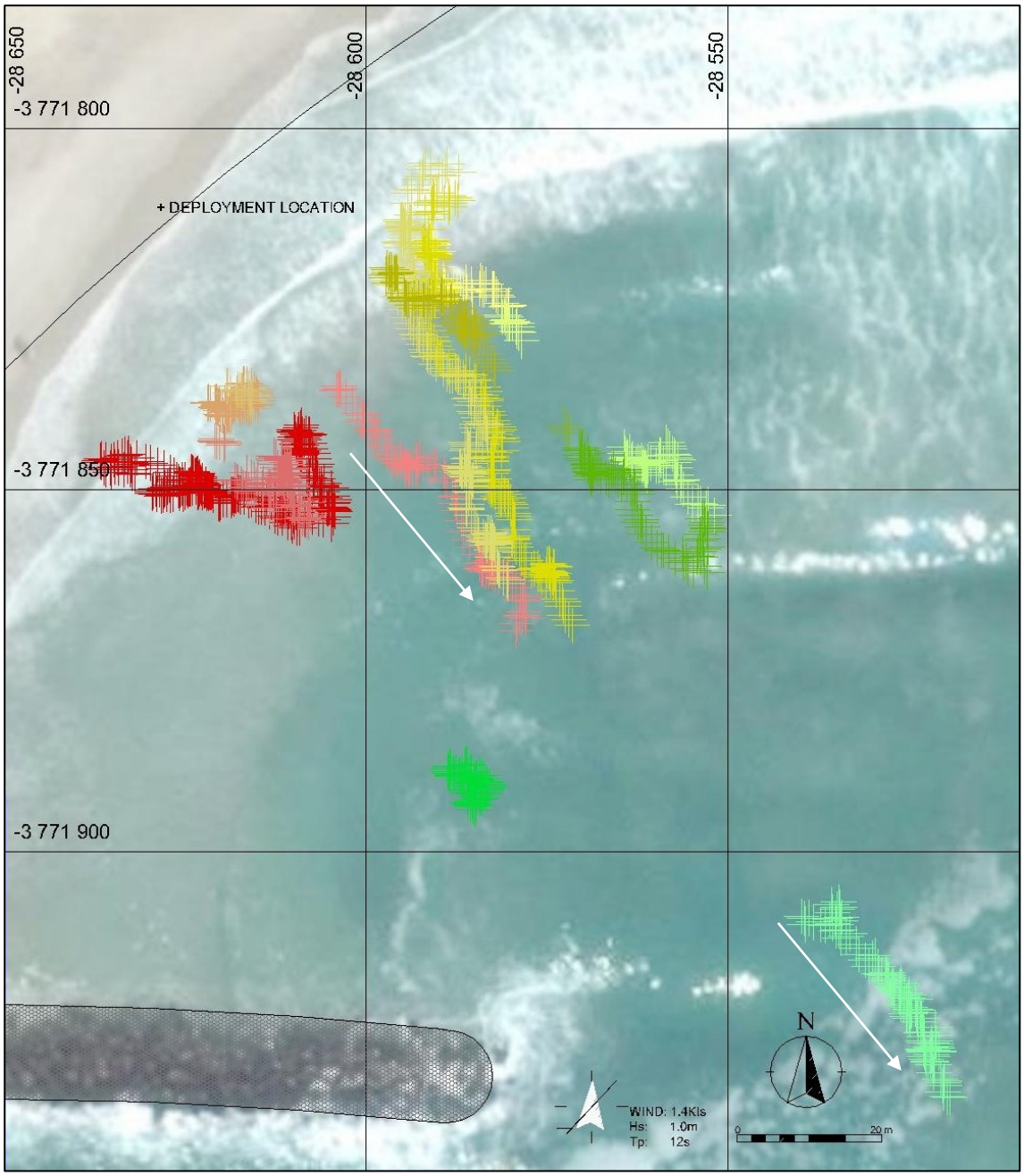

Figure 4-47: Flight FF Drifter Paths

The wave and tides during the test again most closely resembled those of Kistner's MB210 test and the U_{PA30} currents measured at points H and K were 26 cm.s^{-1} and 25 cm.s^{-1} respectively which were higher than the model results at 15.2 cm.s^{-1} and 21.9 cm.s^{-1}. This could be due to the slightly higher tides during testing which leads to an overall increase in the current exceedance profile, as seen in Figure 4-48.

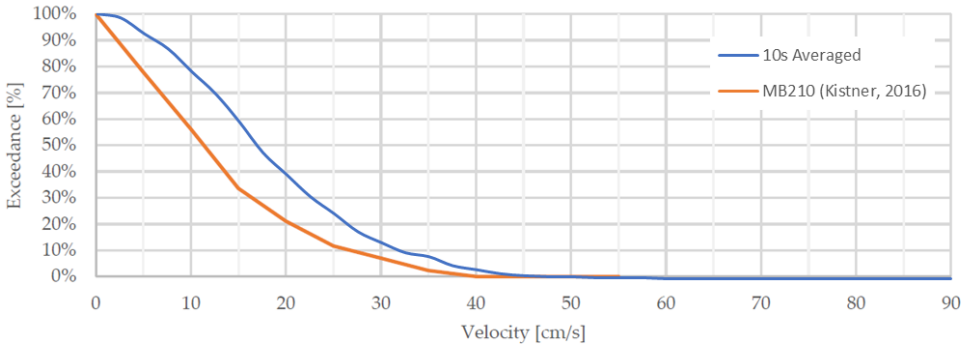

Figure 4-48: FF – MB210 Velocity Exceedance Comparison

However, it seems that there may be more of a sheltered zone behind the spur diverting the current I from Kistner's model slightly offshore which was reported as 26 cm.s^{-1} as the drifter path was measured right through the centre of the model's circulation cell within the bay, as seen in Figure 4-49 below. Another possible reason for the difference in current patterns behind the spur could be the recent construction of a HDPE seawater brine intake pipeline and brine outfall in the sheltered zone approximately 20 m behind the spur.

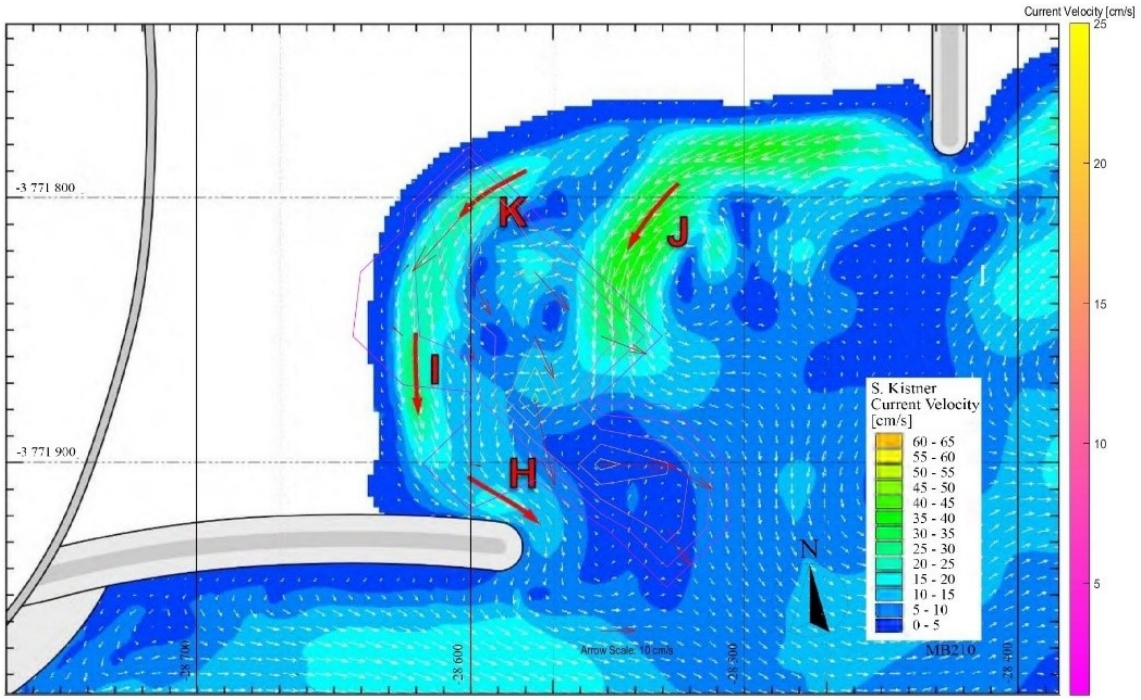

Figure 4-49: FF - Comparison of U_{PA30} Results

The 10 seconds average results, shown in Figure 4-50, gave a maximum current velocity of 58 cm.s^{-1} with the average being 19 cm.s^{-1} in the middle of the bay decreasing to 14 cm.s^{-1} off the end of the spur.

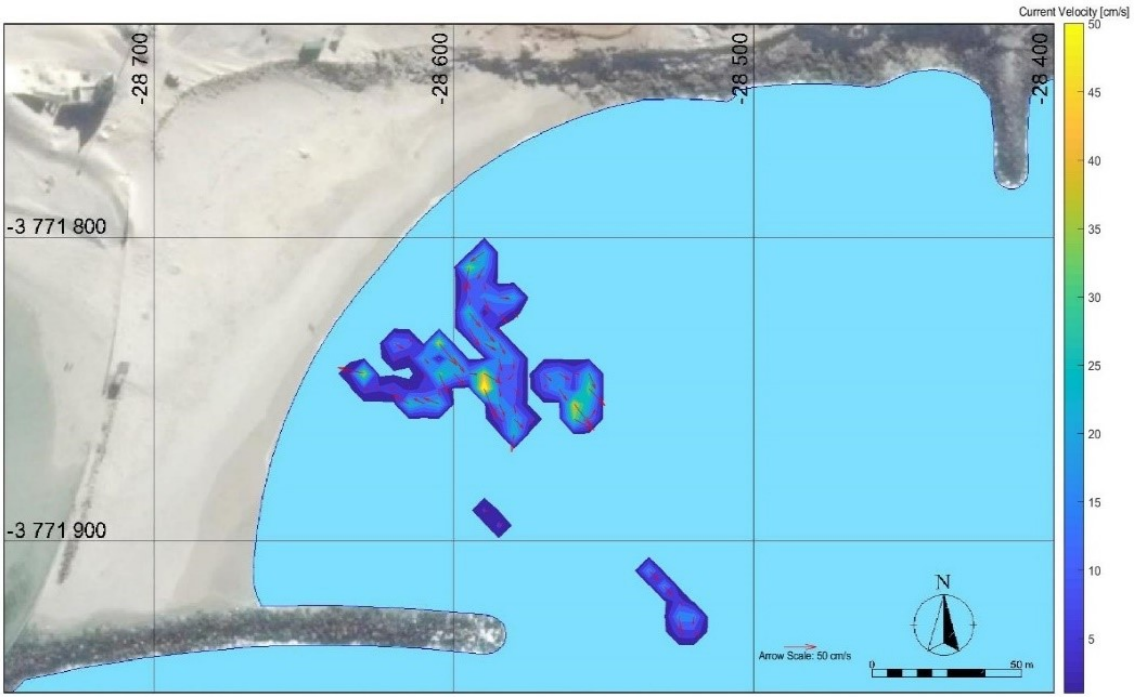

Figure 4-50: FF – 10 Seconds Averaged Current Velocities

4.3.1.7 Data Set FG

No current results were measured during tests on this day as the wind speed was too high for the drone to fly.

4.3.1.8 Data Set FH

Test FH indicated considerable drifter movement with the drifters moving an average of 60 m during each 10-minute-long flight from the beach longshore towards the head of the spur (see Figure 4-51). Due to the high degree of movement, the drifters dispersed, and it was difficult to follow all of them with the drone simultaneously. At times one or two of the drifters would move out of the frame and therefore were not tracked.

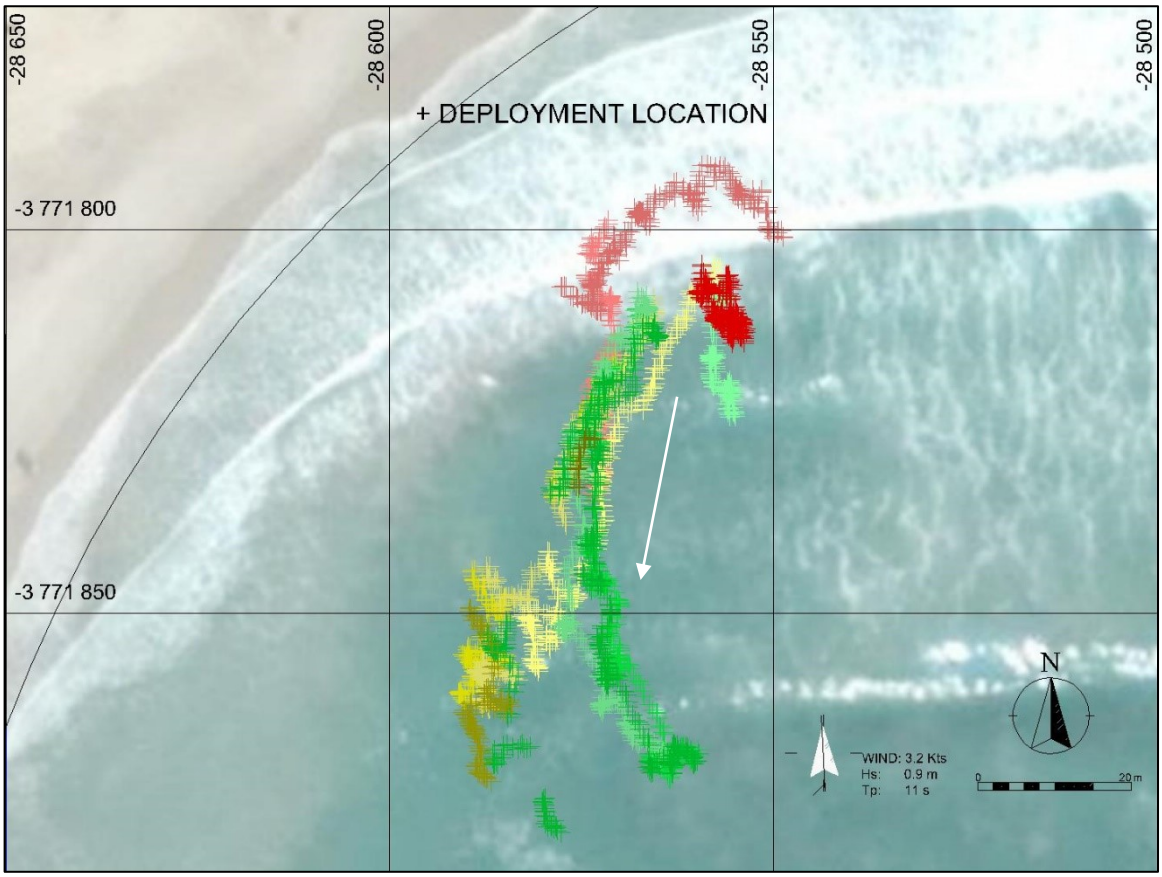

Figure 4-51: Flight FH Drifter Paths

The sea conditions corresponded to the Kistner's test condition MB210 where the estimated U_{PA30} velocity was 21.9 cm.s^{-1} longshore near the beach towards the spur, and a rip current of 38.2 cm.s^{-1}. The velocity exceedance profile, shown in Figure 4-52, correlates between Kistner's model results for MB210 and the drone measurements.

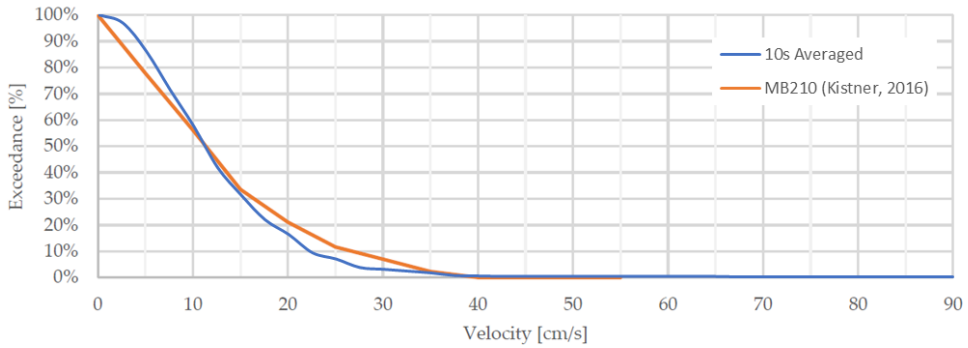

Figure 4-52: FH – MB210 Velocity Exceedance Comparison

The drifters showed a U_{PA30} longshore current of 13 cm.s^{-1}; however, there was not enough resolution to resolve the second rip current near the deployment location, as shown in Figure 4-53. It also seems that at this resolution, the 25 by 25 m grid size for resolving U_{PA30} current velocity included a large number of wave oscillations which reduced the average current magnitude.

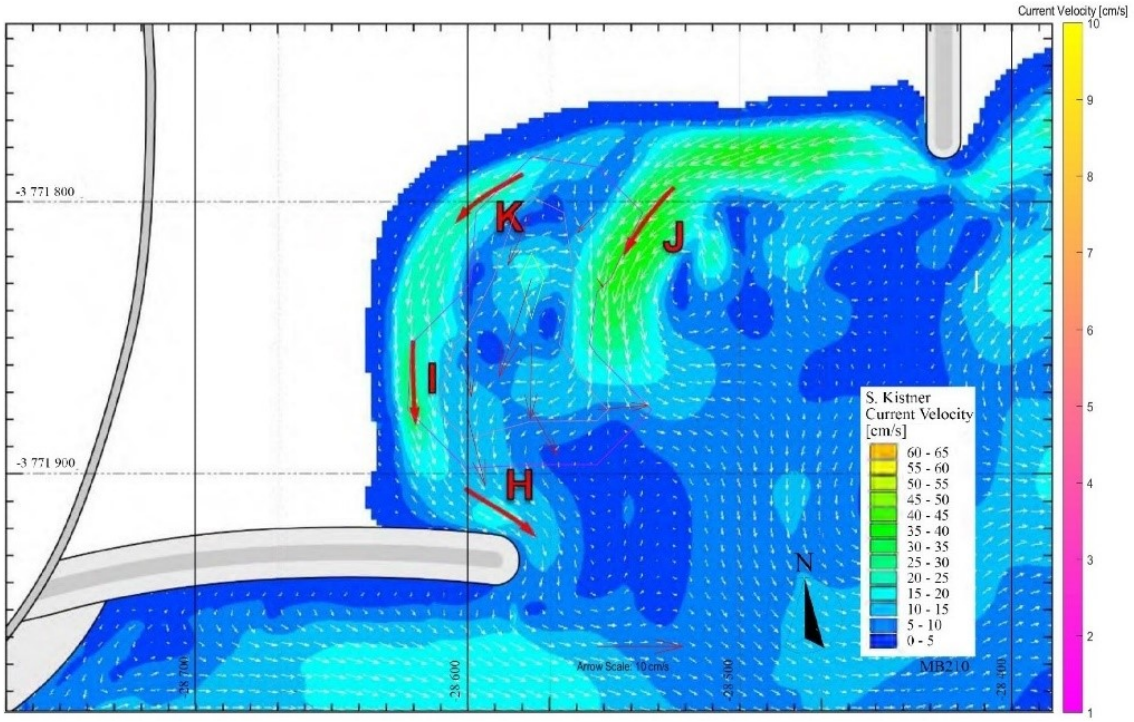

Figure 4-53: FH – Comparison of U_{PA30} Results

The 10 seconds averaged plot (see Figure 4-54) shows a better representation of the current path along the beach towards the spur with a maximum velocity of 66 cm.s^{-1} and an average current velocity over the domain of 12 cm.s^{-1}. This test shows the expected anti-clockwise circulation pattern in the bay within the sheltered area behind the spur.

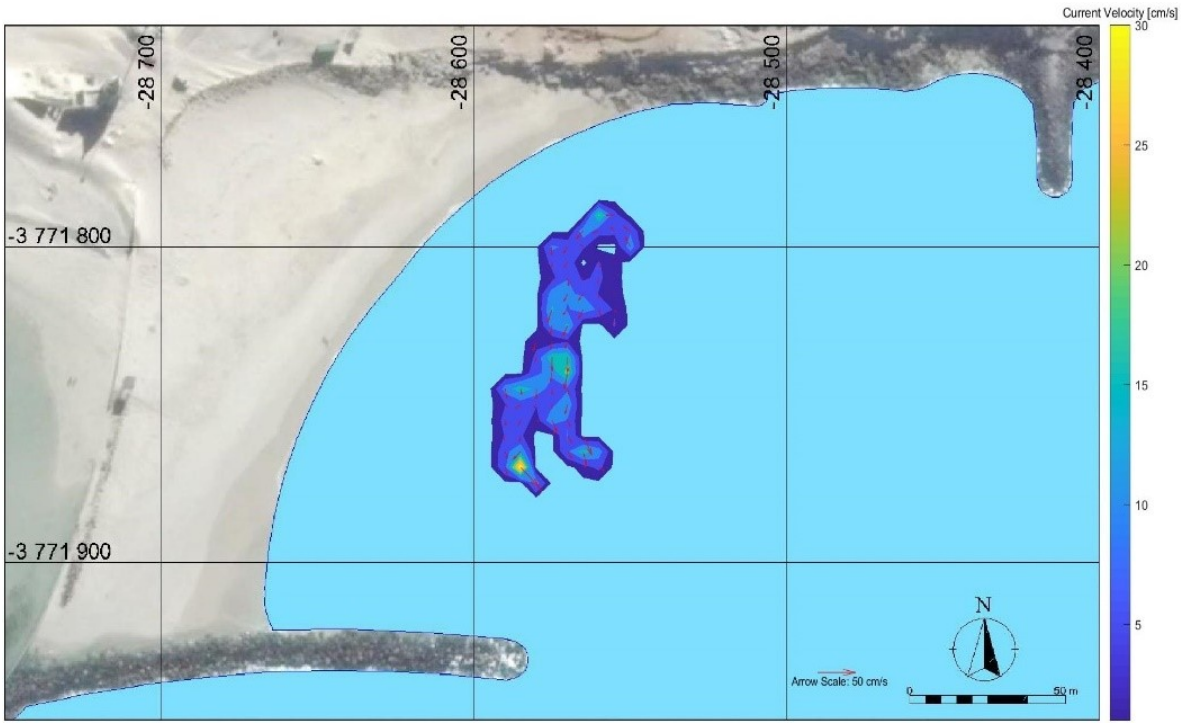

Figure 4-54: FH – 10 Seconds Averaged Current Velocities

4.3.1.9 Trip FI

During collection of this data set, the DJI Inspire 2 drone was used in order to collect some comparison measurements which have been elaborated on in section 4.3.2 below. The currents below were calculated only using the 4353 drifter points collected by the Mavic Air over three flights with the longest drifter path (ending closest to the spur in Figure 4-55 below) being 150 m over 11 minutes, although there was a period where the drifter was out of the frame and was picked up again later in the flight. The longest continuous track was just shy of this at 130 m over 8 minutes.

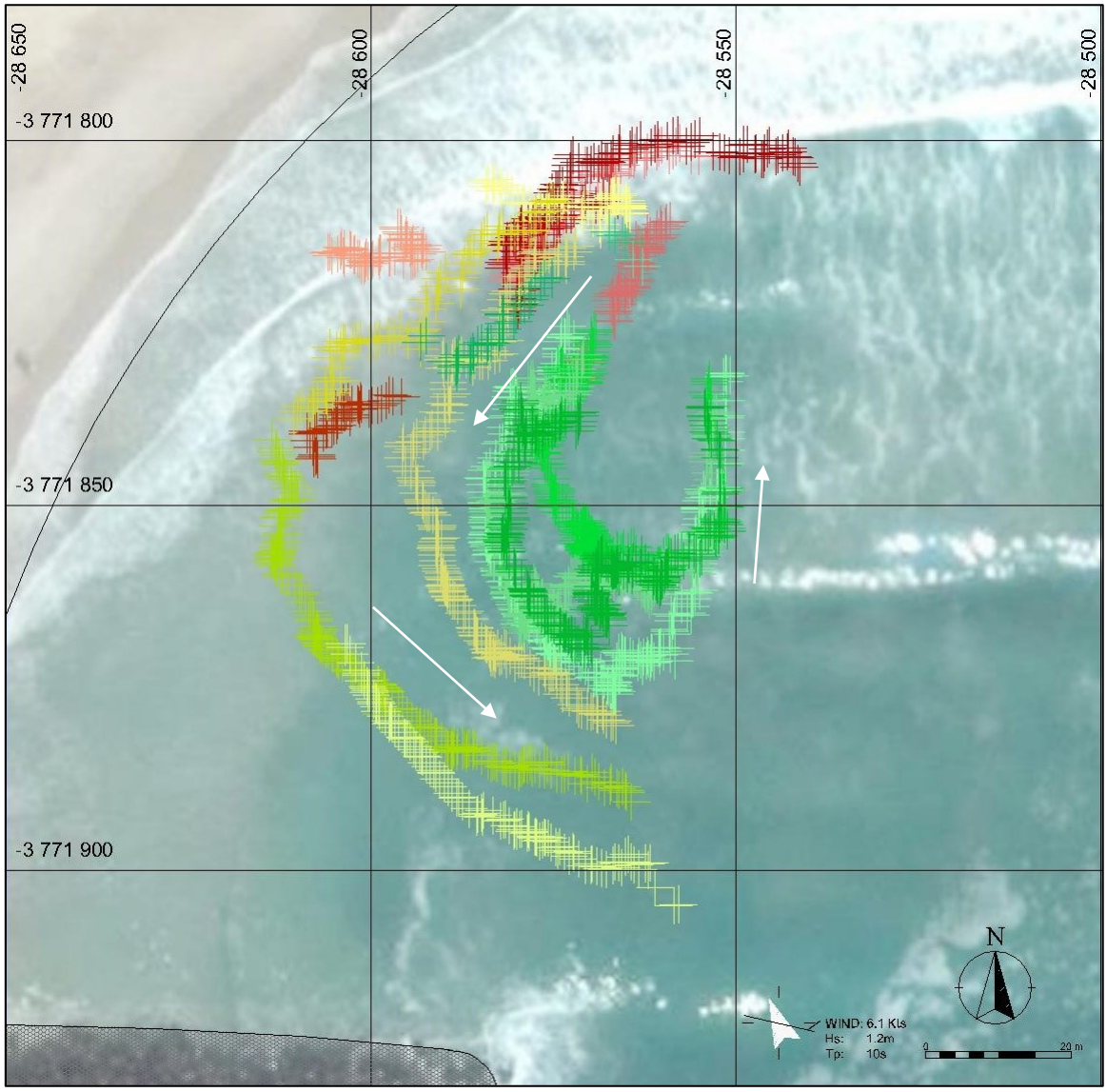

Figure 4-55: Flight FI Drifter Paths

The conditions again matched Kistner's MB210 model and the current pattern also showed the anticlockwise path around the bay (see Figure 4-57). There was a return current noticed in the opposite direction to that of point J in the model results which could be due to waves coming into the bay pushing the drifters as they go past the spur. This test allowed for a comparison to all points extracted from the model shown in Table 4-4 below.

Table 4-4: Test FI vs MB210 U_{PA30} Velocity Results

	Model Velocity Results [cm.s^{-1}]	Measured Velocity Results [cm.s^{-1}]
$U_{(H)}$	27	15.2
$U_{(I)}$	21	26
$U_{(J)}$	-28	38.2
$U_{(K)}$	26	21.9

The velocity exceedance profile for the measurements are approximately 50% higher than that reported by Kistner. This is possibly due to a slightly higher wave height and tide allowing for more wave energy to penetrate into the bay and set up a strong anti-clockwise circulation cell behind the spur. Surfing effects of the drifters returning back at point J may also lead to higher average current measurements.

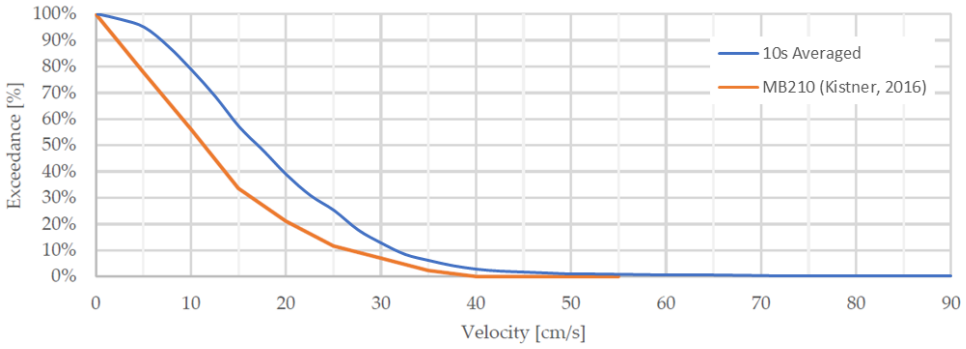

Figure 4-56: FI – MB210 Velocity Exceedance Comparison

Most results align closely with the model apart from point J which may be the model resolving an undertow; while the drifters were carried in by surface current driven by waves coming into the bay.

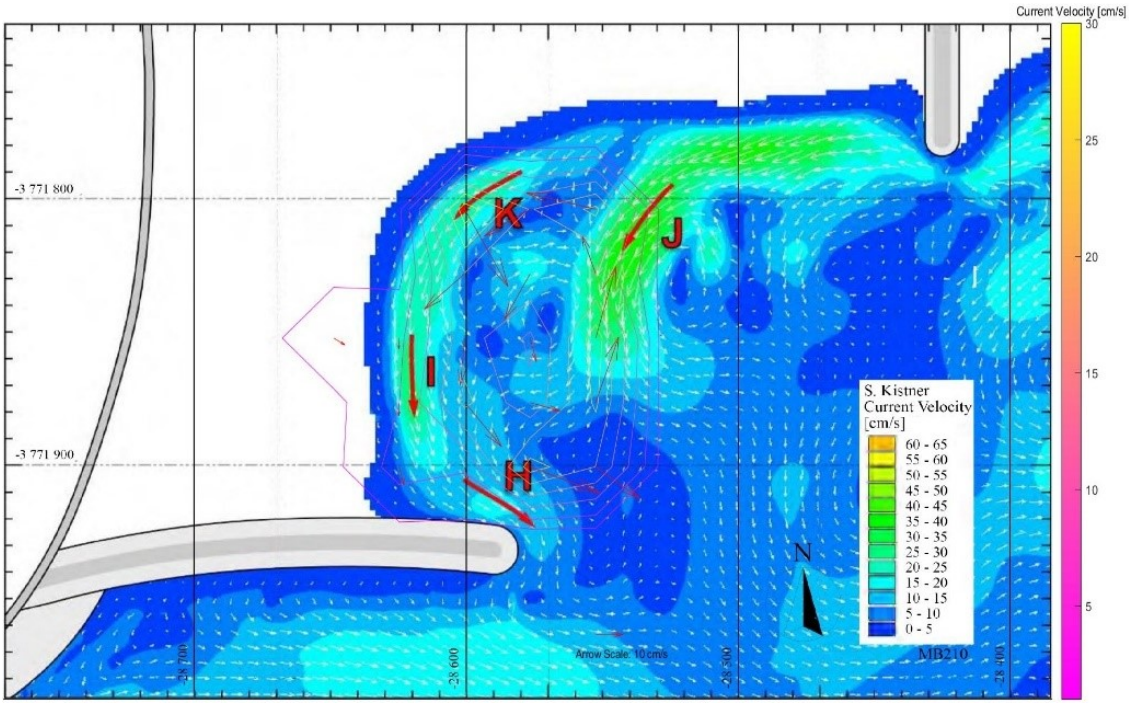

Figure 4-57: FI - Comparison of U_{PA30} Results

The 10 second averaged results shown in Figure 4-58 below has a good spread over the bay giving a good resolution of the current patterns. The maximum velocity was found to the east of the results with a current velocity of 67 cm.s^{-1} towards the beach, most likely due to surfing effects. Behind the spur the maximum current velocity was 47 cm.s^{-1} towards the head of the spur with an overall average velocity of 18 cm.s^{-1}.

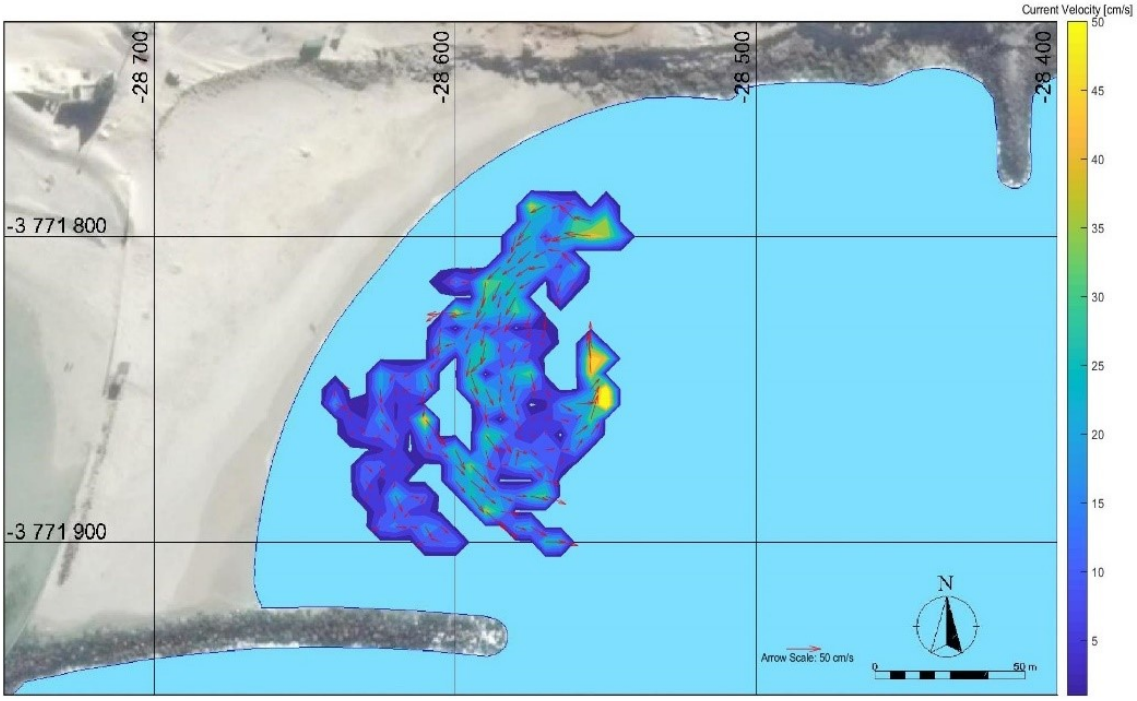

Figure 4-58: FI – 10 Second Averaged Current Velocities

4.3.1.10 Trip FJ

The last data collection set FJ focussed more on the calibration tests of the tape on the shore and the GCP's just behind the surf zone. Still the longest path, shown as blue in Figure 4-59, was approximately 50 m with some additional oscillations in the surf zone. During the third flight the drone was also sent further out to record some of the original drifters which had floated out into the centre of the bay. In total 2649 points were recorded.

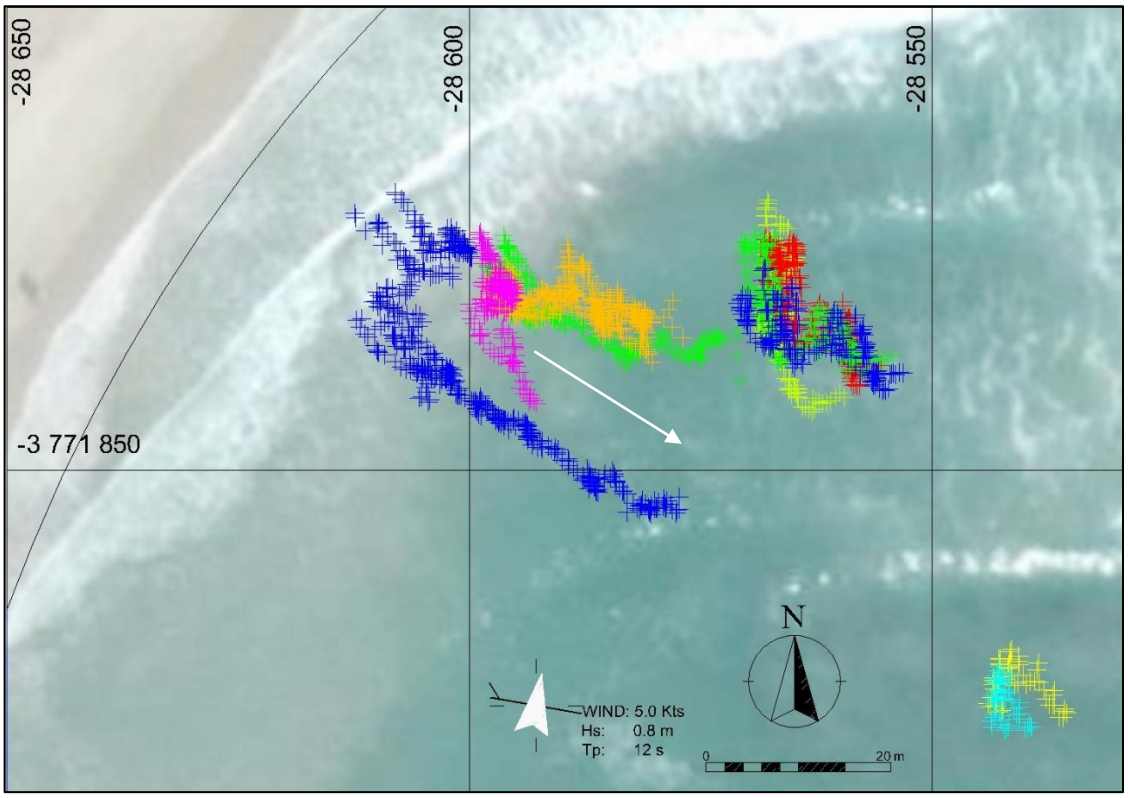

Figure 4-59: Flight FJ Drifter Paths

The sea conditions again corresponded to the Kistner's test condition MB210 where the longshore drift U_{PA30} at point I closer to the spur equalled to 26 cm.s^{-1} and a rip current velocity of 15.2 cm.s^{-1} was recorded at point H. This is highlighted by the velocity exceedance profile which is similar to that reported by Kistner, see Figure 4-60.

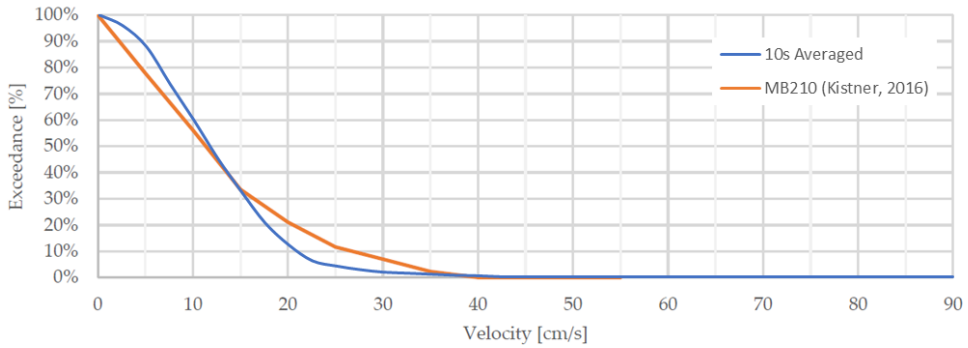

Figure 4-60: FJ – MB210 Velocity Exceedance Comparison

The drifters showed a U_{PA30} longshore current of 29 cm.s^{-1} near the beach, dropping to 5 cm.s^{-1} behind the spur, as shown in Figure 4-61. The drifter's path again appeared to go through the area of low currents seen in the model results indicating a slightly different pattern in the bay. In this case the drifter's path was into the wind indicating that it was not due to wind.

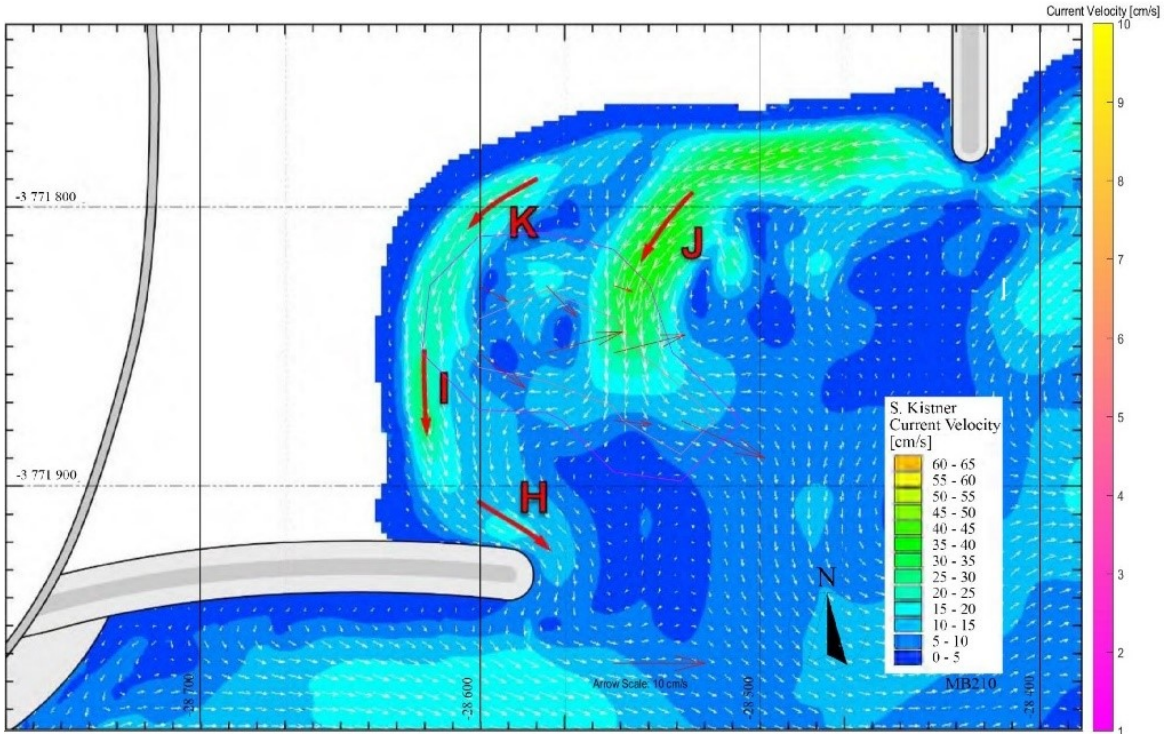

Figure 4-61: FJ – Comparison of U_{PA30} Results

The 10 second averaged plot, as represented in Figure 4-62 below, again shows a more detailed representation of the current path along the beach towards the spur with a maximum velocity of 42 $cm.s^{-1}$ and an average over the domain of 12 $cm.s^{-1}$. This test shows again shows the rip current flowing away from the beach behind the spur which at the time of this test was within the safe bathing area flags.

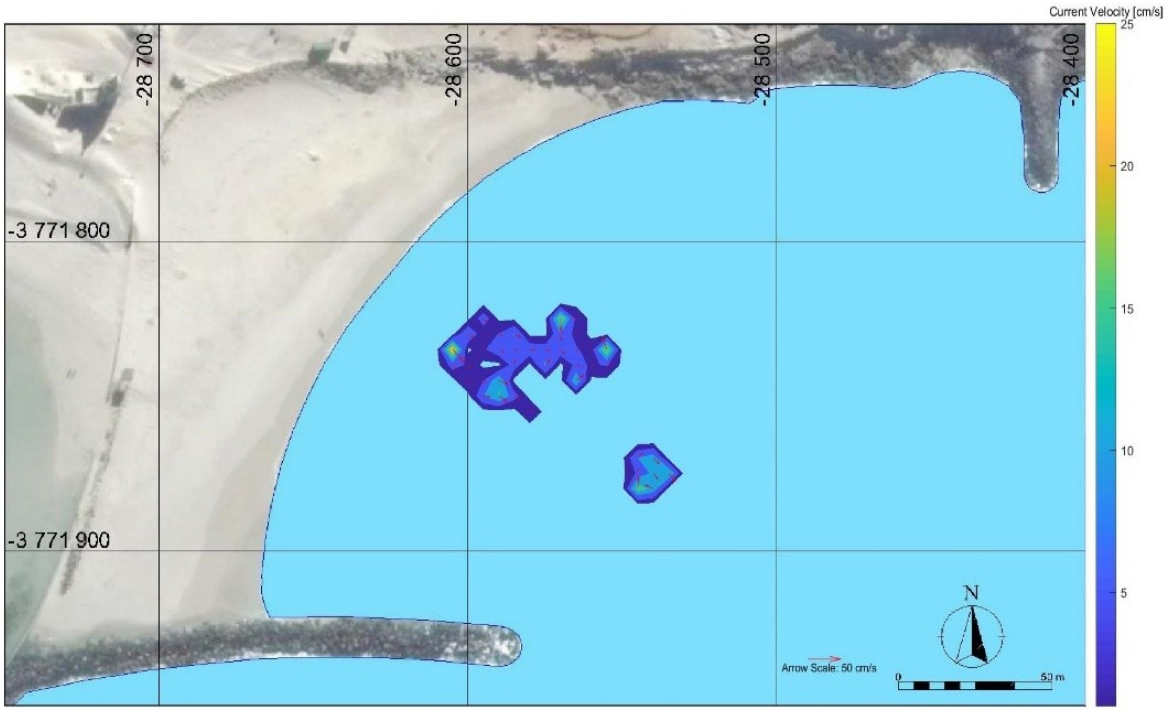

Figure 4-62: FJ – 10 Second Averaged Current Velocities

4.3.2 Inspire Comparison

Comparing the Inspire 2 directly with the Mavic Air proved difficult from the one test carried out as controlled conditions were not achieved, as seen in Figure 4-63 below. In the absence of a calibration test for the Inspire 2, a length was selected between two of the outfall pipelines concrete collars and a comparison was made between the Inspire 2 and the Mavic Air for calibration.

The Inspire 2 focal length factor *f* was kept at the reported 8.8 mm and the elevation correction factor of 5.5 m was selected in order to correctly scale the lengths measured from the Inspire 2, seen as yellow in Figure 4-63 below, and compared to those measured by the already calibrated Mavic Air. It was expected that the elevation correction factor would be higher than the Mavic Air as the drone was launched from higher up at the beach car park.

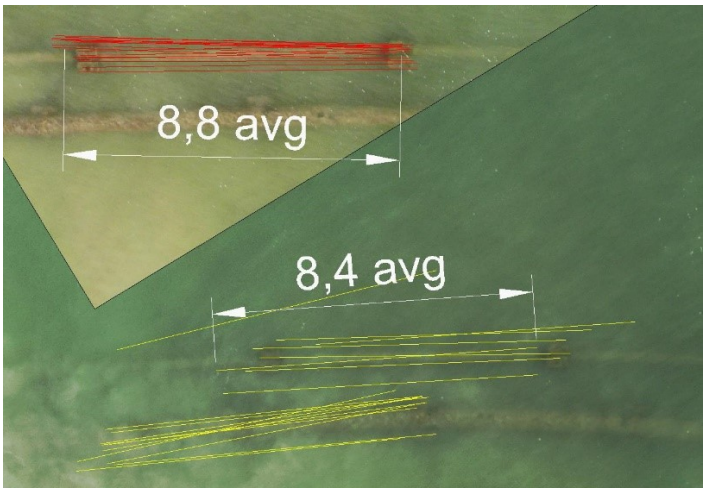

Figure 4-63: Comparison Pipe-Collar Length for Calibration – Mavic Air (red) vs Inspire 2 (yellow)

It was noted that the current velocity measurements by the Inspire 2 were on average higher than those measured by the Mavic Air over the same period, as indicated in Figure 4-64. Specifically, over the test period the average current velocity from the Inspire 2 was 63 cm.s^{-1} with a standard deviation of 47 cm.s^{-1} while the Mavic Air measured an average 37 cm.s^{-1} with a standard deviation of 23 cm.s^{-1}, a reduction of approximately 40%.

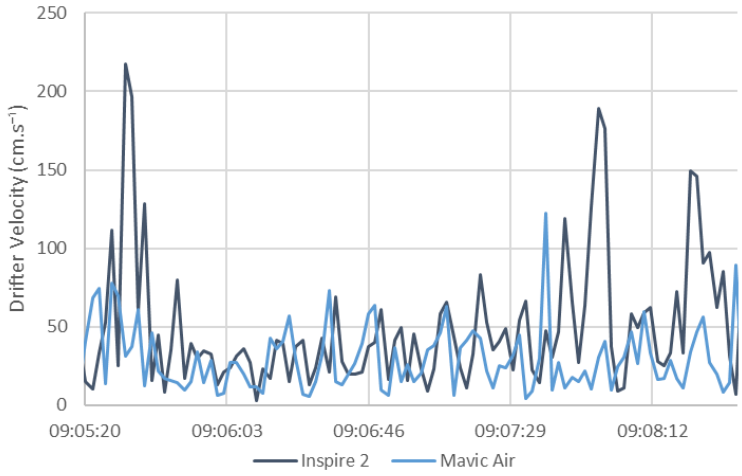

Figure 4-64: Extract Measured Current Velocity Comparison Between Inspire 2 and Mavic Air

It was suspected that the increased current velocity measurements by the Inspire 2 were pilot related as the Inspire 2 had an average horizontal speed of more than three times that of the Mavic Air (63 $cm.s^{-1}$ compared to 17 $cm.s^{-1}$) over the same period. By the time of this test the Mavic Air operator was already familiar with the technique of following the drifters and therefore was able to spend less time moving the drone to keep the drifters in frame. The Inspire 2 operator struggled and was noted to track around more in an attempt to follow the drifters. This led to a higher average drone horizontal speed. It should be noted that the average horizontal position of the Mavic Air during the first test FA was 200 $cm.s^{-1}$ when tracking the drifters. This horizontal velocity quickly dropped to between 10 and 20 $cm.s^{-1}$ for subsequent tests once the operator was more aware of how to track the drifters and what to look for. A larger, brighter display, instead of the cellular phones used, may also assist in picking out the drifters.

Figure 4-65 below, shows the differences between the measurements from the Inspire 2 (positive values) and the Mavic Air (negative values) and highlights that most of the measurements were in the upper right corner where the Inspire 2 has both the larger velocity and the larger current measurement. This error could be introduced as the DJI platform tried to recalibrate its anticipated location based on both the GPS, which has its own built in error, as well as the downward facing sensors which are included to improve the hovering accuracy but may confuse the system over water.

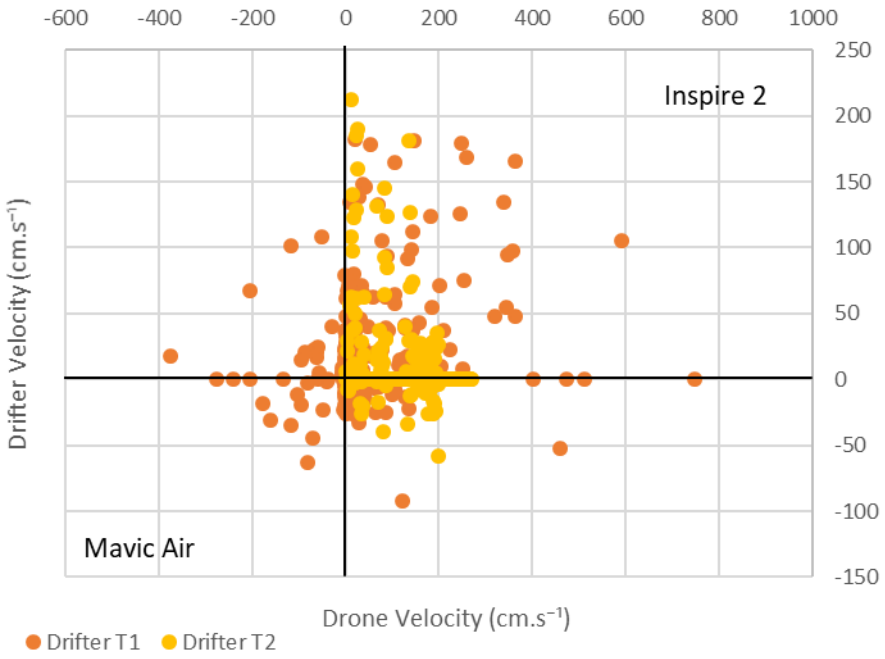

Figure 4-65: Drifter vs Drone Velocity Comparison

As the horizontal displacement of the drone moved past a threshold the drone relied on the GPS data. Any GPS error accumulated during the period when the drone relied on the downward visual sensors was then introduced, causing higher displacement errors in the coordinate measurements. This is shown in Figure 4-63 above where the yellow lines were more spread out as the Inspire 2 moved around more than the Mavic Air which remained more stationary. Tests of similar DJI systems over water, such as the one carried out by Ricker (2017), show that there were some interaction between

the sensors over water and further testing would need to be carried out to quantify this. It should be noted, that the latest DJI Phantom RTK should reduce this error by vastly improving the GPS accuracy.

A test where both drones remain stationary would be better suited to more accurately evaluate and compare the two drones than one where the drifters were followed, especially with a pilot who is not familiar with tracking drifters.

4.3.3 Horizontal Current Velocity Distribution

On clear days it was possible to see the sediments suspended below the drifters as they were tracked. This gave a good indication of the currents below the drifter which typically moved along with the drifters at a similar velocity, as seen in Figure 4-66 below, and reinforced the assumption set out in Section 2.2.2 that the surface currents were a good approximation for the entire water column.

Figure 4-66: Drifter Tracking Along with Suspended Sediments

4.3.4 Notable Surface Features

During testing, objects were often noticed floating along with the drifters. Further investigations could do away with the artificial drifters and, with the aid of computer vision, using object such as surface debris (e.g. sea foam, driftwood and plastic) as can be seen in Figure 4-67 below. Suspended sediment could also be used to measure the currents below the drone like the method of using dye tracers.

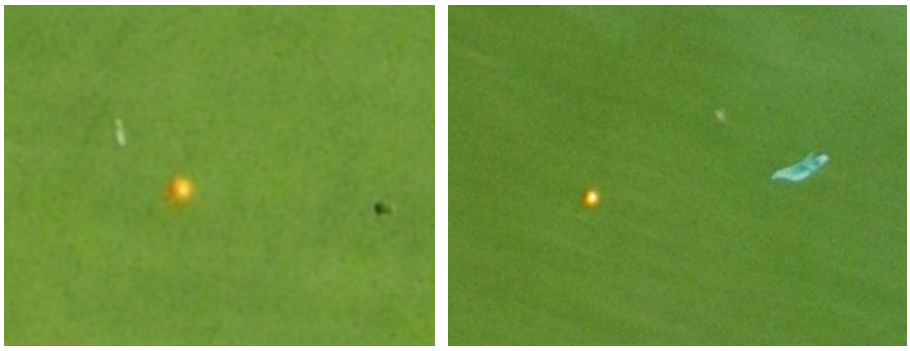

Figure 4-67: Examples of Debris Noted During Tests

Colour manipulation can further assist in identifying drifters. The image on the left of Figure 4-68 is the centre image with a filter that cuts out the spectra of light which do not correlate to the oranges used as drifters. On the right a similar filter was used which has desaturated all colours apart from

the orange collar of the drifters. Similar techniques could be used to simplify processing the images and possibly even pick out drifters through surface foam and debris, especially if infra-red camera technology is utilised.

Figure 4-68: Computer Aided Colour Manipulation

4.4 Monwabisi Study Current Result Comparison Conclusions

On average there was a 50% reduction in the currents measured compared to those at the extracted points from Kistner's Model output, which is not unreasonable as the model was not originally calibrated. There were some results in opposing directions, shown as red results in Table 4-5, and these corresponded to reductions of up to -255% but may be due to surfing effects which skew the measured results.

Table 4-5: Comparison Results Summary

	Measured Velocity Results [cm.s^{-1}]				Kistner	Model Velocity Results [cm.s^{-1}]			
	$U_{(H)}$	$U_{(I)}$	$U_{(J)}$	$U_{(K)}$		$U_{(H)}$	$U_{(I)}$	$U_{(J)}$	$U_{(K)}$
FA		31			**MB110**		21.2		
FB		-5			**MB210**		26		
FC		6			**MB430**		28.8		
FD		20	27		**MB420**		30.9	37.3	
FE		-47		-11	**MB610**		30.4		32.1
FF	26			25	**MB210**	15.2			21.9
FH				13	**MB210**				29.1
FI	27	21	-28	26	**MB210**	15.2	26	38.2	21.9
FJ	5	29			**MB210**	15.2	26		

The remaining results which align with Kistner's modelled directions are in line with the expected current velocities considering that the drifter may not have taken the path of peak velocity as extracted from the model. This is illustrated by Figure 4-69 which shows the velocity exceedance comparison to MB210 where tests FB, FH and FJ show a very similar exceedance profile to the model results and the remaining two tests which are 50% higher possibly due to stronger circulation pattern than that generated by the model due to a higher waves or lower tide experienced during the test.

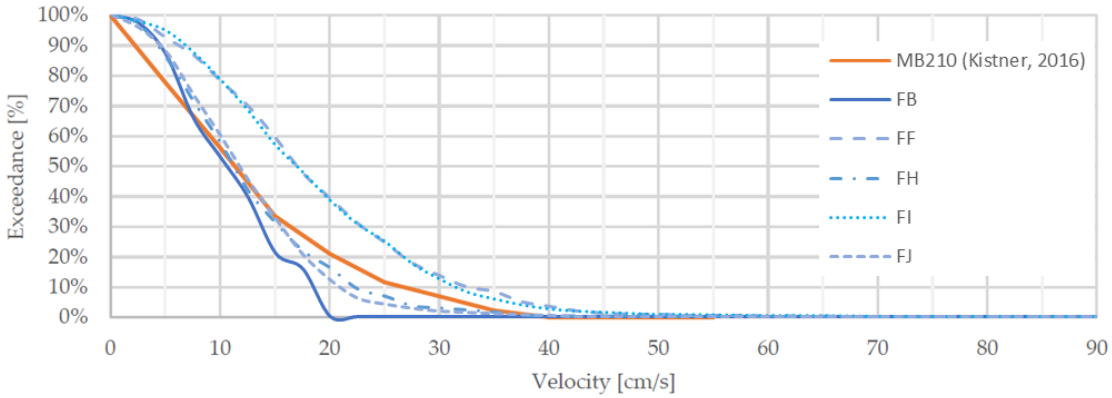

Figure 4-69: Combined MB210 Comparison Velocity Exceedance Results

It was noted that the current pattern did not always correlate well with Kistner's model results. Many drifter measurements illustrated a rip path running from the corner of the bay straight out towards the head of the spur, which was different to the models shore perpendicular pattern as well as a return current in an opposite direction to the offshore rip J, as seen in Figure 4-70. The drifter measurements at this point were more in line with the original current pattern proposed by Theron & Schoonees (2017), (refer to Figure 2-13 on page 14 above). This may be due to a difference between surface currents and overall currents, possibly due to wind or wave surfing effects and may be a possible aspect for further study.

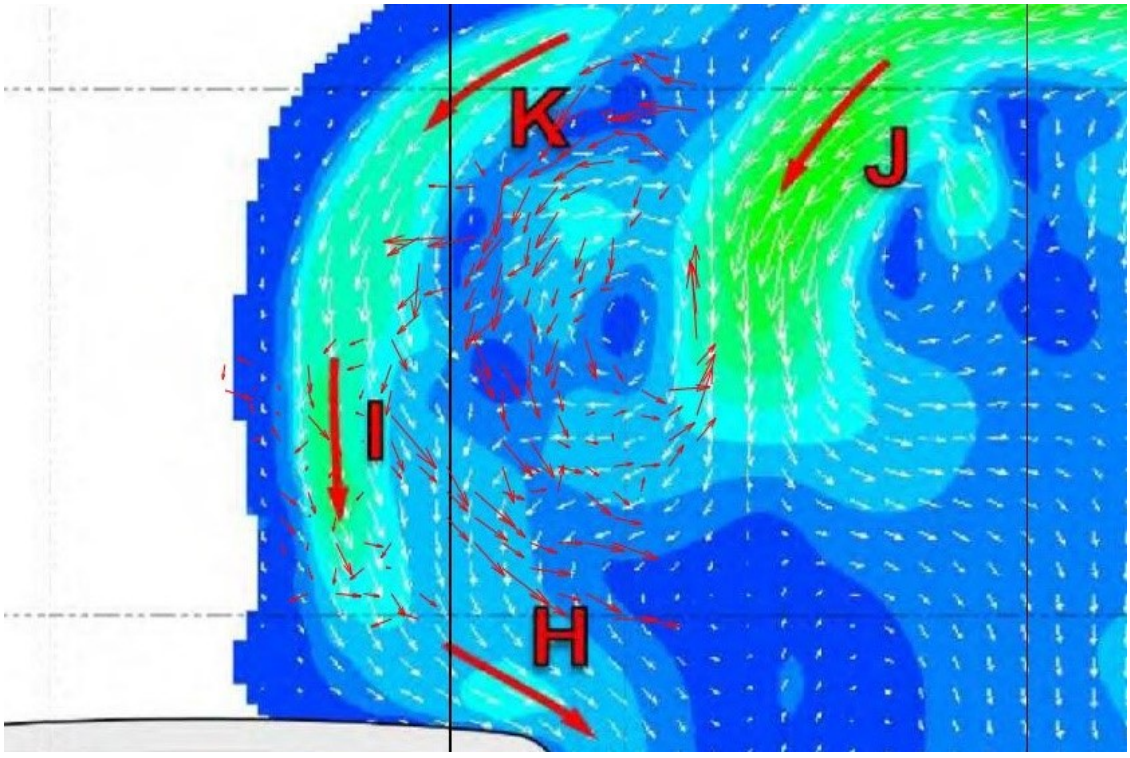

Figure 4-70: Test FI Velocity Vectors Superimposed over Current Designation Areas per Kistner (2016)

4.4.1 Monwabisi Bathy

One possible cause for this differing current patterns within the bay may be sea-bed profile which was tested by Kistner differing from the current bathymetry. An obvious difference is the desalination intake 630 OD HDPE seawater intake pipeline, 355 OD HDPE brine outfall pipeline and concrete weight collars which was installed in 2018, see Figure 4-71.

Figure 4-71: Monwabisi Desalination Pipelines

This structure may be causing a build-up of sediment between the pipelines and spur, making the area shallower. This would drive currents out into the bay along the pipeline, as seen in Figure 4-72, rather than along the breakwater as found in Kistner's results. Hence, a lower current would be found at point H which Kistner extracted from the model, and a higher current would be found further in the bay, as seen in Figure 4-70 above.

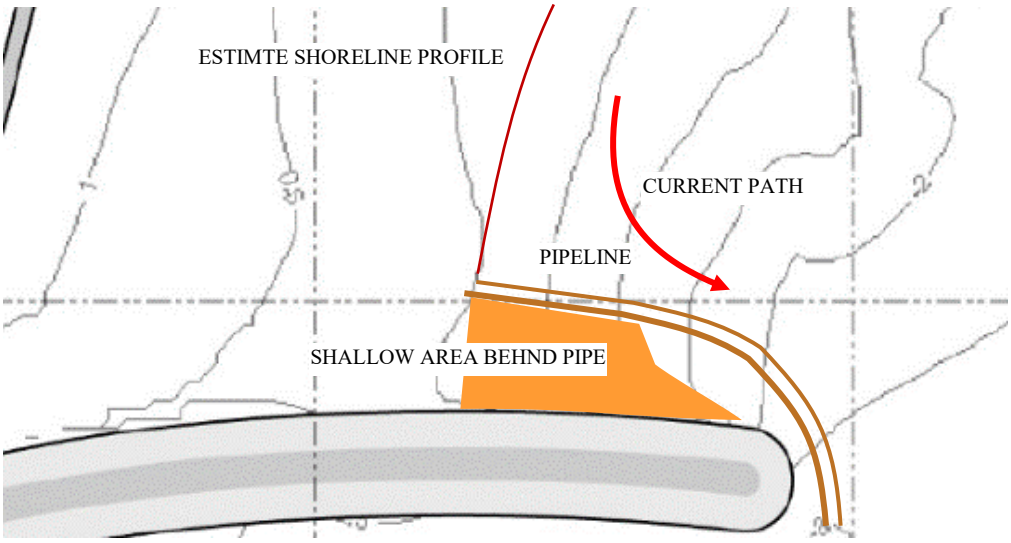

Figure 4-72: Pipeline Bathymetry Changes to Kistner Model Tests

4.5 Other Interesting Observations

Over and above measuring currents, there are numerous applications for drones in the coastal engineering field. During this study the following additional observations were made which could prove to be drone applications in the future.

4.5.1 Underwater Features

If the water was clear enough at the time of collection, underwater features such as rocky outcrops, seen in Figure 4-73 below, could serve as GCP's when the drone was over water. Image recognition algorithms would easily be able to pick up these features between frames and track them in order to provide an error estimate. The image recognition software should be able to find and track the drifter on the water which would be a better than the manual AutoCAD solution utilised in this thesis.

Figure 4-73: Rocky Reef within Monwabisi Bay Seen from Above

Another feature visible on clear days was the movement of sediment which showed both the path of the current, explored in section 4.3.2 above, as well as the actual sediment picked up clearly seen in Figure 4-74. Again, a computer vision algorithm would likely be able to be trained to estimate the sediment movement from these aerial photographs.

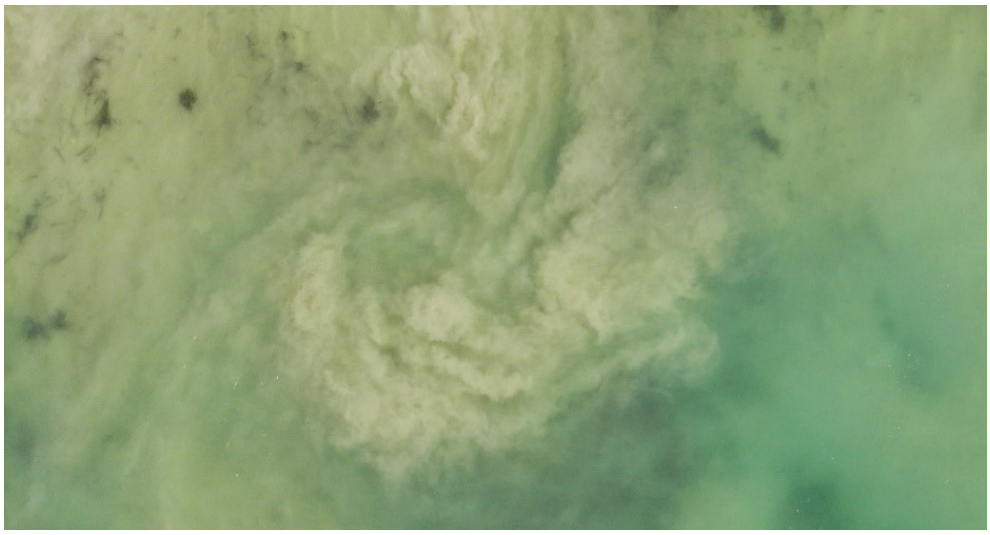

Figure 4-74: Sediment Movement Visible from Above

4.5.2 Outfall Monitoring

A marine brine outfall was installed during the study. On one occasion it was possible to observe the red tinge of the brine outfall due to the presence of ferric hydroxide, as seen in Figure 4-75, which is a by-product of desalination pre-treatment (Watereuse Association, 2011). This would provide a good method for confirming the actual effluent dilutions of the outfall using the gradient between the red brine and the blue sea surface as proposed by Le Roux (2018). For effluent discharges with a heat differential to the surrounding ambient sea temperature, a thermal camera fitted to the drone would be able to "see" the heat dispersion of the outfall and could possibly map dilutions based on temperature variation.

Figure 4-75: Brine Outfall from Above

4.5.3 Marine Life Monitoring

During testing there were points at which marine life crossed through the field of study and could clearly be seen, such as the school of fish (left) as well as a seal (right) in Figure 4-76. This shows the possible use of drones for monitoring marine life, their interactions with both beachgoers, such as shark spotters, or possibly to monitor any impact of coastal construction works.

Figure 4-76: Marine Life Seen During Testing

4.5.4 Algal Bloom

During one flight looking out towards False Bay it was noted that there was a discoloured patch in front of Strandfontein Tidal Pool which was suspected to be a cloud of diatoms (see Figure 4-77) which is often seen in the bay (Kruger & Wilson, 2010). Similar images can be used to monitor seawater intakes which are susceptible to blocking, such as for desalination, and assist reduced pump flow when turbidity is high.

Figure 4-77: Drone View of Suspected False Bay Diatom Cloud

4.5.5 Additional Observation Conclusions

Drones are ideal tools to solve niche problems which are often encountered specific to the coastal and marine environment. By observing what is below or swimming at the surface the range of possible coastal and marine applications for such a versatile tool is varied.

Chapter 5: Conclusions

Drones are a powerful tool for utilisation within the built environment and may prove beneficial in advancing existing engineering techniques such as those used for measuring currents as tested in this thesis. The results prove that currents could in fact be measured by a method similar to that of GPS drifters while reducing the risks associated with launching and retrieving of the drifters.

There was an error generated by the consumer DJI Mavic Air drone, but the magnitude of the error was less than the measured currents and was greatly reduced with an averaging filter. The error was also further reduced when the drone was operated such that movements were smooth and only when required, as it was found that in all tests the error greatly increased whenever the drone moved quickly.

This provides a fast-simple method for gathering initial current velocity measurements on site by a single individual and can be coupled with other investigations using the drone such as site mapping. The measurement accuracy could also be improved with newer technology such as the DJI Phantom RTK which greatly improves the accuracy of the drone's location recording and hence would provide more accurate drifter locations at each time-step.

The method of tracking drifters from above using quadcopter drone photography was found to be dependent on conditions such as wind velocity, surface sea foam as well as sun position. As stated above, more advanced drones can handle a higher wind speed while including a polarised filter which would help to reduce glare from the sun. Specially coloured drifters with enhanced drone sensors should be able to pick up the drifters through the glare and possibly even through sea foam. Another aspect on site which influenced the methodology was the local bird life, where the local kelp seagulls were noted to fly at the drone and at locations near a large colony of sea birds this may impact the ability to carry out the investigation. In this case, simply hovering safely over the beach for 30 seconds to a minute, allowed some time for the seagulls to acclimatise to the drone until they lost interest such that the drone could be flown over the water to commence data collection.

The average instantaneous error, characterised as a velocity found in the drone's ability to track stationary points on the ground ranged between 4 $cm.s^{-1}$ and 6 $cm.s^{-1}$ which reduced to around 2 $cm.s^{-1}$ when averaging out the points over 10s for all tests. During the same tests the average drifter velocity measured was around 30 $cm.s^{-1}$ instantaneously (which included orbital velocities from waves) and then reduced to between 18 $cm.s^{-1}$ and 10 $cm.s^{-1}$ for the averaged results corresponding to longer period currents.

Currents were able to be measured and tracked within Monwabisi bay and the magnitudes of these currents as well as the current patterns observed were found to correlate with the results of Kistner's thesis results in certain cases. The other cases which disagreed were where a drifter was found to move in a direction contrary to that modelled by Kistner and CSIR. This could be attributed to wind

and wave surfing effects of the drifter as well as changes in the bathymetry from the modelled profile over time as well as a new pipeline installed in the bay. Further investigation is required to evaluate the surfing susceptibility of oranges as drifters over traditional drifters with baffles.

Chapter 6: Recommendations

The following recommendations were made as part of this study for consideration in future studies:

- The methodology for digitising the aerial photographs to attain the drifter coordinates was manual and tedious. Further study towards the development of an automated tracking method using computer vision is necessary, or possibly excluding drifters by tracking suspended sediments and floating debris.
- There were a number of instances where the drifter experienced surfing effects. In future studies, tests should be carried out to compare simple round drifters to more complex drifters fitted with baffles or a drogue which will prevent the drifter surfing down a wave.
- The images were not corrected for lens distortion as no lens correction profile was available and the effect was assumed negligible for current velocity measurements. Future studies should include a step for calibration of the lens and correction of images before processing in AutoCAD.
- Fitting the camera with a polarising filter to reduce glare of the water surface will assist in identifying the drifters in harsh sunlight.
- The camera used should have a minimum of a 12 mega pixel with calibrated profile to reduce distortion. If there are no budget constraints, then a thermal camera may further assist in identifying the drifter in the water.
- As no concurrent measurements were available for calibration and verification, a further study could carry out similar tests with other concurrent Eulerian or Lagrangian measurements in obtaining a verification measurement of the exact conditions being tested. In addition to this, local wind measurements should be gathered using a hand-held anemometer.
- In addition measurements a more recent survey of the bathymetry should be acquired to ensure that the model results are representative of the actual currents measured.
- The drone measurements were highly susceptible to variations in elevation and an elevation calibration factor was required to account for the difference between the take-off height and the water level which was not accounted for in the drone's absolute height measurement. Therefore, the use of a stereoscopic camera to capture the downward images could reduce the vertical uncertainties of the drone altitude above the water as the images could be used to calculate the exact distance from the drone.

Chapter 7: References

Aagaard, T. & Vinther, N. 2008. Cross-shore currents in the surf zone: rips or undertow? *Journal of Coastal Research*. 243(243):561–570.

Actimar. 2018. *Actimar deployed a high frequency radar network in South Africa*. [Online], Available: http://www.actimar.fr/en/actimar-informs-you/oceanographic-radar-actimar-deployed-a-high-frequency-radar-network-in-south-africa/ [2019, May 15].

Air Shepherd. 2019. *Reversing the march of extinction*. [Online], Available: https://airshepherd.org/ [2019, May 26].

Airshare. 2019. *NZ Drone Rules*. [Online], Available: https://www.airshare.co.nz/rules [2019, May 26].

Anarde, K. & Figlus, J. 2017. Tilt current meters in the surf zone: benchmarking utility in high-frequency oscillatory flow. In *Coastal Dynamics*.

Appeaning Addo, K., Jayson-Quashigah, P.N., Codjoe, S.N.A. & Martey, F. 2018. Drone as a tool for coastal flood monitoring in the Volta Delta, Ghana. *Geoenvironmental Disasters*. 5(1).

Austin, J. & Atkinson, S. 2004. The design and testing of small, low-cost GPS-tracked surface drifters. *Estuaries*. 27(6):1026–1029.

Australian Water Association. 2015. *High-flying drones to find water leaks*. [Online], Available: https://watersource.awa.asn.au/technology/research/high-flying-drones-to-find-water-leaks/ [2019, July 31].

Baker, J. 2016. *Things to know about ground control in drone surveying*. [Online], Available: https://medium.com/@propeller_aero/things-to-know-about-ground-control-in-drone-surveying-6b63ba6ccf0c [2019, May 24].

Baumann, P.R. 2014. *History of remote sensing, aerial photography*. [Online], Available: http://www.oneonta.edu/faculty/baumanpr/geosat2/rs history i/rs-history-part-1.htm [2019, March 28].

BBC News. 2016. *Amazon makes first drone delivery*. [Online], Available: https://www.bbc.com/news/technology-38320067 [2019, May 26].

Benbow, C.A., Macmahan, J.H. & Thornton, E.B. 2017. *Analysis of surface foam holes associated with depth-limited breaking*. [Online], Available: https://www-jstor-org.ez.sun.ac.za/stable/pdf/44393309.pdf?refreqid=excelsior%3A08a66e814c24882c165d57a7210d63a5 [2019, May 29].

Buczkowski, A. 2017. *How accurate is your drone survey? Everything you need to know.* [Online], Available: https://geoawesomeness.com/accurate-drone-survey-everything-need-know/ [2019, March 29].

CIPA & JEITA. 2016. *Exchangeable image file format for digital still cameras: Exif Version 2.31*. [Online], Available: http://www.cipa.jp/std/documents/e/DC-008-Translation-2016-E.pdf [2019, May 30].

Coleman, F. 2019. The Development and Validation of a Hydrodynamic Model of False Bay by. *M. Eng. Thesis, Stellenbosch University, Stellenbosch*. (April).

CTS Heritage. 2017. *Proposed installation of HF Radar on the south coast of RSA*. Cape Town. [Online], Available: https://sahris.sahra.org.za/sites/default/files/heritagereports/HIA Ouwerf HF Radar Wave Monitoring Antennae.pdf [2019, May 15].

D'Agostino, T. 2018. *DJI camera database*. [Online], Available: https://vfxcamdb.com/category/camera/dji/ [2019, June 05].

Daniel, L. 2018. *Festive season drownings spike after deadly weekend at sea*. [Online], Available: https://www.thesouthafrican.com/news/festive-season-drownings-december-nsri/ [2019, May 22].

Darack, E. 2017. *A brief history of quadrotors*. [Online], Available: https://www.airspacemag.com/daily-planet/brief-history-quadrotors-180963372/ [2019, May 02].

Devi, S. & Veena. 2014. Measurement of relief displacement from vertical photograph. *International Journal of Science, Engineering and Technology Research (IJSETR)*. 3(10):2800–2805. [Online], Available: http://docplayer.net/36703507-Measurement-of-relief-displacement-from-vertical-photograph.html [2019, July 31].

DJI. 2013. *ZENMUSE H3-2D gimbal user manual V1. 16*. Shenzhen. [Online], Available: www.dji.com [2019, May 29].

DJI. 2018a. *Mavic air user manual*. [Online], Available: http://www.dji.com/mavic-air/info#video%0Ahttp://www.dji.com/mavic-air/download.

DJI. 2018b. *DJI launches the Phantom 4 RTK globally*. [Online], Available: https://www.dji.com/newsroom/news/dji-launches-the-phantom-4-rtk-globally [2019, May 26].

DJI. 2019a. *Quadcopters for aerial photography*. [Online], Available: https://www.dji.com/ [2019, May 26].

DJI. 2019b. *Drones for agriculture*. [Online], Available: https://enterprise.dji.com/agriculture?site=brandsite&from=nav [2019, July 31].

DJI. 2019c. *ADS-B receivers in consumer-grade drones will set a new standard in drone safety*. [Online], Available: https://www.dji.com/nz/newsroom/news/dji-adds-airplane-and-helicopter-detectors-to-new-consumer-drones [2019, May 29].

DJI. 2019d. *Zenmuse XT - Unlock the possibilities of sight*. [Online], Available: https://www.dji.com/nz/zenmuse-xt [2019, August 11].

Dohan, K. & Maximenko, N. 2010. Monitoring ocean currents with satellite sensors. *Oceanography*. 23(4):94–103.

Dormehl, L. 2018. *The history of drones in 10 milestones*. [Online], Available: https://www.digitaltrends.com/cool-tech/history-of-drones/ [2019, May 02].

DOSITS. 2019. *How is sound used to measure waves in the surf zone?* [Online], Available: https://dosits.org/people-and-sound/research-ocean-physics/how-is-sound-used-to-measure-waves-in-the-surf-zone/ [2019, May 17].

Drone Deploy. 2018a. *Drones in agriculture*. [Online], Available: https://dronedeploy-www.cdn.prismic.io/dronedeploy-www%2Fb6ac1117-09c8-42fe-b31b-53483050e3df_drones_in_agriculture_fv5.pdf [2019, May 26].

Drone Deploy. 2018b. Commercial drone industry trends. (May).

Editorial Board. 2019. *Nadar - biography & facts*. [Online], Available: https://www.britannica.com/biography/Nadar [2019, March 28].

Etheridge, J. 2018. *Lifesaving boss warns of "recipe for disaster" at Cape beach after 3 drown in baptism ceremony*. [Online], Available: https://www.news24.com/SouthAfrica/News/lifesaving-boss-warns-of-recipe-for-disaster-at-cape-beach-after-3-drown-in-baptism-ceremony-20180326 [2019, May 22].

Fallon, K.M., Lai, Q. & Leatherman, S.P. 2018. Rip current literacy of beachgoers at Miami Beach, Florida. *Natural Hazards*. 90(2):601–621.

Ferry, D. 2016. *Everything you know about surviving rip currents is wrong*. [Online], Available: https://www.outsideonline.com/2089696/everything-you-know-about-surviving-rip-currents-wrong [2019, May 24].

Fietemeyer, J. 2014. The reliability of turbidity and debris moving seaward to spot rip currents on florida beaches and the need for better warning and education programs. *Journal of Coastal Research*. (72):39–43.

Ford, J. 2018. *The history Of drones*. [Online], Available: https://www.dronethusiast.com/history-of-drones/

[2019, April 29].

French, S. 2018. *DJI market share: here's exactly how rapidly it has grown in just a few years*. [Online], Available: http://thedronegirl.com/2018/09/18/dji-market-share/ [2019, May 02].

Gallop, S.L., Bryan, K.R., Pitman, S.J., Ranasinghe, R., Sandwell, D.R. & Harrison, S.R. 2018. Rip current circulation and surf zone retention on a double barred beach. *Marine Geology*. 405(June):12–22.

Gudaitis, F. 1994. The first days of Radio Control. *Model Airplane News*. [Online], Available: https://www.modelairplanenews.com/the-first-days-of-rc/ [2019, May 02].

Half Chrome. 2018. *Mavic Air camera test*. [Online], Available: https://www.halfchrome.com/mavic-air-camera/ [2019, May 23].

Hamukuaya, H., Willemse, N., O'Toole, M. & Attwood, C. 2013. *Science To Governance in the Benguela*.

Harvey, P. 2018. *ExifTool*. Ontario. [Online], Available: https://owl.phy.queensu.ca/~phil/exiftool/.

Hughes, A., Teuten, E., Starnes, T., Cowie, C.N., Swinfield, T., Humpidge, R., Williams, J., Bridge, D., et al. 2018. Drones for GIS – best practice. [Online], Available: https://www.wildlabs.net/sites/default/files/community/files/drones_for_gis_-_best_practice_1.3_0.pdf [2019, May 23].

Hutchings, L., van der Lingen, C.D., Shannon, L.J., Crawford, R.J.M., Verheye, H.M.S., Bartholomae, C.H., van der Plas, A.K., Louw, D., et al. 2009. The Benguela Current: An ecosystem of four components. *Progress in Oceanography*. 83(1–4):15–32.

Inch, K.W. 2014. Surf zone hydrodynamics: measuring waves and currents. *Geomorphological Techniques*. Chap. 3, S. [Online], Available: https://geomorphology.org.uk/sites/default/files/geom_tech_chapters/3.2.3_SurfZoneHydrodynamics.pdf [2019, May 16].

Kaamin, M., Daud, E., Sanik, E., Farah, N., Ahmad, A., Mokhtar, M., Ngadiman, N. & Yahya, F.R. 2016. Mapping shoreline position using unmanned aerial vehicle production of orthophoto map using UAV photogrammetry. In Vol. 020063 *AIP Conference*. 1–6.

Kalantar, B., Mansor, S. Bin, Abdul Halin, A., Shafri, H.Z.M. & Zand, M. 2017. Multiple moving object detection from UAV videos using trajectories of matched regional adjacency graphs. *IEEE Transactions on Geoscience and Remote Sensing*. 55(9):5198–5213.

Keaikitse, A.S. 2014. Long-term tracking of multiple interacting pedestrians using a single camera. Stellenbosch : Stellenbosch University. [Online], Available: https://scholar.sun.ac.za/handle/10019.1/86632 [2019, May 28].

Kistner, S. 2016. Monwabisi: a hydrodynamic study of the hazardous cell circulation and potential related solutions to a safer bathing facility. *M. Eng. Thesis, Stellenbosch University, Stellenbosch*. (December).

Kruger, I. & Wilson, E.G. 2010. Morphology and affiliation of the centric diatom Anaulus birostratus (Grunow) Grunow from South Africa. *South African Journal of Marine Science*. 2(1):163–194.

Laporte-Fauret, Q., Marieu, V., Castelle, B., Michalet, R., Bujan, S. & Rosebery, D. 2019. Low-Cost UAV for high-resolution and large-scale coastal dune change monitoring using photogrammetry. *Journal of Marine Science and Engineering*. 7(3):1–16.

Leatherman, S.B. 2017. Rip current measurements at three south florida beaches. *Journal of Coastal Research*. 335(5):1228–1234.

Long, N., Millescamps, B., Guillot, B., Pouget, F. & Bertin, X. 2016. Monitoring the topography of a dynamic tidal inlet using UAV imagery. *Remote Sensing*. 8(5):1–18.

Lowell Instruments LLC. 2015. *TCM-1 Tilt current meter brochure*. [Online], Available: www.lowellinstruments.com [2019, May 16].

Lowell Instruments LLC. n.d. *TCM-1 Tilt current meter*. [Online], Available:

https://lowellinstruments.com/products/tcm-1-tilt-current-meter/ [2019, May 16].

Madeira, B. & Green, S. 2016. *History of aerial photography*. [Online], Available: http://academic.emporia.edu/aberjame/student/madeira3/history.html [2019, March 28].

Mangor, K. 2019. *Currents*. Coastal Wiki. [Online], Available: http://www.coastalwiki.org/wiki/Currents.

McCarroll, R.J., Brander, R.W., MacMahan, J.H., Turner, I.L., Reniers, A.J.H.M., Brown, J.A., Bradstreet, A. & Sherker, S. 2014. Evaluation of swimmer-based rip current escape strategies. *Natural Hazards*. 71(3):1821–1846.

McCarroll, R.J., Brander, R.W., Turner, I.L., Power, H.E. & Mortlock, T.R. 2014. Lagrangian observations of circulation on an embayed beach with headland rip currents. *Marine Geology*. 355:173–188.

Mrovlje1, J. & Vrančić, D. 2008. *Distance measuring based on stereoscopic pictures*. Slovenia. [Online], Available: http://dsc.ijs.si/files/papers/s101 mrovlje.pdf [2019, August 12].

Mulakala, J. 2019. *Measurement accuracy of the DJI phantom 4 RTK & photogrammetry*. [Online], Available: https://dronedeploy-www.cdn.prismic.io/dronedeploy-www%2F93423f49-b020-4b5a-8546-7ed3ccbde6cd_dji_phantom_4_rtk_book_f-2.pdf.

Murray, T., Cartwright, N. & Tomlinson, R. 2013. Video-imaging of transient rip currents on the Gold Coast open beaches. *Journal of Coastal Research*. 165(65):1809–1814.

NASA. 2015. First pictures of Earth from 100 miles in space. [Online], Available: https://www.nasa.gov/multimedia/imagegallery/image_feature_1298.html [2019, March 28].

NGI. 2013a. *Aerial photography (1926-2008)*. [Online], Available: http://www.ngi.gov.za/index.php/what-we-do/aerial-photography-and-imagery/34-aerial-photography-1926-2008 [2019, April 29].

NGI. 2013b. *Colour digital aerial imagery at 0.5m GSD (2008-2016) and 0.25 GSD (2017-current)*. [Online], Available: http://www.ngi.gov.za/index.php/what-we-do/aerial-photography-and-imagery/35-colour-digital-aerial-imagery-at-0-5m-gsd-2008-2016-and-0-25m-gsd-2017-current [2019, April 29].

NOAA. 2018. *HF radar surface currents*. [Online], Available: https://tidesandcurrents.noaa.gov/hfradar/ [2019, May 20].

Nortek. 2019. *The science behind a simple wave*. [Online], Available: https://www.nortekgroup.com/insight/nortek-wiki/the-science-behind-a-simple-wave [2019, May 17].

NSRI. 2018. *Beware of rip currents.* [Online], Available: http://www.nsri.org.za/2018/06/beware-of-rip-currents/ [2019, May 22].

Oanes, E.I. 2011. *Acoustic doppler velocimeter (Nortek, Vector) in a Posidonia oceanica meadow*. [Online], Available: https://www.flickr.com/photos/eduardoinfates/6304243437/in/photostream/.

Olsson, D. 2004. Field studies of rip currents in the lee of coastal structures. University of Western Australia.

Palmer, M. 2002. Acoustic doppler velocimetry. 1. [Online], Available: http://web.mit.edu/fluids-modules/www/exper_techniques/1.ADV.Principleof_Operation.pdf [2019, May 16].

Parker, A. 2011. *The South African coordinate reference system*. Cape Town.

Piepmeier, J., Jennifer, W. & Broussard, R. 2006. A stereo vision-based wave surface measurement project. *American Society for Engineering Education*. 11–124(2364):1–12.

Pijoos, I. 2016. *Man drowns at Amanzimtoti beach*. [Online], Available: https://www.news24.com/SouthAfrica/News/man-drowns-at-amanzimtoti-beach-20161204 [2019, May 22].

Plant, N.G., Long, J.W., Dalyander, P.S., Thompson, D.M. & Raabe, E.A. 2013. *Application of a hydrodynamic and sediment transport model for guidance of response efforts related to the Deepwater Horizon oil spill in the Northern Gulf of Mexico along the coast of Alabama and Florida*. Virginia. [Online], Available: http://pubs.usgs.gov/of/2012/1234/. [2019, May 27].

Putch, A. 2017. *Linear measurement accuracy of DJI drone platforms and photogrammetry*. San Francisco. [Online], Available: https://dronedeploy-www.cdn.prismic.io/dronedeploy-www%2F46e720cd-fb03-41ec-a6a3-09b424d674b8_linear+measurement+accuracy+of+dji+drone+platforms+and+cloud-based+photogrammetry-v11.pdf [2019, May 24].

Reichhardt, T. 2006. *First photo from space*. [Online], Available: https://www.airspacemag.com/space/the-first-photo-from-space-13721411/ [2019, March 28].

Ricker, E. 2017. *Flying over water - downward positioning sensors on or off?* [Online], Available: https://www.youtube.com/watch?v=FihnvkaN83M [2019, August 06].

Roarty, D.H. 2014. *The global high frequency radar network*. [Online], Available: https://earthzine.org/the-global-high-frequency-radar-network/ [2019, May 15].

Roberts, M.J., van der Lingen, C.D., Whittle, C. & van den Berg, M. 2010. Shelf currents, lee-trapped and transient eddies on the inshore boundary of the agulhas current, South Africa: Their relevance to the kwaZulu-Natal sardine run. *African Journal of Marine Science*. 32(2):423–447.

Le Roux, M. 2018. Assessment of coastline effluent dispersion by means of dye and colour photography. In University of Stellenbosch *2018 Coastal Engineering Short Course*.

SACAA. 2015. *Remotely piloted aircraft systems (Part 101) regulations workshops RPAS regulations (Part 101)*. Johannesburg. [Online], Available: http://www.caa.co.za/Documents/RPAS/Part 101 - RPAS Workshops.pdf [2019, May 29].

SACAA. 2017a. *General information*. [Online], Available: http://www.caa.co.za/pages/rpas/remotely piloted aircraft systems.aspx [2019, May 06].

SACAA. 2017b. *RPAS private operations*. [Online], Available: http://www.caa.co.za/pages/rpas/private operations.aspx.

SACAA. 2019. *RPAS operators*. [Online], Available: http://www.caa.co.za/Pages/RPAS/RPAS operators.aspx [2019, May 26].

Satellite Imaging Corp. 2017. *Orthorectification of satellite imagery*. [Online], Available: https://www.satimagingcorp.com/services/orthorectification/ [2019, May 23].

Savides, M. 2017. *Bumper new year's weekend for Durban*. [Online], Available: https://www.timeslive.co.za/news/south-africa/2017-01-02-bumper-new-years-weekend-for-durban/ [2019, May 22].

Scott, T., Austin, M., Masselink, G. & Russell, P. 2016. Dynamics of rip currents associated with groynes - field measurements, modelling and implications for beach safety. *Coastal Engineering*. 107:53–69.

Shin, S., Nam, J., Son, S., Kim, I.H. & Jung, T.-H. 2017. Field observation and numerical modelling of rip currents within a pocket beach. *Journal of Coastal Research*. 79:229–233.

Short, A.D. & Hogan, C.L. 1994. Rip currents and beach hazards: their impact on public safety and implications for coastal management. *Journal of Coastal Research*. (12):197–209.

SonTek. 2010. *Argonaut-ADV brochure*. San Diego. [Online], Available: www.sontek.com [2019, May 16].

SonTek. 2017. *Acoustic doppler profiler (ADP) and Mini-ADP systems*. San Diego. [Online], Available: www.xyleminc.com [2019, May 16].

Statistics South Africa. 2016. *Mortality and causes of death in South Africa, 2016: Findings from death notification*. Pretoria. [Online], Available: www.statssa.gov.zainfo@statssa.gov.za [2019, May 22].

Stringari, C.E., Harris, D.L. & Power, H.E. 2019. A novel machine learning algorithm for tracking remotely sensed waves in the surf zone. *Coastal Engineering*. 147:149–158.

Sun, H., Song, Q., Shao, R. & Schlicke, T. 2016. Estimation of sea surface currents based on ocean colour remote-sensing image analysis. *International Journal of Remote Sensing*. 37(21):5105–5121.

Sutron. 2019. *Acoustic wave and current profiler (AWAC)*. [Online], Available: https://www.sutron.com/product/acoustic-wave-and-current-profiler/ [2019, May 17].

Theron, A.K. & Schoonees, J.S. 2007. Sand transport at and shoreline response to a breakwater attached to a large tidal pool at Monwabisi, Cape Town. *Journal of the South African Institution of Civil Engineers*. 49(2):2–9.

Theron, A.K., Van Tonder, A., Blake, K., Barwell, L., Schoonees, J.S., Van Dulm, F. & Vonk, A. 1997. *Monwabisi beach safety*. Cape Town: CSIR.

Timeslive. 2017. *Places where most drownings occur - and when*. [Online], Available: https://www.timeslive.co.za/news/south-africa/2017-12-13-places-where-most-drownings-occur-and-when/ [2019, May 22].

Turi, J. 2014. *Tracing the origins of the multirotor drone, for business and pleasure*. [Online], Available: https://www.engadget.com/2014/11/02/tracing-the-origins-of-the-multirotor-drone/#/ [2019, May 02].

U.S. Air Force. 2017. *GPS accuracy*.

U.S. Army Corps of Engineers. 2003. CEM Part II Chapter 4 surf zone hydrodynamics. 1100(July):20–27.

Upadhyay, N. 2014. *Basics of photogrammetry*. [Online], Available: http://www.gisresources.com/basic-of-photogrammetry_2/ [2019, May 23].

Viriyakijja, K. & Chinnarasri, C. 2015. Wave flume measurement using image analysis. *Aquatic Procedia*. 4(Icwrcoe):522–531.

Visser, P.J. 1991. Laboratory measurements of uniform longshore currents. *Coastal Engineering*. 15(5–6):563–593.

Watereuse Association. 2011. *Seawater concentrate management white paper*. [Online], Available: https://watereuse.org/wp-content/uploads/2015/10/Seawater_Concentrate_WP.pdf [2019, June 22].

WHO. 2019. *Drowning*. World Health Organization. [Online], Available: https://www.who.int/violence_injury_prevention/drowning/en/ [2019, May 22].

WindGuru. 2019. *Macassar forecast*. [Online], Available: https://www.windguru.cz/208292 [2019, May 02].

Wolkersdorfer, C. & LeBlanc, J. 2012. Canadian tracer test legislation. *Water Quality Research Journal of Canada*. 47(1):42–55. [Online], Available: https://watermark.silverchair.com/42.pdf?token=AQECAHi208BE49Ooan9kkhW_Ercy7Dm3ZL_9Cf3qfKAc485ysgAAAfAwggHsBgkqhkiG9w0BBwagggHdMIIB2QIBADCCAdIGCSqGSIb3DQEHATAeBglghkgBZQMEAS4wEQQMjeValEsNGR3M4hsLAgEQgIIBoxyeC84mH6lKD5KOmBi0L7TpwEsDSMDVnhq6vBIu-HWh6EVeBB9W [2019, May 22].

Appendix: A Drifter Profile A3 Drawings

A.1 Drawing: Flight FA 2018-05-15

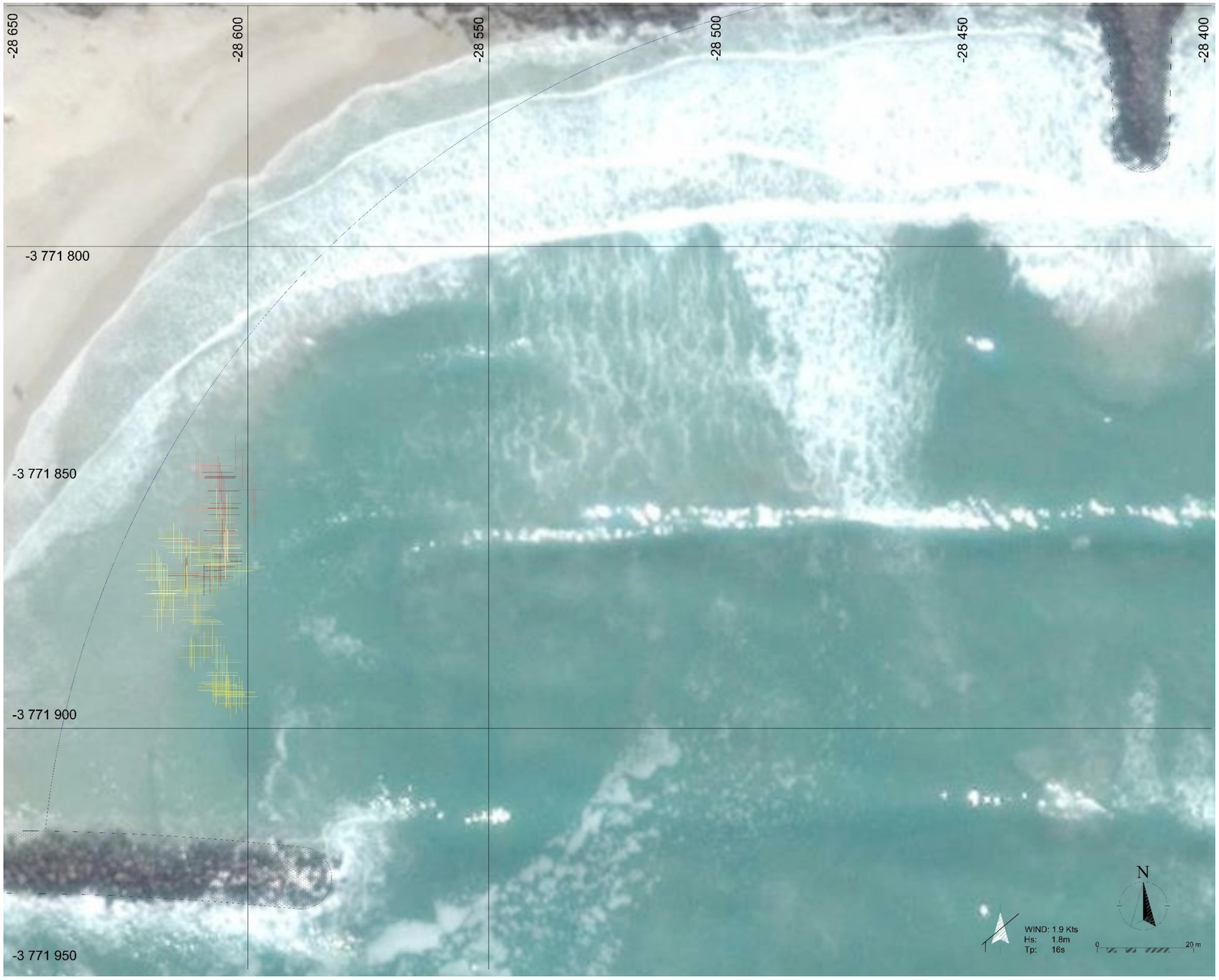

A.2 Drawing: Flight FB 2018-07-17

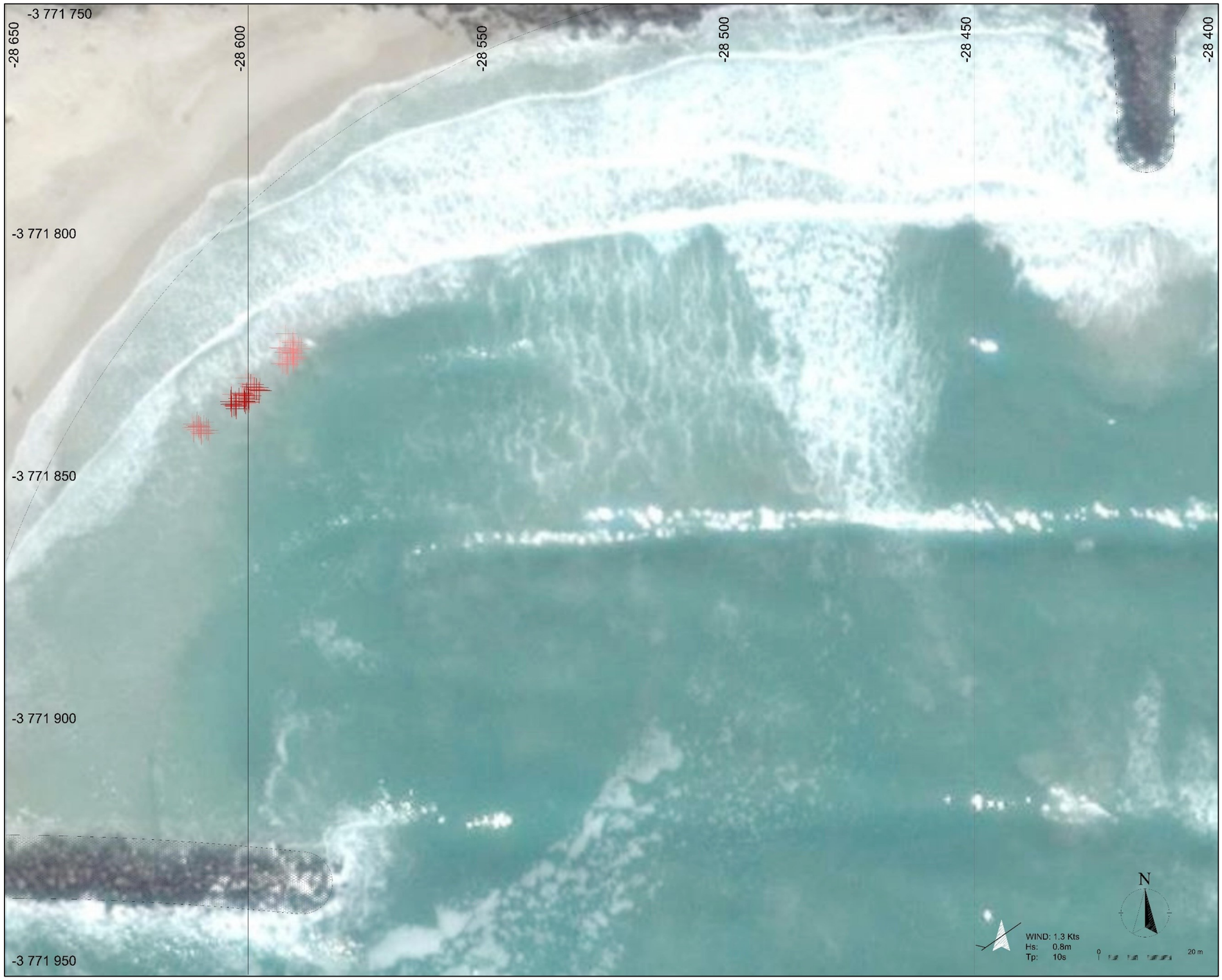

A.3 Drawing: Flight FC 2018-12-11

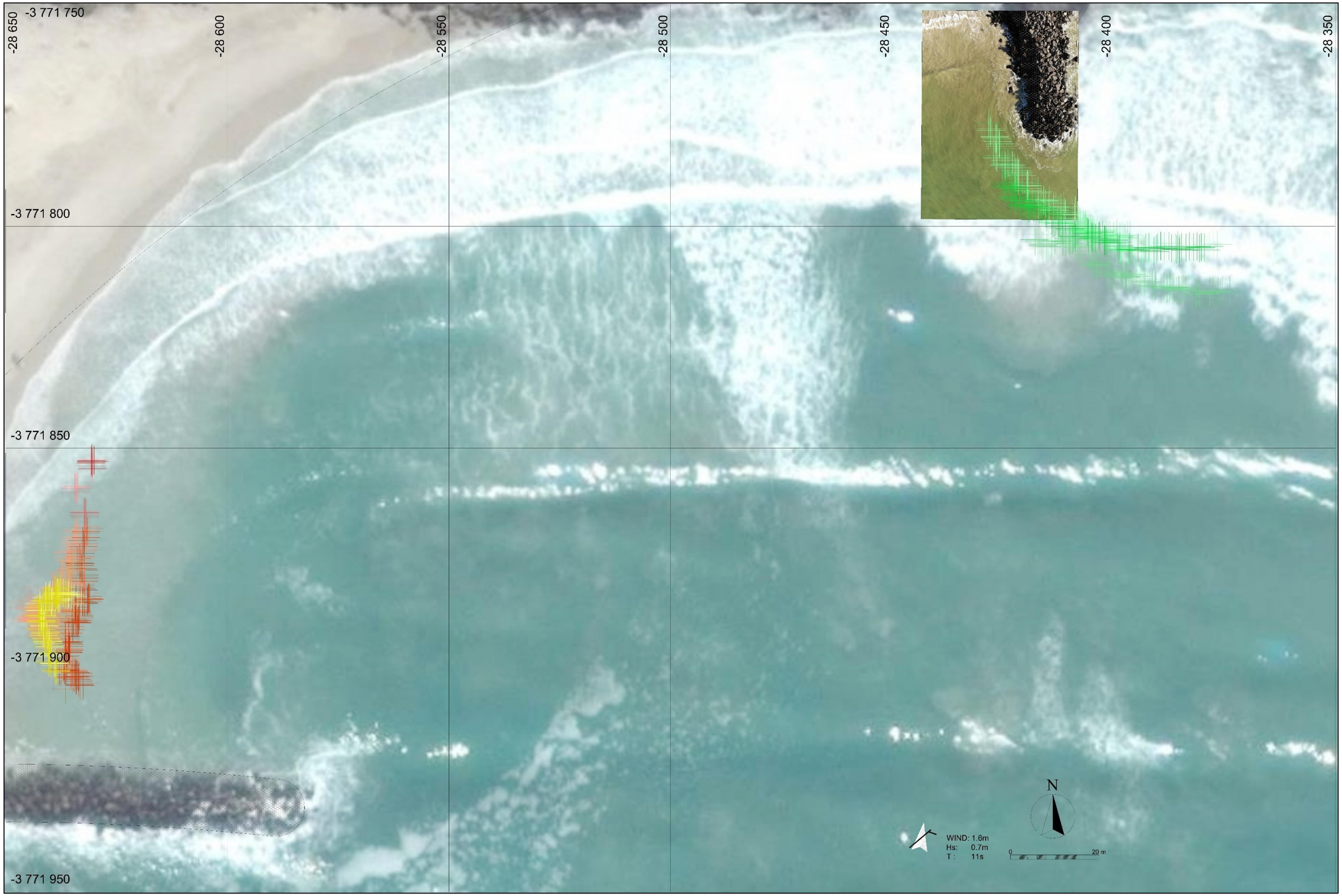

A.4 Drawing: Flight FD 2019-01-07

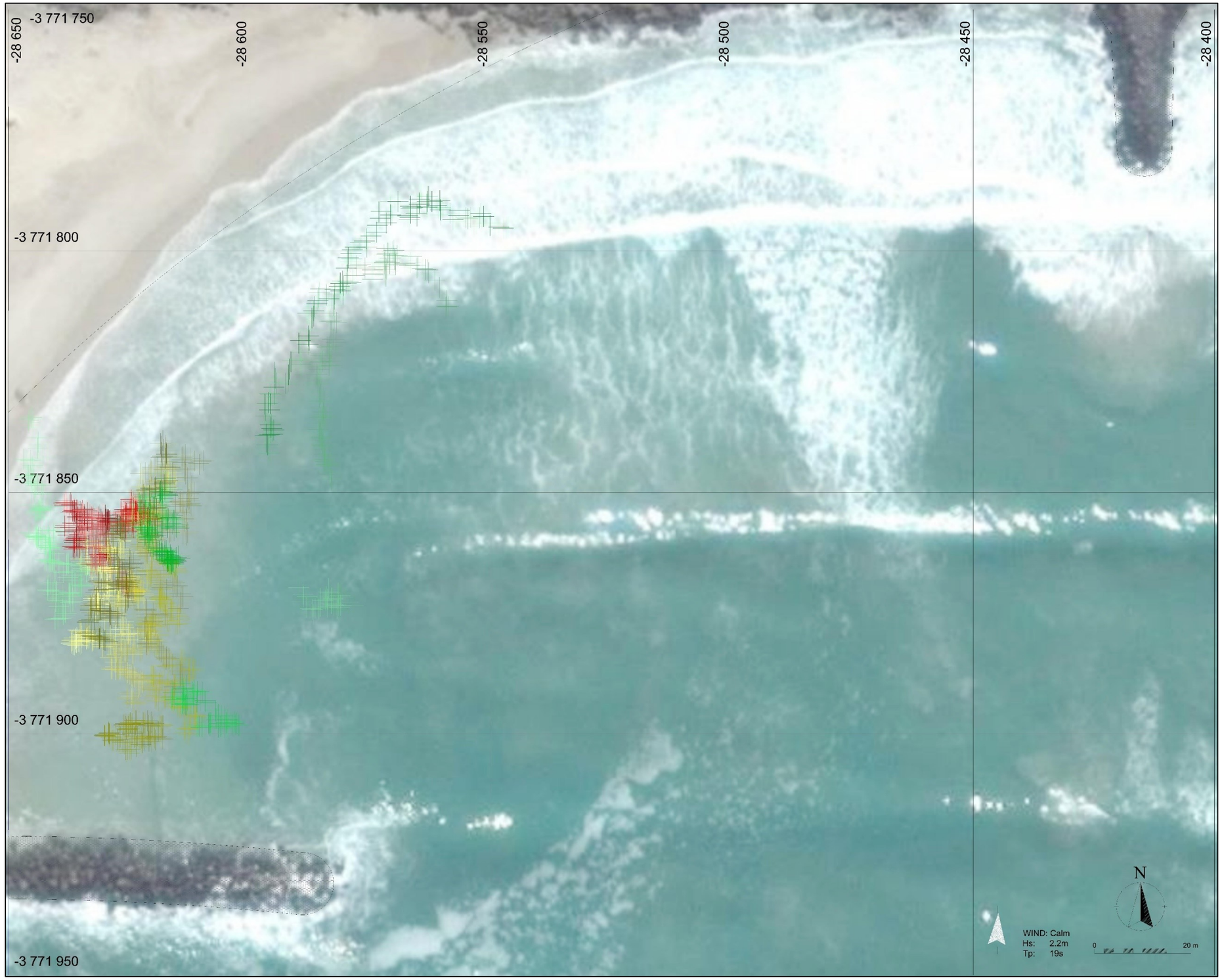

A.5 Drawing: Flight FE 2019-01-11

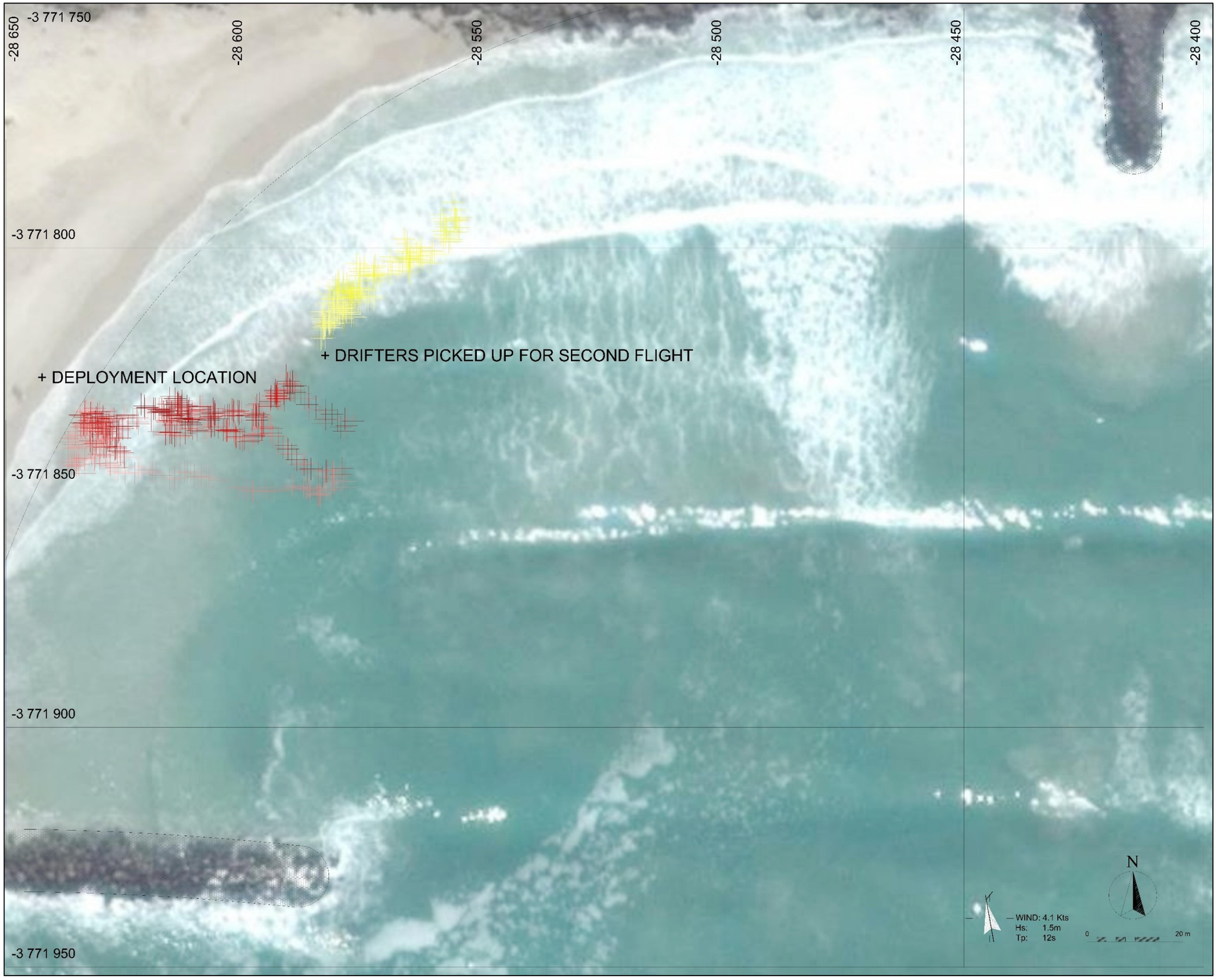

A.6 Drawing: Flight FF 2019-01-17

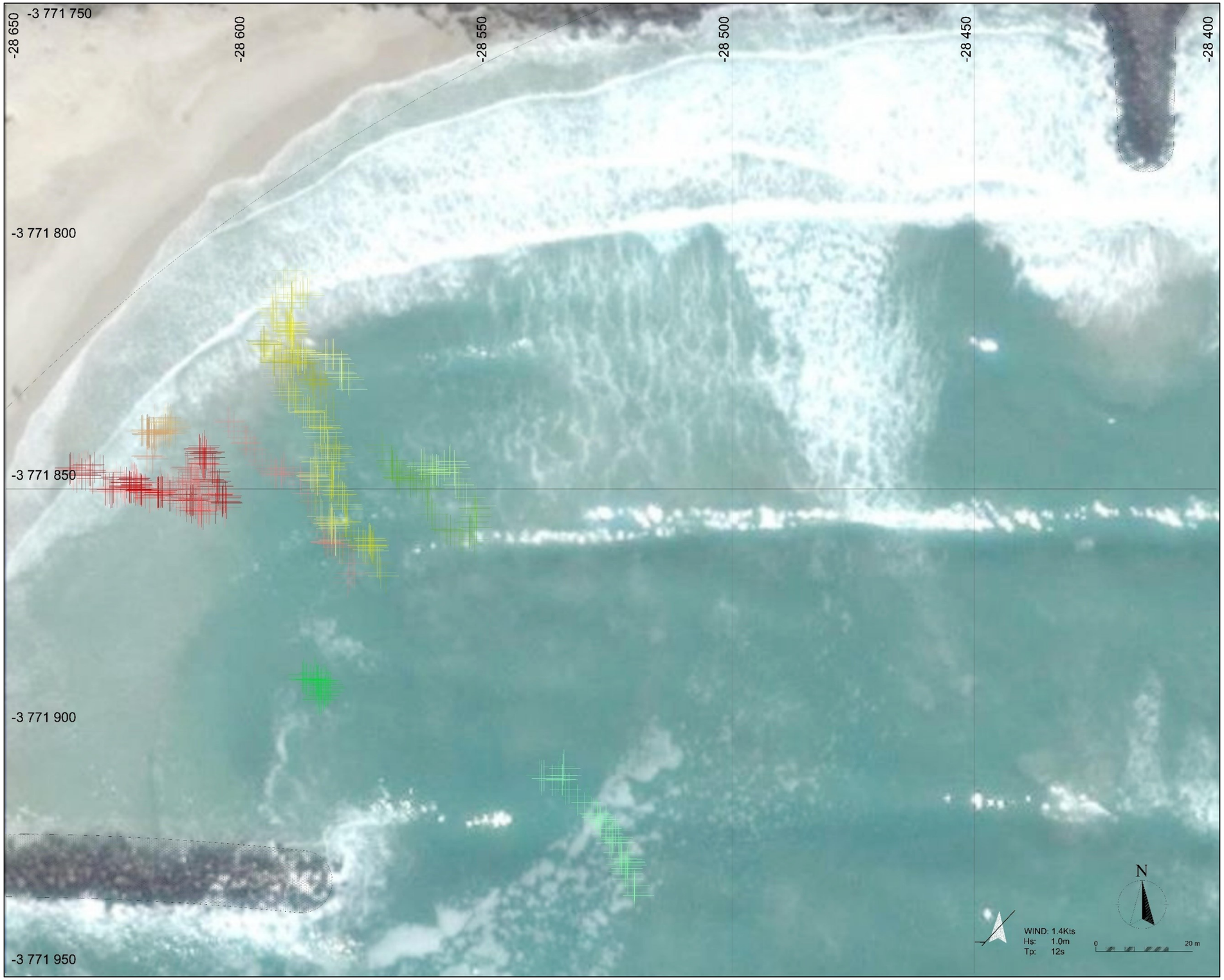

A.7 Drawing: Flight FH 2019-02-05

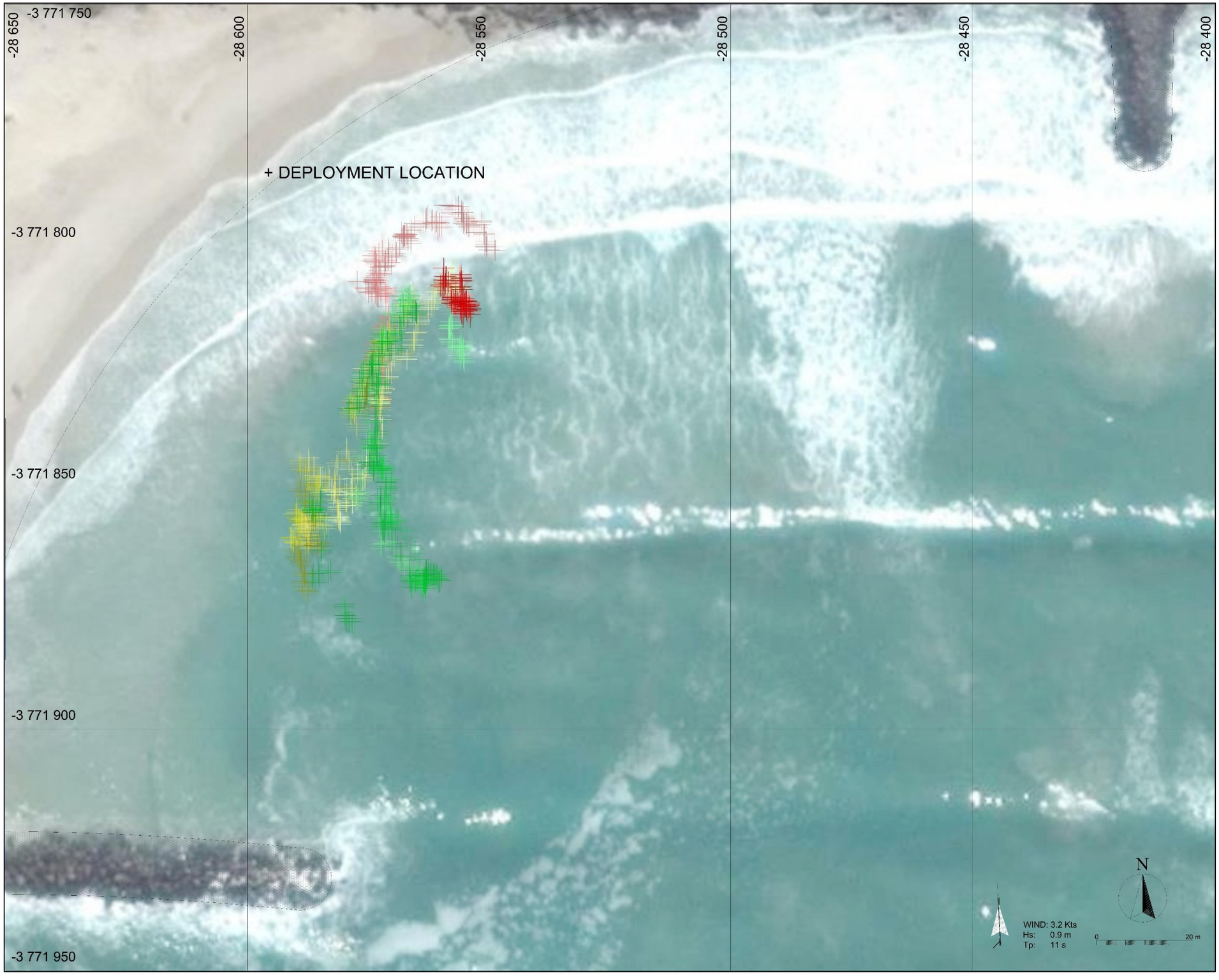

A.8 Drawing: Flight FI 2019-02-07

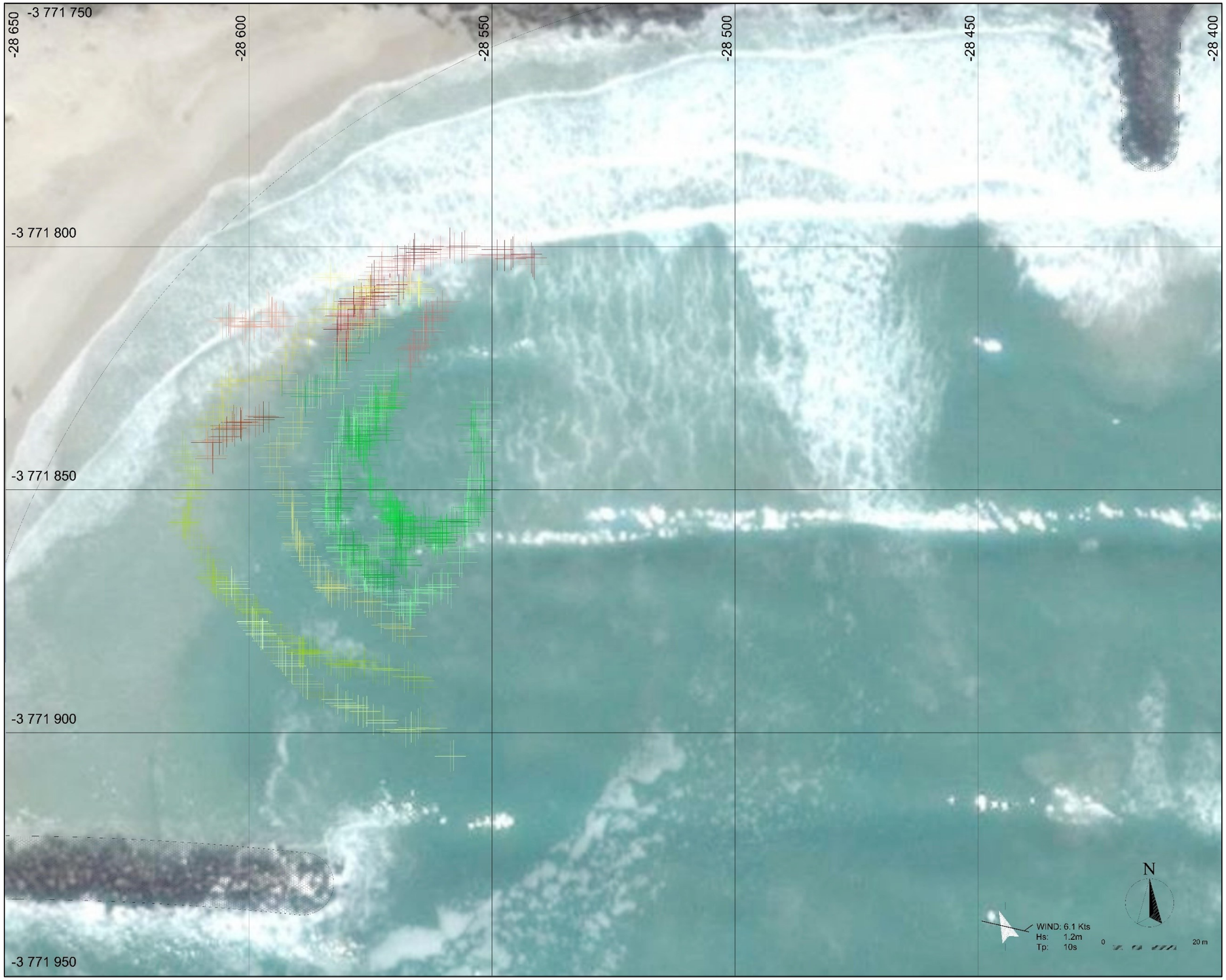

A.9 Drawing: Flight FJ 2019-04-11

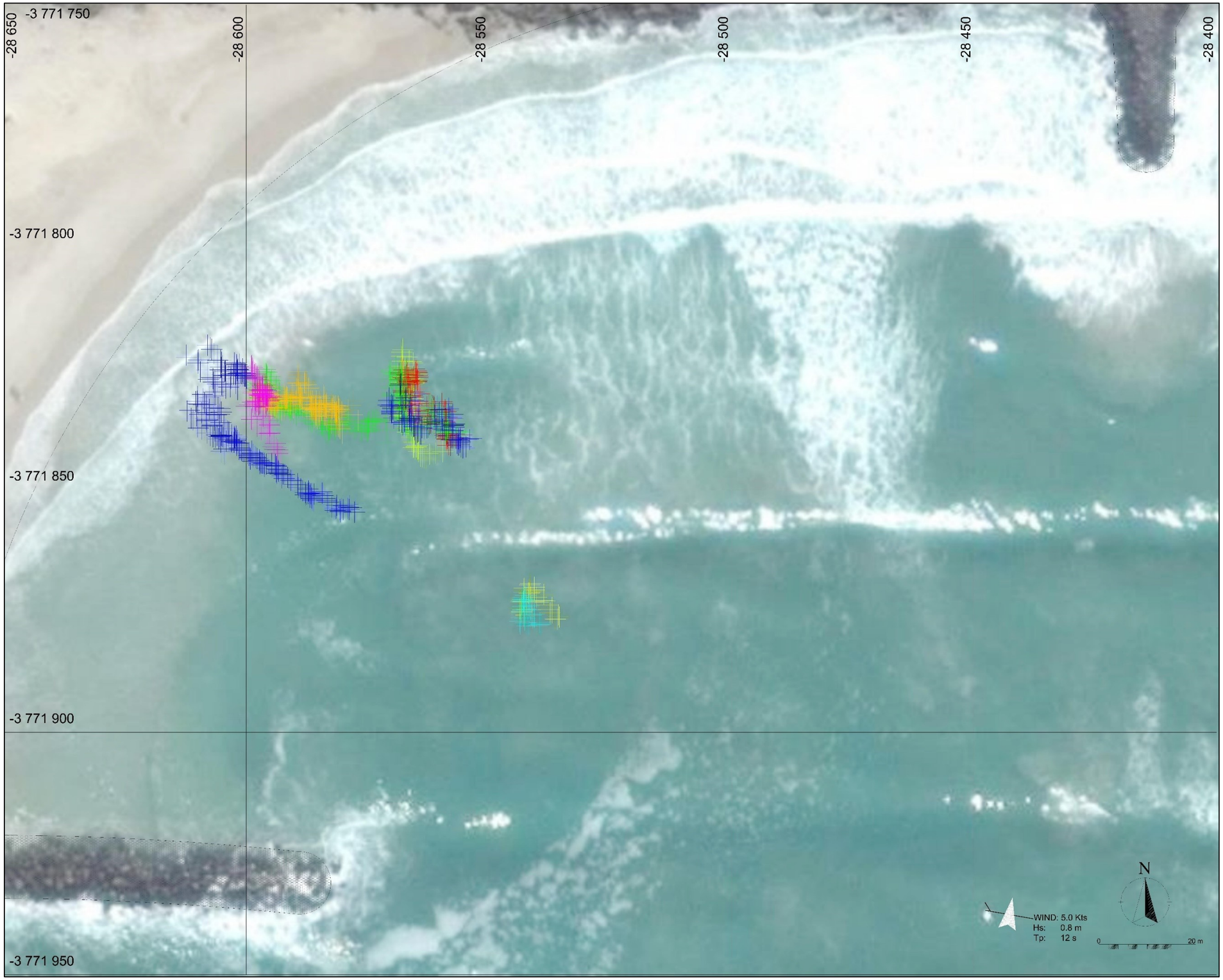

Appendix: B Car Park Calibration Drawing

Car Park Calibration Drawing

Appendix: C Coordinate Transformation

Coordinate Transformation

Aslam Parker provided the following equations in order to convert Geographical coordinates (Lat, Long) into Gauss Conform coordinates for the Southern Hemisphere (2011).

Given the following equations:

$$e^2 = \frac{a^2 - b^2}{a^2}$$

$$e'^2 = \frac{a^2 - b^2}{b^2}$$

$$\eta^2 = e'^2.\cos^2\phi \; ; \qquad \tau = \tan\phi$$

$$A = 1 + \frac{3}{4}.e^2 + \frac{45}{64}.e^4 + \frac{175}{256}.e^6 + \frac{11025}{16384}.e^8 + \frac{43659}{65536}.e^{10}$$

$$B = \frac{3}{4}.e^2 + \frac{15}{16}.e^4 + \frac{525}{512}.e^6 + \frac{2205}{2048}.e^8 + \frac{72765}{65536}.e^{10}$$

$$C = \frac{15}{64}.e^4 + \frac{105}{256}.e^6 + \frac{2205}{4096}.e^8 + \frac{10395}{16384}.e^{10}$$

$$D = \frac{35}{512}.e^6 + \frac{315}{2048}.e^8 + \frac{31185}{131072}.e^{10}$$

$$E = \frac{315}{16384}.e^8 + \frac{3465}{65536}.e^{10}$$

$$F = \frac{693}{131072}.e^{10}$$

$$B_\phi = a.(1 - e^2).\left(A.\phi - \frac{B}{2}.\sin 2\phi + \frac{C}{4}.\sin 4\phi - \frac{D}{6}.\sin\phi + \frac{E}{8}.\sin 8\phi - \frac{F}{10}.\sin 10\phi\right)$$

$\ell = \lambda_0 - \lambda$ (where λ_0 is the longitude of the central meridian)

$$N = \frac{a}{\sqrt{1 - e^2.\sin^2\phi}}$$

$$x = B_\phi + \frac{\ell^2}{2}.N\sin\phi.\cos\phi + \frac{\ell^4}{24}.N.\sin\phi.\cos^3\phi.(5 + 9\eta^2 + 4\eta^4 - \tau^2) + \frac{\ell^6}{720}.N.\sin\phi.\cos^5\phi.(61 - 58\tau^2 + \tau^4 + 270\eta^2 - 330\eta^2\tau^2) + \ldots$$

$$y = \ell.N.\cos\phi + \frac{\ell^3}{6}.N.\cos^3\phi.(1 + \eta^2 - \tau^2) + \frac{\ell^5}{120}.N.\cos^5\phi.(5 - 18\tau^2 + \tau^4 + 14\eta^2 - 58\eta^2\tau^2) + \ldots$$

For the World Geodetic System 1984 ellipsoid the defining parameters are as follows:

- Semi-major axis (a) : 6378137.0 m
- Semi-major axis (b) : 6356752.314 m
- Ellipsoid flattening (f) : 1/298.257223563

Therefore, the equations set out above become:

$$e^2 = \frac{a^2 - b^2}{a^2} = \frac{6378137.0^2 - 6356752.314^2}{6356752.314^2} = 9.01675E + 17$$

$$e'^2 = \frac{a^2 - b^2}{b^2} = \frac{6378137.0^2 - 6356752.314^2}{6356752.314^2} = 0.006739497$$

Substituting e² and e'²

$$\eta'^2 = e'^2 . \cos^2\phi = \sqrt{0.0820944379500043^2 * \cos\Phi^2}$$

$$\tau = \tan\Phi$$

A = 1.005052502

B = 0.005063109

C = 1.06276E-05

D = 2.08204E-08

E = 3.93237E-11

F = 7.10845E-14

$$B_\Phi = 6378137.(1 - 0.0818191908429654^2).(1.00505250178825\Phi - \frac{0.00506310859728167}{2}.\sin 2\Phi + \frac{0.0000106275901588916}{4}.\sin 4\Phi - \frac{2.08203782649766E^{-08}}{6}.\sin\Phi + \frac{3.93237129393568E^{-11}}{8}.\sin 8\Phi - \frac{7.1084532292291E^{-14}}{10}.\sin 10\Phi)$$

λ_0 = 19° in radians

$$\ell = \lambda_0 - \lambda = 0.331612557878923 - \lambda$$

$$N = \frac{a}{\sqrt{1 - e^2.\sin^2\Phi}} = \frac{6378137}{\sqrt{1 - 0.0818191908429654^2.\sin^2\Phi}}$$

Substituting these results into the final equations provided the X & Y coordinates as follows.

$$x = B_\Phi + \frac{\ell^2}{2}.N.\sin\Phi.\cos\Phi + \frac{\ell^4}{24}.N.\sin\Phi.\cos\Phi^3.(5 + 9\eta^2 + 4\eta^4 - \tau^2) + \frac{\ell^6}{720}.N.\sin\Phi.\cos\Phi^5.(61 - 58\tau^2 + \tau^4 + 270\eta^2 - 330\eta^2.\tau^2)$$

$$y = \ell.N.\cos\Phi + \frac{\ell^3}{6}.N.\cos\Phi^3.(1 + \eta^2 - \tau^2) + \frac{\ell^5}{120}.N.\cos\Phi^5.(5 - 18\tau^2 + \tau^4 + 14\eta^2 - 58\eta^2.\tau^2)$$

These equations can then be programmed into Excel to transform each coordinate:

F	G	H	I	J	K	L	M	N	O	P	Q
			Transform Coordinates								
Latitude	Longitude		X (CAD-y)	Y (CAD-x)	Φ	λ	η	τ	B_Φ	ℓ	N
-34.0726	18.690167		-3771759.298	-28599.529	0.5946793	0.326205	0.0680011	0.676354	3771716	0.0054076	6384848.4
-34.0726	18.690169		-3771759.442	-28599.381	0.59467932	0.326205	0.0680011	0.6763541	3771716.1	0.0054076	6384848.4
-34.0726	18.690168		-3771759.553	-28599.482	0.59467934	0.326205	0.0680011	0.6763541	3771716.2	0.0054076	6384848.4
-34.0726	18.690168		-3771759.530	-28599.408	0.59467933	0.326205	0.0680011	0.6763541	3771716.2	0.0054076	6384848.4
-34.0726	18.69017		-3771759.486	-28599.270	0.59467933	0.326205	0.0680011	0.6763541	3771716.2	0.0054076	6384848.4
-34.0726	18.690171		-3771759.430	-28599.196	0.59467932	0.326205	0.0680011	0.6763541	3771716.1	0.0054075	6384848.4
-34.0726	18.690171		-3771759.419	-28599.122	0.59467932	0.326205	0.0680011	0.6763541	3771716.1	0.0054075	6384848.4
-34.0726	18.690173		-3771759.241	-28599.012	0.59467929	0.326205	0.0680011	0.676354	3771715.9	0.0054075	6384848.4

Appendix: D Processing Code

D.1 AutoCAD processing code

```
'Define Global Variables
Public imageNames() As String
Public currentImage As Long
Public numImages As Long
Public fileDirectory As String
Public imageList As String

Function DefineDirectory()  'Define the file paths
    fileDirectory = "C:\Users\Ryan\Documents\Thesis_Working\2018-05-15_MavicAirTest" & "\"  ' File directory path
    imageList = "2018-05-15_MavicAirTest_CalculationsF4.18+1.6m.csv" ' Image list .csv filename"
End Function

Sub AttachMultipleImages()  'Run this first, Photos defined in the imageList will be inported into AutoCAD
    '*** Define Variables ***
    Dim insertionPoint(0 To 2) As Double    'Variable used to centre the image over the origin (based on image dimensions)
    Dim scalefactor As Double               'Scale based on the width
    Dim rotationAngle As Double             'Angle from North
    Dim ImageName As String
    Dim rasterObj As AcadRasterImage
    Dim photoDirectory As String
    Dim point1(0 To 2) As Double            'Origin Point
    Dim point2(0 To 2) As Double            'Image Centre Point

    DefineDirectory
    point1(0) = 0: point1(1) = 0: point1(2) = 0    'Define Origin coordinate for moving image from

    photoDirectory = fileDirectory & "Photos\" 'File directory of photos - ensure photos in folder named \Photos   NB!

    '** Read in CSV **
        Set fso = CreateObject("Scripting.FileSystemObject")

        Dim LineValues() As String    'Array of values in each line
        Dim ReadLine As String        'Each new line read in from the text stream

        Set ts = fso.OpenTextFile(fileDirectory & imageList)         'Open CSV file for photo coordinates

        Do Until ts.AtEndOfStream                   'Leep going till no more lines
            ReadLine = ts.ReadLine                  'Read in a line
            LineValues = Split(ReadLine, ",")       'Split using commas

            insertionPoint(0) = -LineValues(4) / 2  'Read in the width of the image for the top left insertion point y coordinate
            insertionPoint(1) = -LineValues(5) / 2  'Read in the height of the image for the top left insertion point x coordinate
            insertionPoint(2) = 0                   'Define the insertion point z coordinate to 0
            scalefactor = LineValues(4)             'Scale factor of the image set to FOVw
            rotationAngle = -LineValues(3) * 3.14159265359 / 180    'Rotate the image to GimbalYaw in radians

            On Error GoTo ERRORHANDLER
            ' Attach the raster image in model space
            Set rasterObj = ThisDrawing.ModelSpace.AddRaster(photoDirectory & LineValues(0), insertionPoint, scalefactor, 0)

            point2(0) = LineValues(1): point2(1) = LineValues(2): point2(2) = 0
            'Define image coordinate from file
            rasterObj.ImageVisibility = False       'Start image as not visible
            rasterObj.name = LineValues(0)          'Rename image as the filename for search
            rasterObj.Move point1, point2           'Move image from origin(point1) to photo coordinate (point2)
            rasterObj.Rotate point2, rotationAngle  'Rotate image by bearing around the image coordinate
        Loop
```

```
57      ZoomExtents
58      Beep
59      MsgBox "Images Loaded", vbOKOnly, "Complete"
60      Exit Sub
61
62  ERRORHANDLER:
63      MsgBox Err.Description
64  End Sub
65
66  Sub ReadNames()
67      DefineDirectory
68
69      numImages = 0       'Reset the global variable to 0
70      currentImage = 0    'Reset the global variable to 0
71
72      'Read in the csv
73      Set fso = CreateObject("Scripting.FileSystemObject")
74      Set ts = fso.OpenTextFile(fileDirectory & imageList)
75
76      Do Until ts.AtEndOfStream                   'keep going till no more lines
77          ReadLine = ts.ReadLine                      'read first line
78          LineValues = Split(ReadLine, ",")           'split using commas
79
80              'Append name to end of array
81          ReDim Preserve imageNames(0 To numImages)
82          imageNames(numImages) = LineValues(0)
83          numImages = numImages + 1
84      Loop
85
86      numImages = numImages - 1
87      HideImages  'Set all images to hidden
88      ImageVisable (imageNames(currentImage)) 'Unhide first image
89
90  End Sub
91
92
93  Sub NextImage() 'Move to next image
94          If currentImage = numImages Then
95              currentImage = 0
96          Else
97              currentImage = currentImage + 1
98          End If
99          ImageVisable (imageNames(currentImage))
100         ThisDrawing.Utility.Prompt imageNames(currentImage) & vbCrLf    'Display
            current image name in command line
101 End Sub
102
103 Sub PreviousImage() 'Move to previous image
104         If currentImage > 0 Then
105             currentImage = currentImage - 1
106             Else
107             currentImage = numImages
108             End If
109         ImageVisable (imageNames(currentImage))
110         ThisDrawing.Utility.Prompt imageNames(currentImage) & vbCrLf    'Display
            current image name in camand line
111 End Sub
112
113 Function ImageVisable(name As String)   'Set image with name to visible
114     Dim count As Integer
115     count = ThisDrawing.ModelSpace.count    'Checks how many entities are in the
        drawing
116     Dim newObjs As AcadEntity
117     Dim index As Integer
118     For index = 0 To count - 1  'Runs through entire drawing
119         On Error Resume Next
120         Set newObjs = ThisDrawing.ModelSpace.Item(index)    'Read in entity at index
121         If newObjs.name = name Then                         'If the entity name
            matches required make visible
122             newObjs.ImageVisibility = True
123             newObjs.Visible = True
124             Else
125             If InStr(newObjs.name, "DJI") Then                  ' Hide images with
```

```
            DJI
126             newObjs.ImageVisibility = False
127             newObjs.Visible = False
128             End If
129         End If
130     Next
131 End Function
132
133 Function HideImages()   'Set all images to invisible
134     Dim count As Integer
135     count = ThisDrawing.ModelSpace.count    'Checks how many entities are in the
        drawing
136     Dim newObjs As AcadEntity
137     Dim index As Integer
138     For index = 0 To count - 1  'Runs through entire drawing
139         On Error Resume Next
140         Set newObjs = ThisDrawing.ModelSpace.Item(index)
141         If InStr(newObjs.name, "DJI") Then                  ' Hide images with DJI
142             newObjs.ImageVisibility = False
143             newObjs.Visible = False
144         End If
145     Next
146 End Function
147
148 Function UnHideImages()   'Set all images to visible
149     Dim count As Integer
150     count = ThisDrawing.ModelSpace.count    'Checks how many entities are in the
        drawing
151     Dim newObjs As AcadEntity
152     Dim index As Integer
153     For index = 0 To count - 1  'Runs through entire drawing
154         On Error Resume Next
155         Set newObjs = ThisDrawing.ModelSpace.Item(index)
156         If InStr(newObjs.name, "DJI") Then                      ' Hide images with DJI
157             newObjs.ImageVisibility = False
158             newObjs.Visible = True
159         End If
160     Next
161 End Function
162
163 Function findImage()    'Call a form to select an image from a list of images names
164     Dim ImageName As String
165
166     UserForm1.show
167     ImageName = UserForm1.ListBox1.Value
168
169
170     Dim count As Integer
171     count = ThisDrawing.ModelSpace.count    'Checks how many entities are in the
        drawing
172     Dim newObjs As AcadEntity
173     Dim index As Integer
174     Dim ImageIndex As Integer
175     ImageIndex = 0
176
177     For index = 0 To count - 1  'Runs through entire drawing
178         On Error Resume Next
179         Set newObjs = ThisDrawing.ModelSpace.Item(index)
180
181         If InStr(newObjs.ObjectName, "Image") Then
182             If InStr(newObjs.name, "DJI") Then                  'Hide images with DJI
183                 If StrComp(newObjs.name, ImageName) = 0 Then
184                     newObjs.ImageVisibility = True              'Show selected image
185                     newObjs.Visible = True
186                     currentImage = ImageIndex
187                 Else
188                 newObjs.ImageVisibility = False
189                 newObjs.Visible = False
190                 ImageIndex = ImageIndex + 1
191                 End If
192             End If
193         End If
194     Next
```

```
End Function

Sub exportLines()   'Export a csv of all entities in the drawing
    DefineDirectory

    '*** Define Variables ***
    Dim LnStartPoint As Variant
    Dim LnEndPoint As Variant
    Dim LnLength As Double
    Dim LnHandle As String
    Dim LnColour As String
    Dim PolyPoint As Variant

    Dim index As Integer
    Dim index2 As Integer
    Dim count2 As Integer

    Dim strFullName As String
    strFullName = ThisDrawing.FullName  'Call the name of the drawing
    If strFullName = "" Then    'If the drawing hasnt been saved save the drawing as
    the image list name
        ThisDrawing.SaveAs fileDirectory & Left(imageList, Len(imageList) - 4)
        strFullName = fileDirectory & Left(imageList, Len(imageList) - 4) &
        "ObjectOutput.csv"
        Else
        strFullName = Left(strFullName, Len(strFullName) - 4) & "ObjectOutput.csv"
    End If
    Dim count As Integer
    count = ThisDrawing.ModelSpace.count    'Checks how many entities are in the
    drawing

    '*** Create an out file ***
    Set fs = CreateObject("Scripting.FileSystemObject")
    Set a = fs.CreateTextFile(strFullName, True)
    a.WriteLine ("Handle,Length,StartX,StartY,EndX,EndY,Colour")    'Create first
    line headings

        For index = 0 To count - 1  'Runs through entire drawing
        On Error Resume Next
        Set newObjs = ThisDrawing.ModelSpace.Item(index)

        ' *** Export Lines ***
        If InStr(newObjs.ObjectName, "AcDbLine") Then
            LnHandle = newObjs.Handle
            LnLength = newObjs.Length
            LnStartPoint = newObjs.startPoint
            LnEndPoint = newObjs.endPoint
            LnColour = newObjs.color
            a.WriteLine (LnHandle & "," & newObjs.Length & "," & LnStartPoint(0) &
            "," & LnStartPoint(1) & "," & LnEndPoint(0) & "," & LnEndPoint(1) & ","
            & LnColour)
        End If

        ' *** Export PolyLine ***
        If InStr(newObjs.ObjectName, "AcDbPolyline") Then
            PolyPoint = newObjs.Coordinates
            a.WriteLine (newObjs.Handle & "," & newObjs.Length & ",,,,," & LnColour)
            count2 = UBound(PolyPoint) / 2
            For index2 = 0 To count2
                a.WriteLine (",," & PolyPoint(index2 * 2) & "," & PolyPoint(index2 *
                2 + 1))
            Next
        End If

        ' *** Export Points ***
        If InStr(newObjs.ObjectName, "AcDbPoint") Then
            LnHandle = newObjs.Handle
            LnStartPoint = newObjs.Coordinates
            LnColour = newObjs.color
            a.WriteLine (LnHandle & ",," & LnStartPoint(0) & "," & LnStartPoint(1) &
            ",,," & LnColour)
        End If

```

```
260         Next
261         a.Close ' Close output stream
262
263         Beep
264         MsgBox "Line Coordinates Extracted", vbOKOnly, "Complete"
265     End Sub
266
267     Sub NextPoint() ' Function to move to next image and create a new point
268             If currentImage = numImages Then
269                 currentImage = 0
270             Else
271                 currentImage = currentImage + 1
272             End If
273             ImageVisable (imageNames(currentImage))
274             ThisDrawing.Utility.Prompt imageNames(currentImage) & vbCrLf
275
276             ThisDrawing.SendCommand "_point" & vbCr 'Create a new point
277     End Sub
278
279     Sub NextPaste() ' Function to move to next image and past from "copy" memory
280             If currentImage = numImages Then
281                 currentImage = 0
282             Else
283                 currentImage = currentImage + 1
284             End If
285             ImageVisable (imageNames(currentImage))
286             ThisDrawing.Utility.Prompt imageNames(currentImage) & vbCrLf
287
288             ThisDrawing.SendCommand "_pasteclip" & vbCr 'Paste from memory
289     End Sub
290
291
292
```

Example *2018-05-15_MavicAirTest_CalculationsF4.18+1.6m.csv* input file:

	A	B	C	D	E	F	G
1	DJI_0408.JPG	-28609.5	-3771859	149.2	39.85407	29.8709	
2	DJI_0409.JPG	-28609.3	-3771859	149.2	39.85407	29.8709	
3	DJI_0410.JPG	-28609.3	-3771859	149.2	39.85407	29.8709	
4	DJI_0411.JPG	-28609.3	-3771859	149.2	39.85407	29.8709	
5	DJI_0412.JPG	-28609.3	-3771859	149.2	39.85407	29.8709	
6	DJI_0413.JPG	-28609.2	-3771859	149.2	39.85407	29.8709	
7	DJI_0414.JPG	-28609.1	-3771859	149.2	39.85407	29.8709	
8	DJI_0415.JPG	-28609.1	-3771858	149.2	40.00167	29.98153	
9	DJI_0416.JPG	-28609	-3771858	149.2	39.85407	29.8709	
10	DJI_0417.JPG	-28608.9	-3771858	149.2	39.85407	29.8709	
11	DJI_0418.JPG	-28608.9	-3771858	149.2	39.85407	29.8709	

findImage() UserForm example.

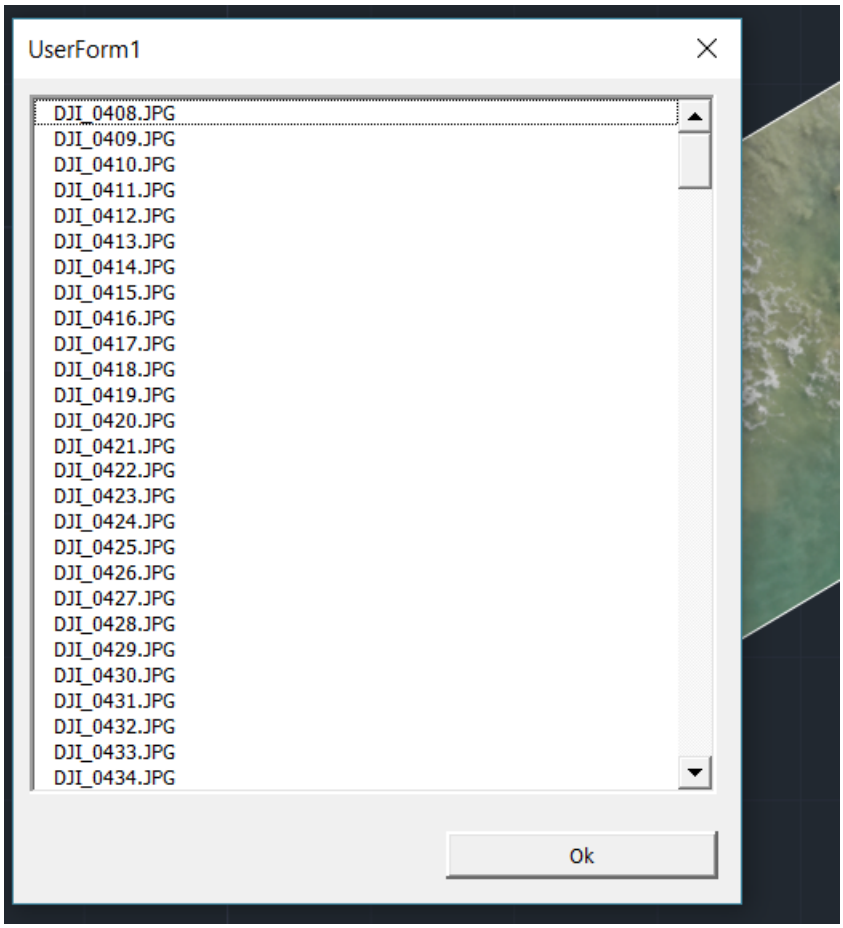

D.2 Matlab figure code

Output Figure Code

```
% Read in all data
close all;clc;clear all;
mxContour = readmatrix('2018-05-15_MavicAirTest_FiguresMatlabUV.xlsm','Sheet','Spatial10sMAtlabData','Range','A1:AP42')
velocity = readtable('2018-05-15_MavicAirTest_FiguresMatlabUV.xlsm', 'Sheet', '10sMatlabVectorData', 'Range', 'F1:I1643')
    %Range set to 5m by 5m bins

% Results Figure with filled contour
figure('Renderer', 'painters', 'Position', [1 1 2900 2200])% [1 1 1450 1100])
hold on
d = imread('C:\Users\Ryan\Documents\Thesis_Working\Mapping\FigureLowTide-Background.jpg');
image(flipud(d), 'XData', [-28750 -28400], 'YData', [-3771950 -3771730]);
[C,h] = contourf(mxContour(1,2:end),mxContour(2:end,1),mxContour(2:end,2:end),[1 5 10 15 20 25 30 35 40 45 50]);
set(h,'LineColor','none')
hcb = colorbar
set(get(hcb,'Title') ,'String','Current Velocity [cm/s]');
quiver(velocity.X,velocity.Y,velocity.Ux,velocity.Uy,'color',[1 0 0],'AutoScaleFactor',1.5);
text(-28483,-3771940,'Arrow Scale: 50 cm/s','HorizontalAlignment','center', 'verticalalignment','bottom', 'FontSize',8)
% Turn off Axes
set(gca, 'XTickLabel', {});
set(gca, 'YTickLabel', {});

saveas(gcf,'2019-01-07_BigWavesResultsFigure.jpg');
hold off
```

UPA30 Figure Code

```
% Read in all data
close all;clc;clear all;
mxContour = readmatrix('2018-05-15_MavicAirTest_FiguresMatlabUV.xlsm','Sheet','Spatial30mVAvg','Range','A1:L10')
velocity = readtable('2018-05-15_MavicAirTest_FiguresMatlabUV.xlsm','Sheet','30mMatlabVectorData', 'Range','A1:D75')
    %Range set to 25m by 25m bins

% Comparison Figure to S Kistners results with contour
figure('Renderer', 'painters', 'Position', [1 1 2400 1700])
hold on
d =imread('C:\Users\Ryan\Documents\Thesis_Working\Mapping\kistner_monwabisi_2016-MB110.jpg');
image(flipud(d), 'XData', [-28776 -28376], 'YData', [-3771990 -3771728]);
[C,h] = contour(mxContour(1,2:end),mxContour(2:end,1),mxContour(2:end,2:end),[1 5 10 15 20 25 30 35 40 45 50]);
colormap(spring)
hcb = colorbar
set(get(hcb,'Title') ,'String','Current Velocity [cm/s]');
quiver(velocity.X,velocity.Y,velocity.Ux,velocity.Uy,'color',[1 0 0],'AutoScaleFactor',1.0);
text(-28540,-3771975,'Arrow Scale: 10cm/s','HorizontalAlignment','center','verticalalignment', 'bottom','FontSize',8)
% Turn off Axes
set(gca, 'XTickLabel', {});
set(gca, 'YTickLabel', {});

saveas(gcf,'2018-05-15_MavicAirTest_MB110Figure.jpg');
hold off
```